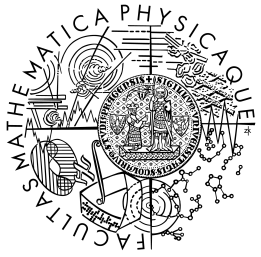

FACULTY
OF MATHEMATICS
AND PHYSICS
Charles University

DOCTORAL THESIS

Lea Chlanová

Structural study of nanocrystalline titanium oxide films and their temperature stability

Department of Condensed Matter Physics

Supervisor of the doctoral thesis:	Prof. RNDr. Radomír Kužel, CSc.
Study programme:	Physics
Study branch:	Physics of Condensed Matter and Materials Research

Prague 2018

I declare that I carried out this doctoral thesis independently, and only with the cited sources, literature and other professional sources.

I understand that my work relates to the rights and obligations under the Act No. 121/2000 Sb., the Copyright Act, as amended, in particular the fact that the Charles University has the right to conclude a license agreement on the use of this work as a school work pursuant to Section 60 subsection 1 of the Copyright Act.

In Prague date ..... signature of the author

Title: Structural study of nanocrystalline titanium oxide films and their temperature stability

Author: Lea Chlanová

Department: Department of Condensed Matter Physics

Supervisor: Prof. RNDr. Radomír Kužel, CSc., Department of Condensed Matter Physics

Abstract:

TiO_2 thin films can exhibit photocatalytic activity and photoinduced superhydrophilicity depending on crystallinity, phase composition and microstructure. These parameters were studied by X-ray diffraction (XRD) and reflectivity (XRR) for magnetron deposited films – nanocrystalline and amorphous, namely their temperature and time evolution. For nanocrystalline films, it was found that higher partial oxygen pressure during the deposition is beneficial. Small anatase crystallites were stable up to about 450 °C. Depth-profiling XRD of some samples revealed that rutile phase was only present close to the substrate. For amorphous films it was found that the crystallization depends strongly on the film thickness and it is slower for very thin films. Evolution of the intensities of anatase diffraction peaks with annealing time could be described by a modified Avrami equation. XRD profile was relatively narrow from the very beginning of crystallization (at about 220 °C), which indicated relatively larger crystallites (> 100 nm), and hence, nanocrystalline films cannot be obtained simply by annealing of amorphous ones. Peak shifts with annealing time indicated generation of a tensile residual stress. These stresses in crystallized films were studied in detail at room temperature. The strain anisotropy in the films was observed and interpreted. Tensile residual stresses formed during the crystallization process increased rapidly with reducing film thickness and inhibited the further crystallization. Additional benefit of the work was the stimulation of further development of the software for total diffraction pattern, namely by inclusion of the effect of elastic anisotropic strain in the films.

Keywords: titanium dioxide, thin film, X-ray diffraction, reflectivity, texture, residual stress, hydrophilicity

Název: Studium struktury a teplotní stability nanokrystalických tenkých vrstev oxidu titaničitého

Autorka: Lea Chlanová

Katedra: Katedra fyziky kondenzovaných látek

Vedoucí práce: Prof. RNDr. Radomír Kužel, CSc., Katedra fyziky kondenzovaných látek

Abstrakt: Tenké vrstvy TiO_2 mohou vykazovat fotokatalytickou aktivitu a fotoindukovanou superhydrofilicitu (smáčivost) v závislosti na krystalinitě, fázovém složení a mikrostruktuře vrstev. Tyto parametry byly studovány pomocí rtg difrakce a reflektivity pro magnetronově naprášené amorfní a nanokrystalické vrstvy, zejména jejich teplotní i časový vývoj. V případě nanokrystalických vrstev byl ukázán pozitivní vliv vyššího parciálního tlaku kyslíku. Malé krystality anatasu (okolo 10 nm) byly stabilní do teplot minimálně 450 °C. Hloubkové profilování rtg difrakcí ukázalo, že fáze rutilu se vyskytuje vždy jen v blízkosti substrátu. Pro amorfní vrstvy byla nalezena výrazná závislost krystalizace na tloušťce vrstev a byla velmi pomalá pro velmi tenké vrstvy. časový vývoj intenzit difrakčních maxim anatasu mohl být dobře popsán modifikovanou Avramiho rovnicí. Rtg difrakční profily byly relativně úzké od samotného počátku krystalizace při cca 220 °C, což indikuje velikost krystalitů větší než asi 100 nm, a tedy nanokrystalické vrstvy nelze jednoduše připravit vhodným žíháním vrstev amorfních. Posuny difrakčních píků s časem poukazovaly vznik tahových zbytkových napětí. Tato napětí v krystalizovaných vrstvách byla detailně studovaná za pokojové teploty po žíhání. Byla nalezena a interpretována poměrně výrazná elastická anizotropie. Tahová zbytková napětí generovaná během krystalizačního procesu se rychle zvyšují se zmenšující se tloušťkou vrstvy a brání další krystalizaci. V důsledku toho klesá rychlost krystalizace se zmenšující se tloušťkou vrstvy. Za významný výsledek práce lze také považovat stimulování dalšího vývoje softwaru pro aproximaci (fitování) celého difrakčního záznamu najednou a to zejména zahrnutí efektu anizotropní elastické deformace ve vrstvách.

Klíčová slova: oxid titaničitý, tenká vrstva, rentgenová difrakce, reflektivita, textura, zbytkové napětí, hydrofilicita

I wish to express gratitude to Prof. RNDr. Radomír Kužel, CSc.for supervising my doctoral studies and for many valuable advices. I am much obliged to Dr. Zdeněk Matěj for introducing me to his M'Struct software. I value all the people with whom I collaborated during my studies and work on the thesis from Department of Condensed Matter Physics. I also wish to thank to Dr. Šícha who kindly granted his TiO_2 samples. I am indebted to my husband for support during writing of this thesis.

This work was supported by a GAUK grant.

Contents

1 Introduction **1**

2 Titanium dioxide **4**
2.1 Crystal structure 4
2.2 Photoactivity and photocatalysis 8
2.3 Superhydrophilicity 11

3 X-ray methods **13**
3.1 X-ray experiment geometry 13
3.1.1 Bragg-Brentano geometry 14
3.1.2 Parallel beam geometry 15
3.2 Phase analysis 16
3.3 Profile analysis 19
3.3.1 Correction for instrumental broadening 20
3.3.2 Analysis of physical broadening 22
3.4 Texture 26
3.5 Residual stress 28
3.6 X-ray reflectivity 31

4 Whole pattern fitting **34**
4.1 Software description, effects and parameters 35
4.1.1 Peak positions 35
4.1.2 Peak intensities 36
4.1.3 Line profiles 37
4.1.4 Residual stress 39

5 TiO_2 sample preparation **41**

6 Films prepared with different partial oxygen pressure **44**

6.1 X-ray results . . . 45
6.2 Summary . . . 50

7 Films prepared as nanocrystalline **51**
7.1 Line profile analysis and phase analysis . . . 52
7.2 Reflectivity . . . 58
7.3 Residual stress . . . 60
7.4 Texture . . . 62
7.5 Hydrophilicity . . . 62
7.6 Summary . . . 64

8 In situ study of temperature stability **65**
8.1 Amorphous samples . . . 65
8.2 High temperature XRD measurements . . . 66
8.3 Isochronal annealing . . . 67
8.4 Isothermal annealing . . . 69
8.5 Line broadening . . . 73
8.6 X-ray reflectivity . . . 74
8.7 Peak shifts - stress development . . . 77
8.8 Residual stress and elastic anisotropy . . . 78
8.9 Texture . . . 84
8.10 Summary . . . 86

9 Comparison with other TiO_2 films **87**

10 Summary of the thesis **94**

Bibliography **97**

List of Figures **105**

List of Tables **110**

List of Abbreviations **111**

Chapter 1

Introduction

Titanium dioxide exhibits several interesting properties and it is studied intensively. It has, for example, a good chemical stability, mechanical hardness, and high refractive index. TiO_2 thin films are studied mainly because of two remarkable effects: photocatalytic activity and photo-induced superhydrophilicity. The former effect is based on the formation of electron-hole pairs. However, the transport of the charge carriers is negatively influenced by their recombination. Separation of the charge carriers is of the key importance in the TiO_2 photoactivity. It has been shown that there is a strong improvement of the charge separation process by decreasing the particle size to about 10 nm. On the other hand, structural defects can lead to a formation of the energy levels around the mid-gap that act as recombination centers. Structural disorder in amorphous films drastically reduces the phototocatalytic effect.

The latter effect, superhydrophilicity of TiO_2, was discovered at the TOTO Inc. laboratories in Japan in 1995. This can be used, for example, for the anti-fogging applications in a steamed environment. Here, a water contact angle on the titania surface as low as about 5° suppresses formation of many small droplets. The mechanism of the photoactivated superhydrophilicity is proposed on the basis of a reconstruction of surface hydroxyl groups under ultra-violet (UV) irradiation.

The two above processes are essentially different but in many cases take place simultaneously on the same TiO_2 surface. It has been found many times that anatase phase of TiO_2 exhibits more than two times higher photoactivity than the rutile phase. From these findings it follows that the films having these properties the best should probably be nanocrystalline

anatase. The anatase phase in TiO_2 films can be quite well formed when the temperature of substrate during the deposition is higher then about 250 °C.

The work of the thesis was done in collaboration with the Faculty of Applied Sciences, University of West Bohemia [1]. From the technological point of view the main aim was to deposit photoactive titania thin films using a reactive pulsed dual magnetron with high deposition rate on unheated substrates and to find a correlation between deposition parameters and physical and functional properties. Very often the films prepared at lower temperatures are amorphous. Then there is a question, if nanocrystalline films cannot be obtained by a suitable annealing. Finally, also nanocrystalline anatase films were successfully deposited at low temperature of substrates (< 180 °C) in the oxide mode sputtering.

In connection with this, the aim of the presented thesis was to study in detail the structural and microstructural characteristics and the phase composition of the films in dependence on the deposition parameters and also to study the temperature stability of the composition and microstructure of the films. In order to achieve this, we applied the X-ray scattering methods which are invaluable for obtaining many such characteristics – phase composition, lattice parameters, crystallite size, microstrain, residual stress, texture, thickness of the film, its density and surface roughness. It appeared that all of these parameters play some role and also can be well-obtained by the X-ray methods. Since it was found that microstructure and crystallization can depend strongly on the film thickness, large attention was given to this problem including *in situ* studies at higher temperatures.

The thesis is organized as follows. At the beginning a brief introduction on titanium dioxide, its polymorphs and basic properties is presented. Additionally, properties of the studied thin films are described, that are important for application, i.e., photoactivity, photocatalysis, and superhydrophilicity. Details of preparation by magnetron sputtering are given in Chapter 5.

The applied X-ray diffraction and reflectivity methods are described and discussed in Chapter 3 and 4, namely used geometries, and various structural properties that can be determined by X-ray methods, as well as our approach to the analysis of the results.

The results of measurements and analyzes are summarized in the remaining chapters. TiO_2 films with equal thickness but prepared under different partial oxygen pressure were measured and analyzed, and the

results are presented in Chapter 6. This is followed by Chapter 7 where samples prepared already as nanocrystalline were studied in dependence on thickness, substrate and annealing.

In order to better understand the crystallization processes and size of the crystallites with annealing, *in situ* high temperature XRD measurements were performed, and are described in Chapter 8. The time evolutions were described by the Avrami theory and structural properties of the films were studied in detail. In the last Chapter 9, some findings of the temperature and time dependences are briefly compared with those obtained for the films prepared by different methods.

Chapter 2

Titanium dioxide

Since the beginning of the 20th century titanium dioxide TiO_2 has found its use in colouring paper, varnishes, plastics but also food products, medicaments, and toothpaste or due to its high refractive index even as a sunscreen. Its main application as an outstanding white pigment somehow overshadows many other interesting properties, such as that titanium dioxide thin film is a photocatalyst under UV light with a great potential for hydrolysis, or recently discovered superhydrophilic properties [2].

This chapter summarizes basic facts about various forms of TiO_2 crystal structure. It further briefly describes properties of the studied thin films that are important for application, i.e., photoactivity, photocatalysis, and superhydrophilicity.

2.1 Crystal structure

The knowledge of crystal structure plays an important role in understanding of chemical and physical properties of TiO_2. The unique properties of titanium dioxide are bound with crystal structure and from recent experiments it seems that nanocrystalline films have even better properties [3].

Titanium dioxide can form a number of polymorphs, of which anatase, rutile and brookite are the three naturally occurring and most important crystal structures. The diffraction patterns of the phases (Fig. 2.1) are very well distinguishable, and so x-ray diffraction is a suitable method for their study.

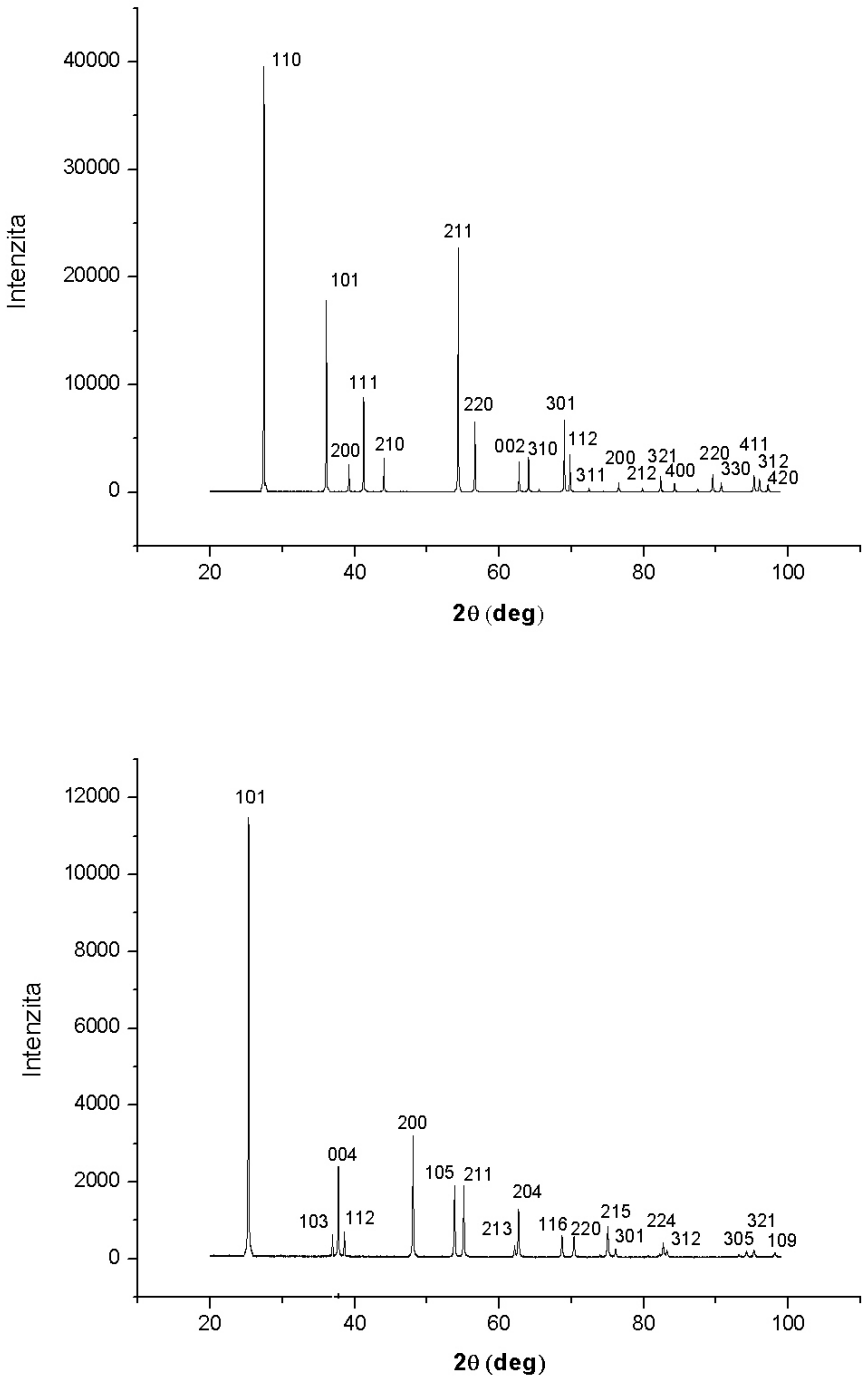

Figure 2.1: Rutile (top) and anatase (bottom) diffraction patterns.

structure	crystal class	space group	lattice constants
anatase	tetragonal	$I4_1/amd$	a = 3.7842 Å, c = 9.5146 Å
rutile	tetragonal	$I4_2/mnm$	a = 4.5937 Å, 2.9581 Å
brookite	orthorombic	$Pbca$	a = 9.182 Å, b = 5.456 Å, c = 5.143 Å

Table 2.1: Spacegroups and lattice parameters of anatase, rutile and brookite. Data taken from Ref. [4, 5, 6].

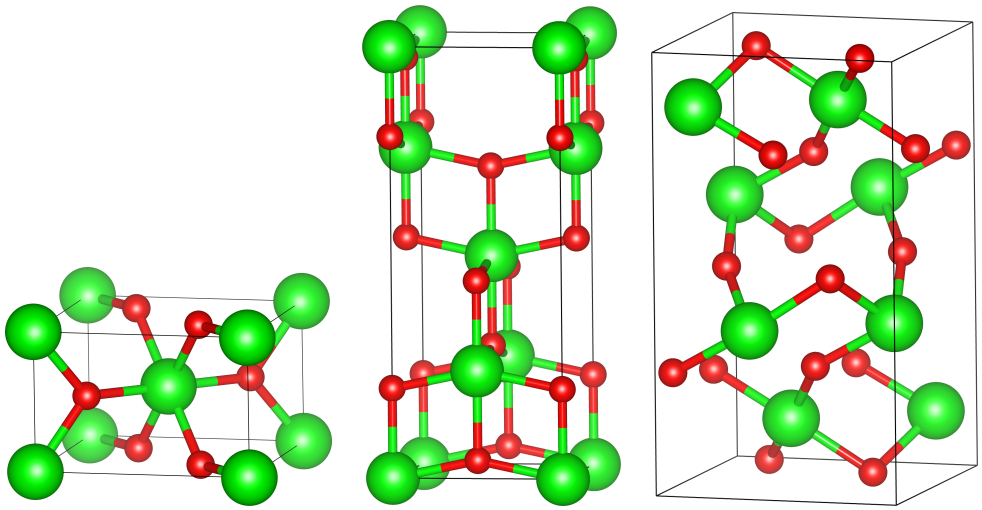

Figure 2.2: Rutile, anatase and brookite crystal structures, the red dots represent oxygen atoms and the green ones represent titanium atoms

Rutile unit cell contains two TiO_2 formulas with titanium atoms surrounded by oxygen octahedrons, where two bonds between the titanium and oxygen atoms at aspices of the octahedron are slightly elongated, and each oxygen atom is bonded to three titanium atoms. The neighbouring octahedra share one corner along the ⟨110⟩-type directions, and are stacked with their longer axis alternating by 90° (Fig. 2.2 left).

The anatase structure (Fig. 2.2 middle) is similar but slightly more distorted than rutile, with deviation from 90° bond angle. The corner-sharing octahedra form (001) planes and are connected by their edges with the plane of octahedra below. The octahedra visualization of anatase and rutile structures are shown in Fig. 2.3.

In brookite structure the oxygen octahedra are irregular, with the interatomic distances ranging from 1.87 to 2.04 Å and different O–Ti–O bond angles ranging from 77 to 105 degrees. The octahedron stacking is similar to rutile since straight polyhedron chains are linked through three different corners of the unit cell, but the linking of polyhedron chains occurs

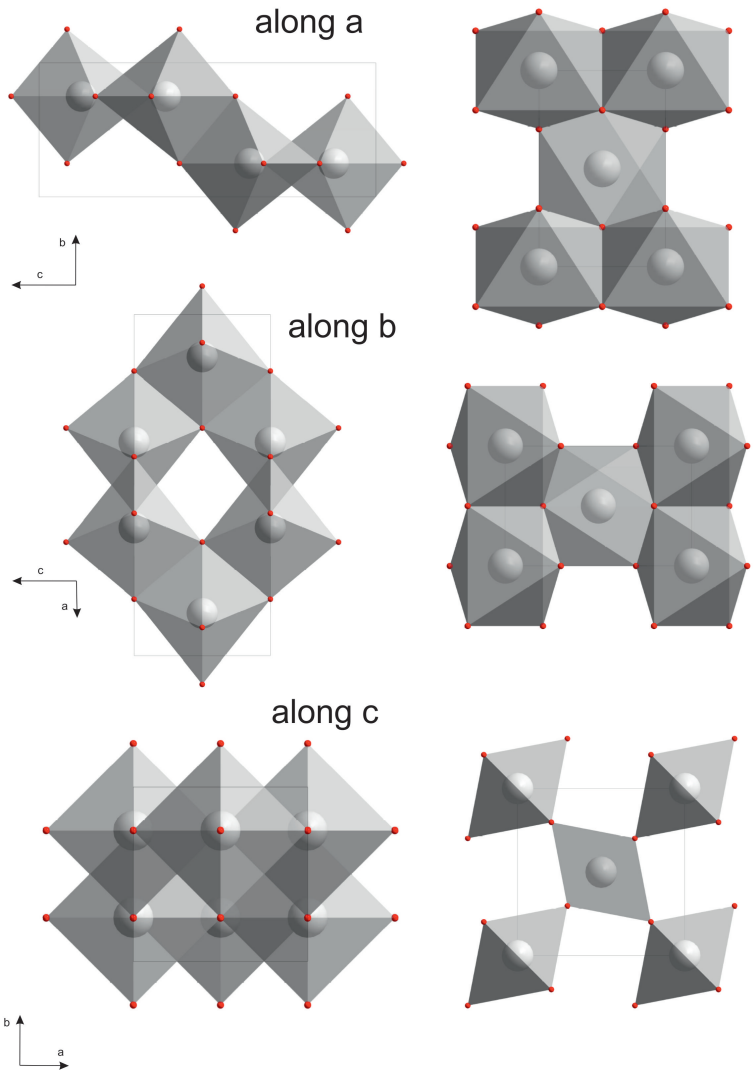

Figure 2.3: Views on anatase (left) and rutile (right) structures along *a*, *b* and *c* axis as obtained by the program Diamond (Crystal Impact software).

through cis bridges in brookite. (Fig. 2.2 right, Fig. 2.3). More details on structures of rutile, anatase and brookite can be found in [7, 8, 9, 10].

From these three phases the rutile is the most common and stable one (brookite is the rarest), both anatase and brookite transform to rutile approximately at 800 $°C$. Rutile then melts between 1830 $°C$ and 1850 $°C$. However, only rutile and anatase play any significant role in the applications of TiO_2 [11].

Beside these three modifications titanium dioxide has also five high pressure phases (e.g., α-PbO_2-like, baddeleyite-like and cotunnite-like) and three metastable forms produced synthetically (monoclinic, tetragonal and orthorhombic), see the phase diagram of a Ti-O system in Fig. 2.4 taken from Samsonov [12]. A high-pressure phase of TiO_2, which has the cotunnite structure, is one of the hardest known oxides. A sample prepared at high temperature and pressure and quenched in liquid nitrogen had a hardness of 38 GPa [13] making it harder than cubic boron nitride for example. However, cotunnite type TiO_2 is not stable at room temperature. Titanium dioxide also occurs as a constituent in ilmenite ($FeTiO_3$) from which it is industrially produced, perovskite ($CaTiO_3$) and titanite ($CaTiSiO_5$). It can be also mined in one of the purest forms as a rutile beach sand [14, 15].

2.2 Photoactivity and photocatalysis

The properties that allow titanium dioxide to be widely used colour agent, e.g., good chemical stability, nontoxicity, high refractive index, and mechanical hardness, are also important for application of TiO_2 as a photoactive material in technology [16, 17, 18, 19, 20, 21]. The photocurrent response of TiO_2 rutile single crystal was observed by Fujishima and Honda at the end of 1960s [22]. They connected a complete electrochemical circuit, with titanium dioxide and platinum back as the two electrodes (Fig. 2.5). After irradiation of the surface of the electrode with light ($\lambda < 415$ nm), the photocurrent flowed from platinum counter electrode to the TiO_2 electrode through the external circuit. On TiO_2 electrode the oxidation reaction (oxygen revolution) occurred while on the Pt electrode the reduction reaction (hydrogen evolution) took place. Their work demonstrated the possibility of using titanium dioxide for generating hydrogen from water and solar (UV) radiation, without application of external voltage. Among the three common crystalline phases, anatase

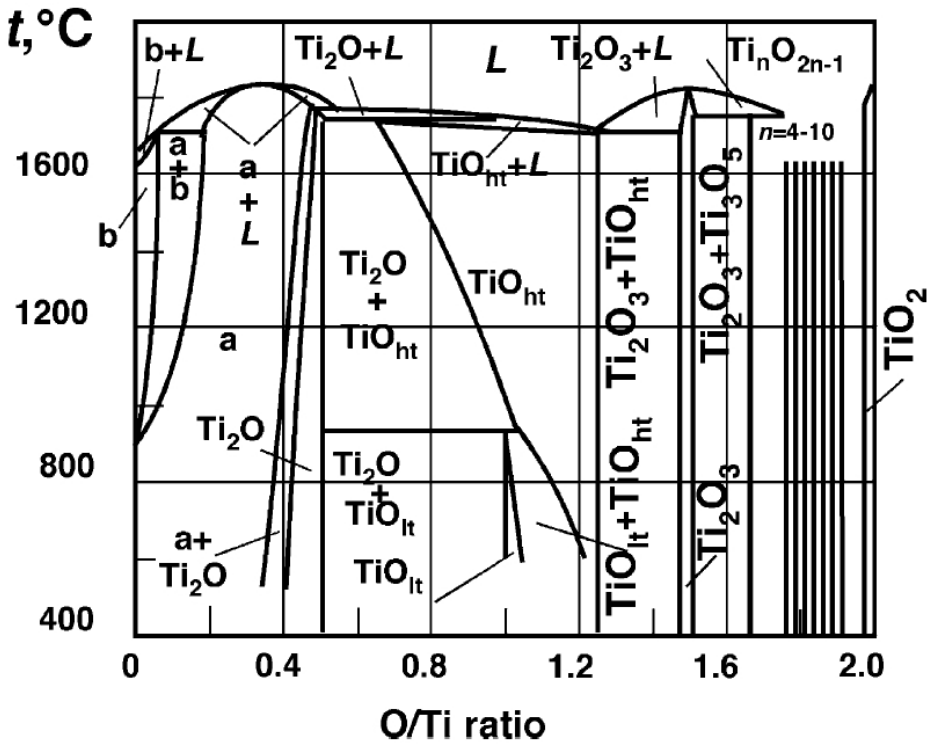

Figure 2.4: Phase diagram of Ti-O system taken from Samsonov [12]. The region Ti_2O_3-TiO_2 contains Ti_2O_3, Ti_3O_5, seven discrete phases of the homologous series Ti_nO_{2n-1} (Magneli phases) and TiO_2.

seems to be the most photoactive one [11, 23].

Until now the use of TiO_2 for hydrogen production has not reached commercial use [24], however, many other very useful reactions can be induced over irradiated surface of TiO_2. It can be used for photocatalytic decomposition of the inorganic and organic compounds into environmentally friendly compounds or the photocatalytic reaction can be used for keeping the surfaces clean and sterile.

After irradiating ($h\nu > E_{BG}$) the semiconductor photocatalyst, an electron-hole pair is created. In case of anatase the band gap energy E_{BG} is 3.2 eV, for rutile it is 3.0 eV. Some of these electron-hole pairs can diffuse to the surface of the photocatalyst (TiO_2) where they participate in reactions with available surface species. The electrons and holes at the surface can either react directly with target compounds or indirectly by creating hydroxyl radicals (•OH), hydrogen peroxide (H_2O_2), superoxide (O_2^-) and singlet oxygen (•O_2). (•OH), hydrogen peroxide (H_2O_2), superoxide (O_2^-) and singlet oxygen (•O_2) are created from OH groups, H_2O and (O_2^-),

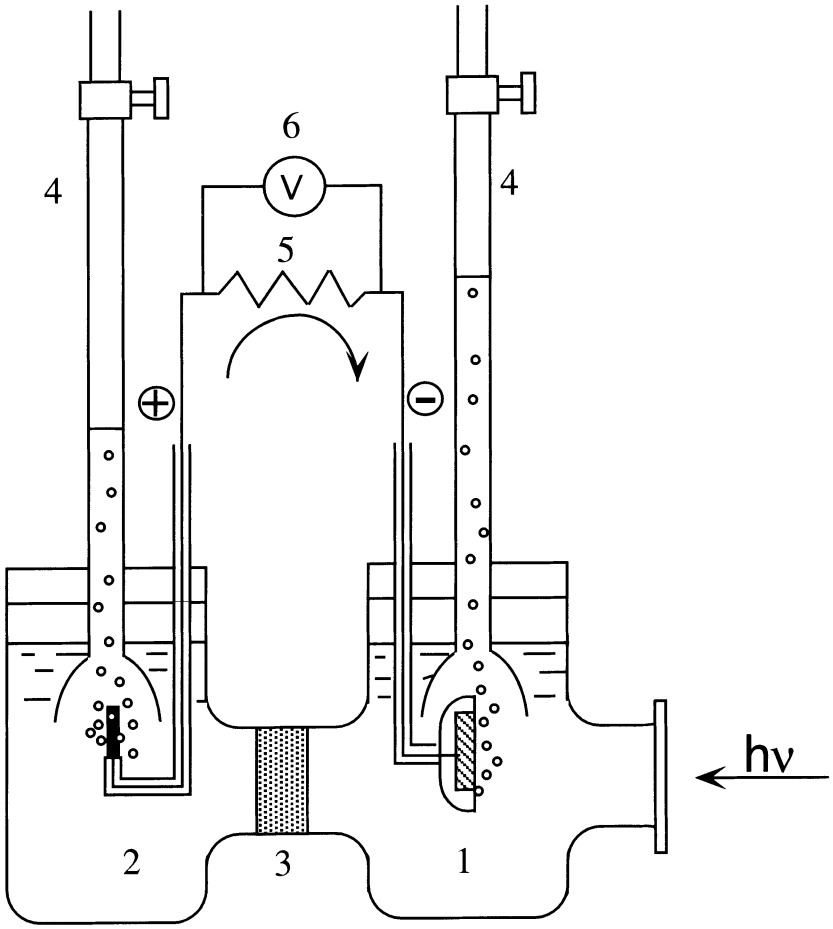

Figure 2.5: Schematic diagram of an electrochemical photocell [18]. (1) n-type TiO_2 electrode; (2) platinum back counter electrode; (3) ionically conducting separator; (4) gas buret; (5) load resistance and (6) voltmeter

all of them play an important role in the decomposition of the organic and inorganic compounds. In principle it is possible to decompose any organic compound to CO_2, H_2O and mineral acids using these active oxygen species. The only condition is the presence of the light with suitable wavelength. Further details about photocatalytic reactions assisted by the photoactivated TiO_2 particles can be found in [25, 21].

TiO_2 seems to be an ideal photocatalyst since it is relatively cheap, chemically highly stable, and photogenerated holes are highly oxidizing. Mainly rutile and anatase are suitable for photocatalysis and have been under intense study recently [23].

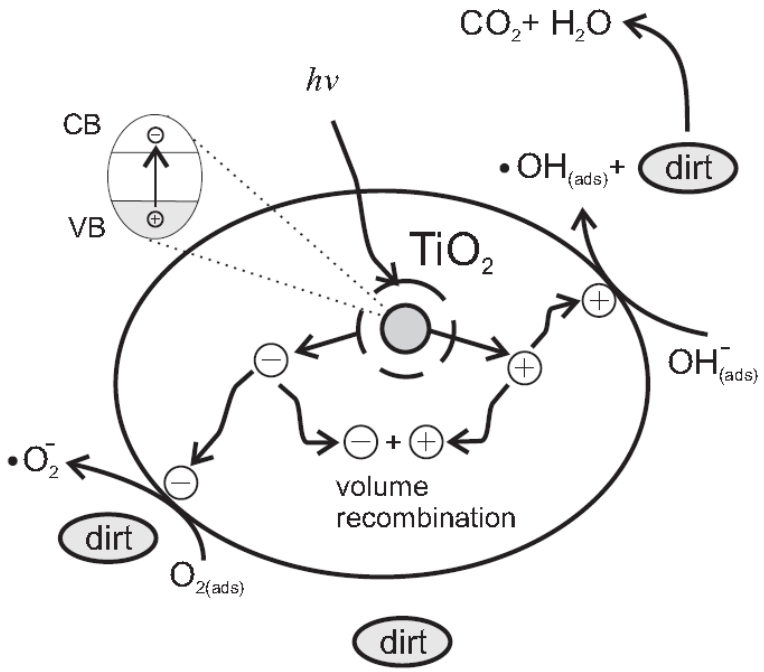

Figure 2.6: The principle of the photocatalytic processes and the formation of the highly reactive radicals on the surface of the TiO_2 particle [18]

2.3 Superhydrophilicity

Another important property of TiO_2, related again to photoactivity, is its superhydrophylic behaviour. The photo induced superhydrophilic behaviour of TiO_2 was for the first time observed by [2] who found that the surface of TiO_2 becomes highly hydrophilic after UV irradiation as the contact angle between a water droplet and the surface approaches zero. Therefore, the water on the surface does not form droplets, but it forms thin, clear and transparent film. After irradiation, the photoactive TiO_2 creates electron-hole pair which can either recombine or react with surface species - in case of titanium dioxide the surface species available for the reaction are Ti^{4+} and bridging O^{2-} groups. As a result, the hydrophilic surface Ti^{3+} species are generated via the reduction of the Ti^{4+} surface species by photogenerated electrons, and oxygen vacancies are generated via the oxidation of the bridging O^{2-} species to oxygen by photogenerated holes. Hydroxyl ions subsequently absorb and fill the oxygen vacancies with the result that the hydrophilic nature of the surface is enhanced [26]. When the UV source is removed the process is reversed as the Ti^{3+} sites

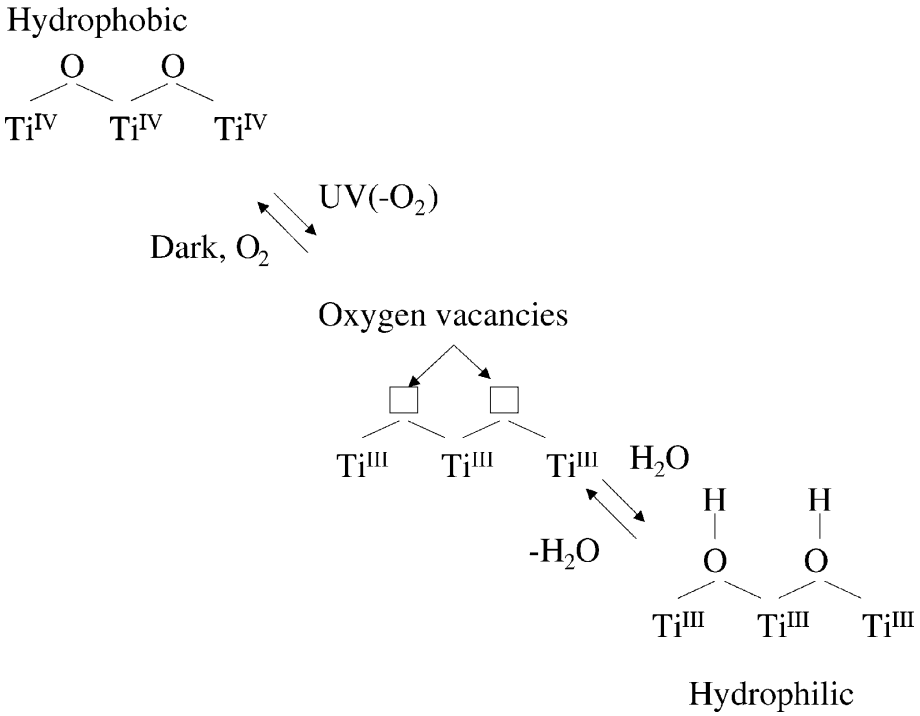

Figure 2.7: Schematic illustration of the major processes associated with the photoinduced superhydrophilic property of titania. UV excitation of the semiconductor creates electron-hole pairs. The holes can oxidixe bridging O^{2-} species on the surface into oxygen, thereby creating vacancies. The photogenerated electrons can reduce the Ti^{4+} atoms to Ti^{3+}. Dissociative adsorption of water onto the irradiated surface hydroxylates it and renders it considerably more hydrophilic. The process is reversed in the dark as the oxygen oxidizes the Ti^{3+} species present and the reduced oxygen fills the bridging oxygen vacancies [27].

are slowly oxidized back to Ti^{4+} by ambient oxygen, and the vacancies are filled by the O^{2-} ions as a consequence of the oxidation. Further details on the photoinduced superhydrophilicity can be found in [27].

The combination of photocatalytic and superhydrophilic properties enables to create so called self-cleaning surfaces. One of the applications of the superhydrophilic behaviour of the TiO_2 thus are, for example, the anti-fogging applications in a steamed environment [28].

Chapter 3

X-ray methods

X-ray diffraction (XRD) is one of the most suited and versatile methods for study of crystalline materials. It is non-destructive and capable of resolving not only the basic crystallographic structure but also different microstructural features. It appeared that it is in particular useful for titanium dioxide thin films since different features and parameters that can be determined by XRD play important role there and are well measurable.

In general, the method allows qualitative and quantitative phase analysis, determination of crystallite size and microstrain. It is also well suited for evaluation of residual stress or preferred orientation (texture). X-ray reflectivity can be used for determination of the film thickness and surface roughness.

Several of these X-ray diffraction methods were employed in this work. A brief description of these applied methods, geometries, and our approach to analysis of the results is given in the following text.

3.1 X-ray experiment geometry

The geometrical arrangement of the X-ray diffraction experiment is defining aspect to what quantities can be obtained and how precisely. There are two main geometries, conventional Bragg-Brentano geometry, which provides higher intensities at lower resolution, and parallel beam geometry with lower intensity but lower sensitivity to sample adjustment and more possibilities due to geometric flexibility.

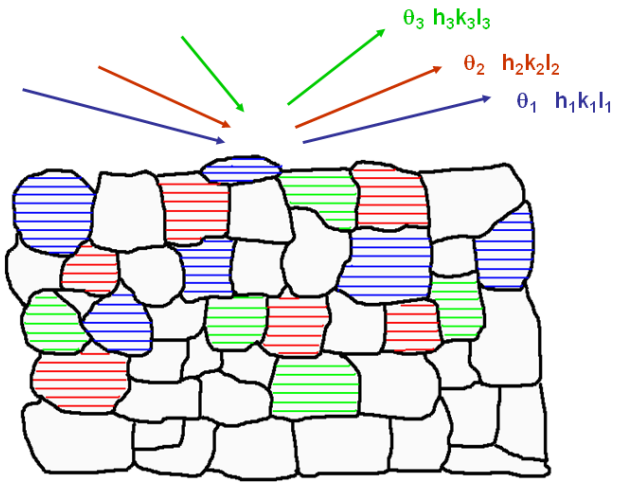

Figure 3.1: Bragg-Brentano conventional powder diffraction geometry - information from the grains oriented with the corresponding planes parallel to the surface

3.1.1 Bragg-Brentano geometry

Basic measurements of standard powder diffraction are performed in the so-called Bragg-Brentano geometry when the signal for all individual diffraction peaks comes from the crystallites oriented with the respective lattice planes parallel to the surface.

The main characteristic of this geometry is that the incidence beam and the diffracted beam are symmetric with respect to the sample surface normal. This can be achieved in two ways during the measurement:

1. by scanning the θ_1 and θ_2 in the same speed in the $\theta - \theta$ configuration,

2. by scanning 2θ at twice the speed of ω in the $\theta - 2\theta$ configuration.

A divergence beam from the source (X-ray tube), after passing the Soller slits 1 and the divergence slit, hits the sample surface with an incidence angle θ. The incident X-rays spread on the sample surface with incidence angles slightly varying from θ. The irradiated area then depends on the incidence angle and beam divergence. The diffracted

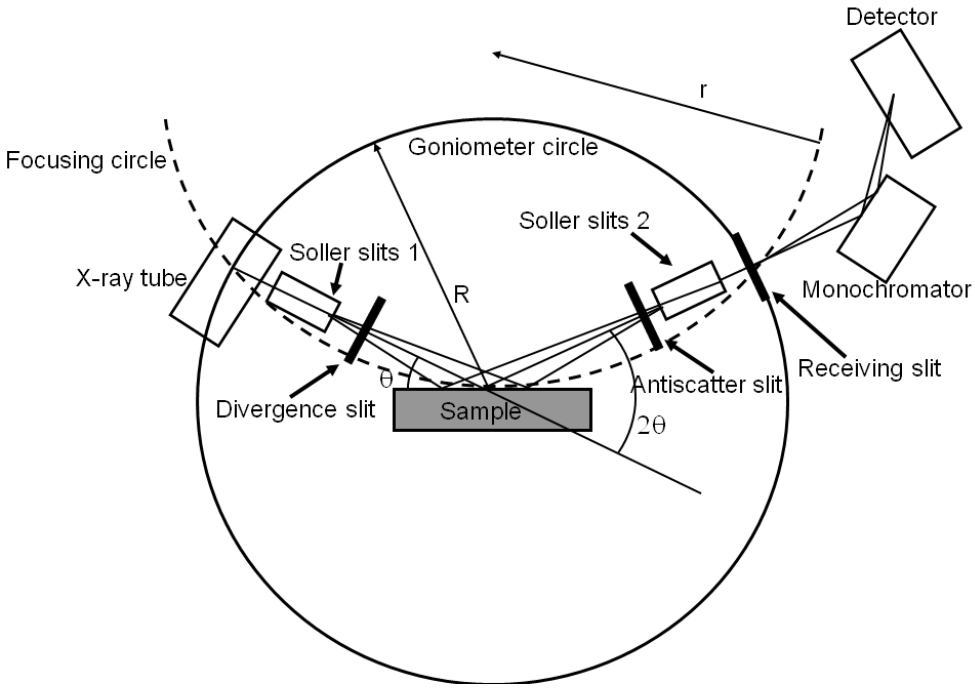

Figure 3.2: Bragg-Brentano conventional powder diffraction geometry.

X-rays leave the sample under the angle 2θ, pass through the antiscatter slit and Soller slits 2 and focus at the receiving slit. The point detector can be placed right after the receiving slit or after a crystal monochromator.

The main advantage of this method is relatively high resolution but on the other hand the drawback of this method is high sensitivity to, in particular, specimen displacement from the goniometer axis. The penetration depth in this method is quite high and depends on the incidence angle θ, and therefore, this technique is not very suitable for measurements of very thin films.

3.1.2 Parallel beam geometry

To study thin films symmetric Bragg-Brentano geometry is insufficient and one has to employ asymmetric geometry (see scheme in Fig. 3.3) which allows to reduce the penetration depth of the beam by using small incidence angles (typically $0.3° - 3°$). Therefore, one can obtain the information from surface of the sample or from a very small depth. Furthermore, this approach enables to control the scanning depth by changing

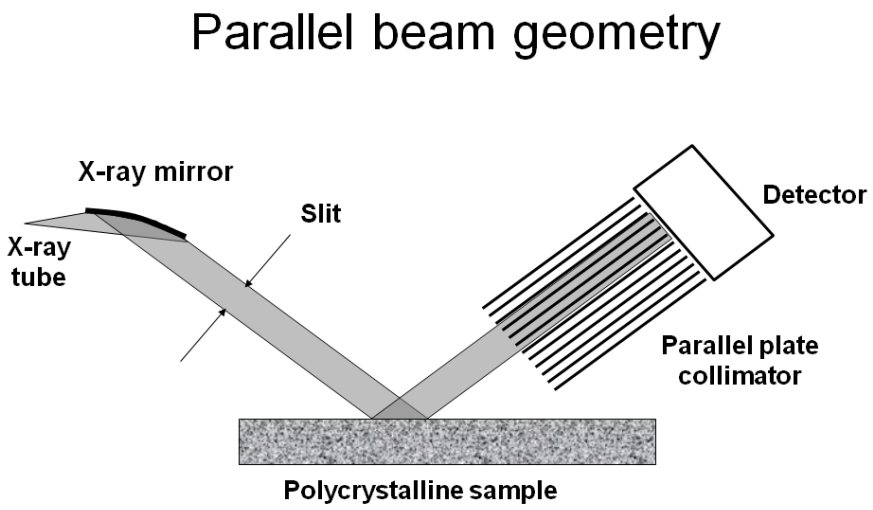

Figure 3.3: Scheme of the parallel beam geometry.

the angle of incidence of the X-ray beam.

Another great advantage of parallel beam is its insensitivity to errors associated with sample displacement, which enables the possibility of using a small incidence angle. Also, samples with a curved surface can be used. On the other hand, parallel beam geometry has about three times lower resolution than the Bragg-Brentano geometry.

3.2 Phase analysis

By the means of X-ray diffraction one can solve a very common problem in material research: the phase composition of an unknown material. By using diffraction methods (X-ray, electron and neutron diffraction) it is possible to obtain the information about crystal structure, and therefore, to distinguish the different phases of the same material. This is the main difference between diffraction methods and chemical analysis (such as fluorescence and spectroscopic methods), which yield only chemical (elemental) composition of the studied material.

The main complications for material identifications are caused by the real structure (texture, structure defects, macroscopic stress). Because of

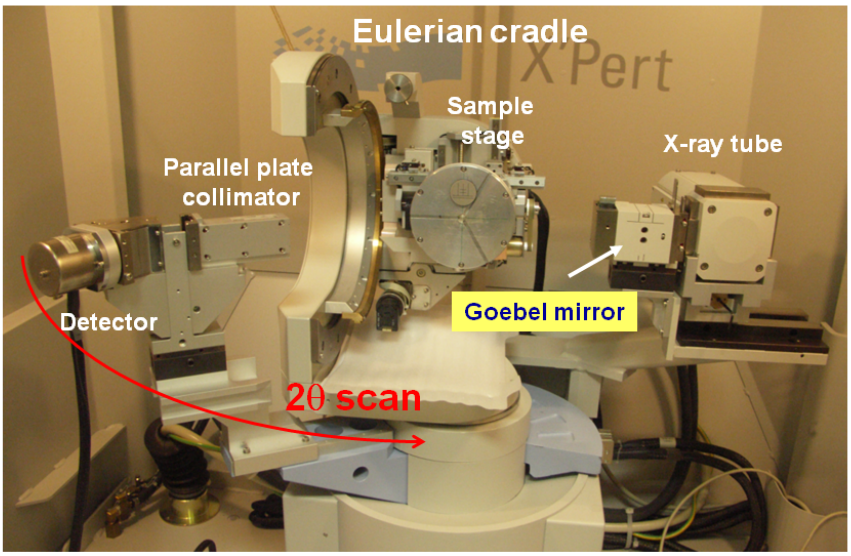

Figure 3.4: Panalytical X'Pert MRD diffractometer in parallel beam geometry.

the fact that some materials with different elemental composition can have very similar, hard to distinguish diffraction patterns, it is very suitable to combine the diffraction phase analysis with the methods of chemical analysis.

From diffraction point of view the phase analysis can be divided into qualitative and quantitative phase analysis. The main task of qualitative phase analysis is the identification of phase or phases in a specimen and estimation of phases in polycrystalline material. Quantitative analysis of diffraction data deals with the determination of amounts of different phases in mixed samples.

Quantitative phase analysis

The volume of the analyzed phase in the sample is directly proportional to the intensity of diffraction lines. For the integrated line intensity of the

powder sample the following formula can be found in the literature [29].

$$I_{\mathrm{hkl}} = \left(\frac{I_0 e^4 \lambda^3 d}{32\pi m^2 c^4 r}\right)\left(\frac{p|F_{hkl}|^2}{V_e^2}\right)\left(\frac{1+\cos^2 2\theta}{\sin^2\theta\cos\theta}\right)A(\theta)V_{hkl}, \tag{3.1}$$

where I_0 is the intensity of the incidence radiation, e is the electron charge, m is the electron mass, c is the speed of light, λ is the wavelength of the used radiation, d is the slit width in front of the detector, r is the goniometer circle radius, p is the multiplicity of the crystallographic planes, F_{hkl} is the structure factor which also includes Debye-Waller factor, V_e is the volume of the elementary unit cell, $A(\theta)$ is the absorption term and V_{hkl} is the diffracting volume.

It is important to emphasize that previously mentioned formula is for the powders, while for the thin films the formula needs some corrections [30]. Additionally, for small incidence angles the Bragg angle shift from reflection is much larger and must be taken into account in determining the lattice spacing. The shift $\Delta 2\theta$ is given by [31]

$$\Delta 2\theta = 2\theta_{obs} - 2\theta_{cal} = \frac{\delta}{\sin(2\theta_{cal})}\left(2 + \frac{\sin(\alpha)}{\sin(2\theta_{cal})} + \frac{\sin(2\theta_{cal})}{\sin(\alpha)}\right). \tag{3.2}$$

It can be shown [30] that formula 3.2 can be (for small α about 0.001 *rad*) rewritten as

$$\Delta 2\theta = \frac{2\delta}{sin(2\theta_{cal})} - \frac{\delta}{\alpha} \tag{3.3}$$

where $\Delta 2\theta$ and α are in radians. The general formula for the diffracted intensity is then [32]

$$I = CL(\theta)P(\theta)A(\alpha,\theta,t)\frac{|F_{hkl}|^2}{V_c^2}Vn_{hkl}T(\alpha,\theta), \tag{3.4}$$

where V is the sample volume, θ is the Bragg angle, α the incidence angle, $L(\theta)$ is the Lorentz term, $P(\theta)$ the polarization term, F_{hkl} the structure factor, V_c the volume of the elementary unit cell and n_{hkl} is the multiplicity of crystallographic planes hkl, C is the multiplicative factor, $A(\alpha,\theta,t)$ is the absorption term and $T(\theta)$ is the texture term. The information about the thickness t is included in the term $A(\alpha,\theta,t)$.

As it is shown in [33, 34], for the absorption factor in the thin film with thickness t it is possible to express the formula as

$$A(\alpha,\theta,t) = \frac{1}{\mu}\frac{\sin\beta}{\sin\alpha+\sin\beta}\exp\left(-\mu t\left(\frac{1}{\sin\alpha}+\frac{1}{\sin\beta}\right)\right), \tag{3.5}$$

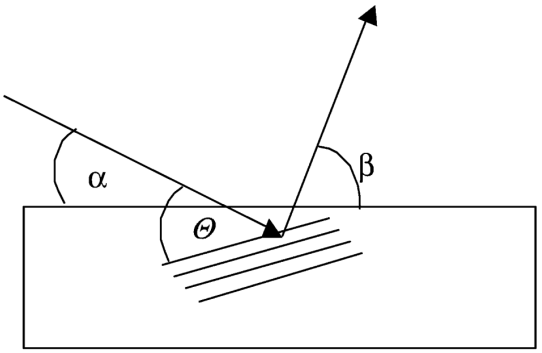

Figure 3.5: Definition of angles α, β and θ, [32].

where μ is the linear absorption coefficient for the thin film. The definition of the angles α, β and θ is shown in Fig. 3.5.

The formula for the intensity of the thin films is, however, valid only for large incidence angles. For small incidence angle one has to take into account refraction and transparency on interface [35]. Colombi et al. [35] evaluated the intensity of a Bragg reflection by integrating the contribution arising from scattering at different depths weighted by the effective scattering volume and the beam intensity below the surface:

$$I(\alpha, 2\theta) \propto \int_0^{\text{Thickness}} |t(n,\alpha)|^2 A(z,\alpha,2\theta) G(\alpha,\Delta V) dz, \tag{3.6}$$

where A is the absorption term due to the geometrical path of a wave scattered at a depth z under the surface. A can be expressed as

$$A(z,\alpha,2\theta) = \exp\left(-\frac{1}{L_{1/e}}\left(\frac{z}{\sin\alpha} + \frac{z}{\sin 2\theta - \alpha}\right)\right), \tag{3.7}$$

where $L_{1/e}$ is the penetration depth (the depth at which the intensity is attenuated by a factor $1/e$). $G(\alpha, \Delta V)$ is a geometrical correction factor which takes into account the effective scattering volume and the beam intensity per unity of surface.

3.3 Profile analysis

The study of structural imperfection (microstructure) by the means of X-ray powder diffraction is known as line profile analysis. Microstructure affects the breadth and shape of a diffraction line profile and may also introduce a displacement from its ideal position [36]. From the change

of peak positions the lattice parameters, lattice geometry and defects, and also the residual stress can be evaluated, and integrated intensities provide information about the atomic structure, texture, and lattice vibrations. The widths and shapes of diffraction peaks allow to evaluate internal strains, coherent domain size, lattice defects, and distribution of lattice defects and domains, respectively. Any of these characteristics can be determined from a single powder diffraction pattern for each phase separately.

When analyzing the line broadening one has to consider also the influence of used instrument – instrumental broadening. There should be an effort to minimize instrumental broadening, i.e., to increase the resolution, which usually comes at the cost of intensity. Conventional parafocusing Bragg-Brentano geometry usually has quite a good resolution, so that the influence of instrumental broadening can be neglected. The problem emerges in the analysis of thin films when the symmetric scan is often inconvenient because of larger penetration depth and for asymmetric scans parallel beam geometry is preferred.

3.3.1 Correction for instrumental broadening

Measured diffraction profile $h(s)$ is a convolution of physical profile $f(s)$ with the function describing the influence of experiment geometry and spectral line broadening $g(s)$

$$h = g * f \; h(s) = \int g(z) f(s - z) dz \tag{3.8}$$

Deconvolution must be performed in order to obtain the profile f. There are several procedures for the deconvolution, e.g., the Stokes method which is based on theorem that the Fourier transform of convolution of a product of two functions is the product of corresponding (in general complex) Fourier coefficients.

Nowadays, there are methods and software for calculation of instrumental function as a convolution of many components such as specimen displacement, absorption, vertical divergence, flat sample, spectral components etc. However, mostly the g-function is determined by measurement of diffraction line profile on a standard – a material with negligible own physical broadening. The best way is to use material with identical composition as the studied sample but this is rarely possible and certified standard can used instead, such as LaB_6 from the NIST (National Institute of Standards).

Unfortunately, the deconvolution in this case is mathematically ill-defined problem (finite range of profile, truncation, noise) and can lead to systematic errors. There are some methods to overcome the problem, e.g., by the so-called regularization.

Simplified approximative procedures may be used for the line broadening. In many cases the Cauchy (C), quadratic Cauchy (C2) or Gauss (G) functions are considered for approximation of the diffraction profile. Probably the best approximation is the Voigt function – the convolution of the Cauchy and Gauss functions.

Then the profile shape can be characterized by the ratio φ of FWHM (full width at half of maximum) and integral breadth β (integrated intensity divided by the peak height) with the limiting values,

$$\varphi = 0.9395 \quad (\text{for } \xi = 0) \text{ a } \varphi = 0.6366 \quad (\text{for } \xi = \infty)$$

De Keijser, Langford, Mittemeijer and Vogels [37] published empirical approximations for precise relations between the ratio φ and width components:

$$\begin{aligned} \beta_c/\beta &= 2.0207 - 0.4803\varphi - 1.7756\varphi^2, \\ \beta_g/\beta &= 0.642 + 1.4187\sqrt{\varphi - 2/\pi)} - 2.2043\varphi + 1.8706\varphi^2. \end{aligned} \tag{3.9}$$

Both components of the total integral breadth β – Cauchy (β_c) and Gauss (β_g) – can then be determined. The total integral breath (or FWHM) can be obtained from these components according to another empirical formula:

$$\begin{aligned} \beta_g/\beta &= -\xi\,\pi/2 + 0.5\sqrt{\pi\xi^2 + 4} - 0.234\,\xi\,\exp(-2.176\xi), \\ \varphi &= \sqrt{(1+\xi^2)/\pi}\,(-\xi\,\sqrt{\pi} + \sqrt{\pi\xi^2 + 4}) - 0.1889\,\exp(-3.5\xi), \end{aligned} \tag{3.10}$$

where $\xi = \frac{\beta_c}{\sqrt{\pi}\beta_g}$.

The correction for instrumental broadening can then be performed easily separately for both components (Gauss and Cauchy), for which the following well-known relations can be used:

$$\beta_{fc} = \beta_{hc} - \beta_{gc} \qquad \beta_{fg}^2 = \beta_{hg}^2 - \beta_{gg}^2. \tag{3.11}$$

C and G components for physical profile then can be synthesized into total corrected integral breadth according to relation (3.10).

In the last years, instead of deconvolution, the convolution of known instrumental profile g with unknown physical profile described by some function with a few parameters is fitted on experimental data for example as follows:

$$I(S_i) = b(S_i) + \sum_j \sum_k f_j(S_i - x_k) g_j(x_k) \Delta x, \tag{3.12}$$

where Δx is a step of measurements, b is the background value and j corresponds to individual reflections. This approach was also used in the M'Struct software for total powder pattern fitting, which was employed in this work (see Chapter 4).

3.3.2 Analysis of physical broadening

Analysis of physical profile can be performed either in the direct space by means of Fourier coefficients or in the reciprocal space directly from the measured profiles. The first way is more clear and easier with respect to the physical interpretation of microstructural parameters, the latter one is easier from the point of view of experiment, evaluation and lower sensitivity to experimental errors. There are basically two models of microstructure description – phenomenological and microscopic based on considerations of distributions of different lattice defects, namely dislocations. In our case, we preferred the first model since dislocation are not the only reasons for strain broadening in the studied films.

In the phenomenological model, it is assumed that the crystal consists of mosaic blocks (crystallites – coherently diffracting domains) that can be misoriented so that the diffracted waves are incoherent. At the same time there are inhomogeneous distortions of crystal structure that cause shifts of lattice cells (microstrain).

Now, the reciprocal space approximative methods are briefly described.

Crystallite size broadening

Relation between the integral breadth and the crystallite size in the measured direction is given by the well-known Scherrer equation

$$\beta_D = 1 \,/\, D \tag{3.13}$$

where D is the so-called apparent crystallite size perpendicular to the measured lattice planes (hkl), i.e., in the direction of the diffraction vector

(in the reciprocal space units - $1/d$). This crystallite size is the volume average

$$D = \frac{1}{V} \int \int \int T \mathrm{d}x \mathrm{d}y \mathrm{d}z, \tag{3.14}$$

where V is the crystallite volume, T its thickness in a point (x, y, z) in the direction of the diffraction vector and the integration is performed over the whole volume of the crystallite. *True* crystallite size p is then defined as the third root of the volume and it is related to the apparent size as

$$p = K_\beta \, D, \tag{3.15}$$

where K_β is the Scherrer constant dependent on the crystallite shape. Scherrer constants (~ 1) were published for different crystallite shapes (spheres, cubes, parallelepipeds, tetrahedrons, cylinders etc, e.g., [38] or [39]. For spheres $K_\beta = 1.0747$ for all reflections. It should be noted that the method can be used for determination of the crystallite size in the range from a few nanometers up to about 300 nm by the conventional laboratory powder diffractometry.

Microstrain

Relation between the integral breadth and microstrain $e = \Delta d/d$ is given as follows

$$\beta_s = \frac{4e}{\lambda} \sin\theta, \tag{3.16}$$

that is well-defined only for the Gaussian distribution of the microstrain. However, it is formally used also in other cases. The quantity e can be related directly to crystal defects or to the so-called 2nd kind stresses. Correct interpretation of this type of XRD line broadening is not always easy, however, it can be useful for comparison of samples or for study of thermal evolution of microstructure.

Size-strain separation

Methods for separation of size and strain effects are, in principle, based on different behaviour of both effects in the reciprocal space. While the size broadening is independent of the diffraction vector magnitude, the strain broadening is directly proportional to it. Total integral breadth is given by

$$\beta = \frac{\beta_D \beta_s}{\int I^D I^s dS}, \tag{3.17}$$

where S is a variable (1/d), D contribution from the size effect and s contribution of microstrain. For derivation of analytical expression and calculation of the integral, different approximations for both components must be used. Realistic and often used functions are the Gauss (G), Cauchy (C) and quadratic Cauchy (C2).

Below a few cases are shown; for symbols C, C2, G, the first one is always that related to the size effect. The simplest combinations are (see also the section on instrumental broadening) C-C and G-G. Then

$$\text{C-C}: \ \beta = \beta_D + \beta_s \qquad \text{G-G}: \beta^2 = \beta_D^2 + \beta_s^2. \tag{3.18}$$

Empirically, the Cauchy function for crystallite size and G or C2 for microstrain are considered. Then the following relations are used

$$\text{C-C2}: \ \beta = \frac{\beta_D + 2\beta s}{\beta_D + 4\beta_s} \qquad \text{C-G}: \beta = \frac{\beta_s \ \mathrm{erf}\left[-\frac{1}{\pi}(\frac{\beta_D}{\beta_s})^2\right]}{1 - 2\ \mathrm{erf}\left[\frac{\sqrt{2}}{\pi}\frac{\beta_D}{\beta_s}\right]}. \tag{3.19}$$

Often, the well-known Williamson-Hall plot, i.e., dependence of integral breadth β on $\sin\theta$ is used that corresponds to not very realistic combination C-C, is used. Usual relation can be modified as follows

$$\beta_{hkl}^{\kappa} = \frac{\mathcal{K}}{D_{hkl}} + \mathcal{L}(4e_{hkl}\sin\theta\ /\lambda\ )^q \tag{3.20}$$

in order to suppress the errors made by the considered C-C assumption.

Constants κ, $\mathcal{K}$, $\mathcal{L}$, and q depend on the considered approximation. Some more realistic combinations are shown in Table 3.3.2. In practice, some mean values between the cases $\beta_D << \beta_s$ and $\beta_D >> \beta_s$ must be used.

For the combination C-G (actually the Voigt function) often the parabolic approximation is used

$$\frac{\beta_D}{\beta} = 1 - \frac{\pi}{2}\frac{\beta_s}{\beta}. \tag{3.21}$$

Both D and e can be dependent on the crystallographic direction, and consequently, the integral breadth would be also hkl dependent. Therefore, the dependence (3.20) should be used for more orders of the reflection (e.g., 111, 222, 333) rather than for different directions.

In the literature the simplified application of the Voigt function method (see section on instrumental broadening) can be used. If we assume that the Gaussian component is related only to the microstrain while the Cauchy component only to the small crystallite size, then both parameters D and e can be determined from each single reflection

$$D = 1/\beta_c \qquad \mathrm{e} = \lambda\beta_g\ /\ 4\sin\theta. \tag{3.22}$$

Table 3.1: Constants in the modified Williamson-Hall plot.

	condition	$\mathcal{K}$	$\mathcal{L}$	q
C2	$\beta_s \gg \beta_D$	0.75	1	1
	$\beta_s \ll \beta_D$	1	2D	2
G	$\beta_s < \beta_D$	$2/\pi$	1	1
	$\beta_s \ll \beta_D$	1	D/2	2

In case we don't want to be restricted by such assumptions, it is possible for the calculated Cauchy and Gauss components β_c a β_g of the physical profile to apply relations (3.9) and calculate components $\beta_{Gd}, \beta_{Gs}, \beta_{Cd}$, and β_{Cs}. These can be synthesized with the aid of (3.10) and both quantities D and e determined. In this work we did not apply the first approach which is oversimplified nor the second one which gave rather noisy values of widths.

Fourier analysis of diffraction profiles

Fourier analysis known as Warren-Averbach ([40] or [38]) analysis provides an approach that is less burdened with approximations compared to the previous method. The diffraction profile can be expressed as the Fourier series

$$I(2\theta) = K \sum_{-\infty}^{\infty} A_n \cos 2\pi n h_3 + B_n \sin 2\pi n h_3, \tag{3.23}$$

where $h_3 = 2d_0 \sin\theta/\lambda$ (d_0 corresponds to the interplanar spacing of the first order of the measured reflection and the Fourier coefficients A_n can be expressed as a product of the size A_n^D and strain A_n^s coefficients.

Size coefficients are given by relations

$$A_n^D = N_n / N_3, \tag{3.24}$$

$$A_n^D = \frac{1}{N_3} \sum_{i=n}^{\infty} (i-n) p(i), \tag{3.25}$$

where N_n is the total number of pairs of elementary cells separated by n other cells, $p(i)$ is the fraction of columns with the length of i cells, and N_3 is the total number of cells in studied direction according to the original Warren notation. This can be easily generalized to any direction. The first derivation of the coefficients in the origin gives directly the mean value

of N_3, i.e., the crystallite size:

$$\left(\frac{dA_n^D}{dn}\right)_{n=0} = -\frac{1}{n}. \tag{3.26}$$

Strain coefficients are given by the mean value of relative displacements of the cell pairs

$$A_n^s = \langle \cos 2\pi l Z_n \rangle, \tag{3.27}$$

where l is the reflection order and Z_n is the relative displacement of cell pairs separated by n other cells. If the mean value of $\langle Z_n \rangle$ is equal to zero then $B_n = 0$ and profile is symmetric and unshifted. For Gaussian distribution of displacements Z_n we can write $A_n^d = \exp(-2\pi^2 l^2 \langle Z_n^2 \rangle)$, and the size and strain coefficients can be separated according to

$$\ln A_n = \ln A_n^s - 2\pi^2 l^2 \langle Z_n^2 \rangle, \tag{3.28}$$

which is also a good approximation for small n, in general case. In practice, the real distance L is used instead of the number of lattice cells n. Then we can apply the following relation

$$\ln A_L = \ln A_L^s - 2\pi^2 \langle \varepsilon(L)^2 \rangle L^2 / \, d^2, \tag{3.29}$$

where $L = na_3$ (a_3 denotes the lattice parameter in the studied direction) and $\varepsilon = \Delta L / \, L$ is the microstrain.

In conventional analysis, the dependences $\ln A$ vs. $1/d^2$ are plotted for different L. From the slopes we get $\langle \varepsilon_L^2 \rangle$ and from the intercepts values of $\ln A_L^D$. From the slope of A_L^s vs. L plot we determine the mean value of the crystallite size $\langle L \rangle$ in the studied direction $\langle hkl \rangle$ and finally we can plot also the dependence of microstrain $\langle \varepsilon(L)^2 \rangle$.

Described procedure has several drawbacks. It consists of several steps (background separation, doublet separation, Fourier transformation for standard and sample, deconvolution) and experimental errors are emphasized. Nowadays, there is usually a preference to include the above mentioned Fourier coefficients into the function fitted to whole diffraction pattern (see Chapter 4).

3.4 Texture

The distribution of crystallographic orientations of grains in a polycrystalline sample is in general described by texture. A sample with fully

random orientations has no texture, while if the crystallographic orientations have some preferred orientation then the sample has an appropriate texture – depending on the percentage of crystals having the preferred orientation.

When the texture is present, the individual integrated intensities of *hkl* peaks, I_{hkl}, may differ significantly from the theoretical intensities, given primarily by the structure factors, R_{hkl}, and such an effect can usually be described by some model and corrected (e.g., March-Dollase [41, 42]). The preferred orientation can also be characterized by the so-called Harris texture indices T_{hkl} defined as normalized ratios I_{hkl}/R_{hkl}.

It is, however, not always possible to ascribe the observed variations of intensities to the texture, as they may be related to the crystal structure itself or one can simply have a poor grain statistics. In such cases, other than symmetrical scans must be used as the effects are usually weak for powders – but they may be significant for bulk materials and in particular for thin films. In order to completely characterize textures (and also stresses) it is required to incline the measured specimen from symmetrical position. This can be realized in the Eulerian cradle where besides the rotations around the goniometer axis (angle θ) also perpendicular directions (ψ or χ) are possible. Parallel beam optics with polycapillary is usually preferred in order to reduce instrumental aberrations and increase intensity, of course, at the cost of reduced resolution. A brief list of possible asymmetric θ-2θ scan arrangements is as follows:

- Ω-scan, ψ-scan. For a given diffraction peak *hkl* the detector is fixed in Bragg position of measured peak. The scan is then performed by rotation of the specimen about the goniometer axis (or perpendicular axis, respectively) and a shift of the peak maximum from the original position (symmetric Bragg case) indicates inclination of the texture.

- ϕ-scan. The detector is again fixed in the Bragg position of measured diffraction peak and the sample is rotated around the surface normal. It must be done in asymmetric position for the lattice planes inclined to the film surface. Independence of intensity on ϕ indicate axially symmetric texture.

- Pole figure measurement. The detector is fixed in the Bragg position of measured diffraction peak and intensities for different sample

inclinations (ϕ, ψ) are measured and displayed in stereographic projection. This enables a full characterization of texture.

- Orientation distribution function. It is calculated from several pole figures and describes the so-called 3D texture. It is then used as a weight function for calculation of different physical properties of whole polycrystalline material.

3.5 Residual stress

The residual stress is defined as a stress which is present in the sample without any external forces. Three types of residual stress can be distinguished, according to the volume in which the residual stress remains homogeneous:

- type I, **Macro stress - residual stress (σ^{I})** homogeneous within the body of the component over a range much larger than the grain size.
- type II, **Micro stress (σ^{II})** varies on the scale comparable to an individual grain dimensions, homogeneous within a single grain.
- type III, **Micro stress (σ^{III})**, inhomogeneous, exists within a grain as a result of present dislocations or other crystalline defects.

The residual stress is determined by measurement of lattice spacing in dependence on the inclination ψ of the crystal lattice plane with respect to the specimen surface. The geometry is typically similar with that for texture measurements and there are again several different approaches how to measure the dependence:

- 2Ω-scan. With small constant angle of incidence the detector scan gives information related to the lattice plane *hkl* (in particular lattice spacings) – differently inclined with respect to the surface for different *hkl*. Parallel beam geometry is required. Elastic anisotropy of the material may cause scatter of values.
- θ-2θ scan with the ω-goniometer. The specimen is tilted by ψ from the symmetrical Bragg position around the goniometer axis and peak positions for different ψ are measured by a θ-2θ scan. This can be done for several *hkl*, however, for low angle peaks the range of possible angles ψ is geometrically significantly restricted.

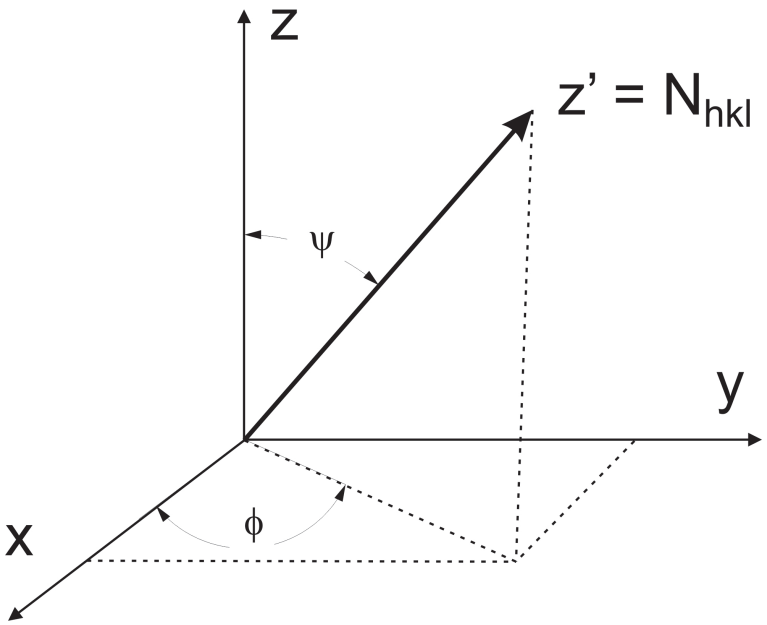

Figure 3.6: Illustration of the coordinate systems associated with the specimen and laboratory.

- θ-2θ scan with the ψ-goniometer. Analogously, the specimen is tilted by ψ in the Eulerian cradle around the axis perpendicular to the goniometer axis and again peak positions for different ψ are measured by a θ-2θ scan, this time with no significant geometrical restrictions for ψ.

The methods for stress evaluation by XRD are described for example in [43] or [44]. For the description of residual stress we use three coordinate systems: $(\vec{x}\vec{y}\vec{z})$ of the specimen, $(\vec{x}'\vec{y}'\vec{z}')$ of the laboratory system, in which the lattice strain is measured along the third axis, and $(\vec{x}_H\vec{y}_H\vec{z}_H)$ as the system of the principle axis of deformation (see Fig. 3.6). If the ε_{ij} are components of the strain tensor in orthogonal coordinate system of the specimen then the ε'_{ij} components can be determined from the equation

$$\varepsilon'_{ij} = \sum_{k,l=1}^{3} a_{ik} a_{jl} \varepsilon_{kl}, \tag{3.30}$$

where a_{ij} are directional cosines between axes of both coordinate systems and for measured strain we can write

$$\varepsilon'_{33} = \sum_{k,l=1}^{3} a_{3k} a_{3l} \varepsilon_{kl}. \tag{3.31}$$

It can then be shown that

$$\varepsilon'_{33} = \varepsilon_{\phi\psi} = \frac{d_{\phi\psi} - d_0}{d_0} = (\varepsilon_{11}\cos^2\phi + \varepsilon_{12}\sin 2\phi + \varepsilon_{22}\sin^2\phi - \varepsilon_{33})\sin^2\psi + \\ +\varepsilon_{33} + (\varepsilon_{13}\cos\phi + \varepsilon_{23}\sin\phi)\sin 2\psi. \quad (3.32)$$

Transformation into the equation for the residual stress requires models of grain interaction, nevertheless in general we can write

$$\varepsilon_{\phi\psi} = \frac{1}{2}s_2^{hkl}(\sigma_{11}\cos^2\phi + \sigma_{12}\sin 2\phi + \sigma_{22}\sin^2\phi - \sigma_{33})\sin^2\psi + \sigma_{33} \\ +\frac{1}{2}s_2^{hkl}(\sigma_{13}\cos\phi + \sigma_{23}\sin\phi)\sin 2\psi + \\ +s_1^{hkl}(\sigma_{11} + \sigma_{22} + \sigma_{33}), \quad (3.33)$$

where s_{ij} are the so-called X-ray elastic constants. If the z axis is identical with one of the principal axis of stress tensor then $\sigma_{13} = \sigma_{23} = 0$ and also $\sigma_{33} = 0$. Then there exists only biaxial stress in the material:

$$\varepsilon_{\phi\psi} = \frac{1}{2}s_2^{hkl}\sigma_\phi \sin^2\psi + s_1^{hkl}(\sigma_1 + \sigma_2), \quad (3.34)$$

where $\sigma_\phi = \sigma_{11}\cos^2\phi + \sigma_{12}\sin 2\phi + \sigma_{22}sin^2\phi$ or $\sigma_\phi = \sigma_{11}\cos^2\phi + \sigma_{22}\sin^2\phi$.

This relation is a basis of the so-called $sin^2\psi$- method, i.e., usage of linear dependence of the interplanar spacing on $sin^2\psi$. If the stress tensor is also symmetric in the plane of sample surface, the stress is uniaxial with $\sigma_{11} = \sigma_{22} = \sigma$ and the equation becomes

$$\varepsilon_{\phi\psi} = \frac{1}{2}s_2^{hkl}\sigma \sin^2\psi + 2s_1^{hkl}\sigma \quad (3.35)$$

For the practical application of the method it is assumed that the X-ray elastic constants are known. For elastically isotropic material they can be simply calculated as follows

$$s_1 = \frac{\nu}{E} \qquad \frac{1}{2}s_2 = -\frac{1+\nu}{E}, \quad (3.36)$$

where ν is the Poisson number and E Young modulus.

We also need the value of stress-free interplanar spacing (d^0). For simple isotropic stress this can also be replaced by d_{00}, i.e., the spacing measured for zero plane inclination to the surface ($\psi = 0$).

For elastically anisotropic materials again some model of grain interaction is necessary. There are several models but usually two extreme

approaches are used with some adjustable weight factor mixing them: the Reuss (R) and the Voigt (V). The former assumes that the stress in all randomly oriented crystallites is the same as a mean stress in the sample, which means that strain which is directly measured can be *hkl* dependent. The latter model assumes that strain is the same – and the stress then can be different in different crystallites. Thus in the Reuss case we can find different stress values for different measured crystal lattice planes (*hkl*).

The relations for X-ray elastic constants are quite simple for cubic materials for both R and V models. In our case we had to use more complicated relations for tetragonal materials, in particular, for the Laue class 4/*mmm*. They are given in [45].

In practice, we can often see nonlinear dependences of the measured strain on $\sin^2\psi$, which can be caused by several reasons. Relatively simple is the case of general triple axis stress when we must use equation (3.33) instead of (3.35). This can be distinguished by the so-called ψ splitting, i.e., different dependences of the strain on $\sin^2\psi$ for positive and negative values of ψ. If more measurements for different ψ and ϕ angles are performed then, in principle, the full stress tensor can be determined (e.g., also [46, 47]) Another reason for deflection from the linearity can be the presence of stress gradient causing curvature of the dependence close to origin because of different penetration depths for different ψ [48]. The most difficult is the case when a stronger texture and elastic anisotropy are present; that causes non-regularly oscillating dependence. Such a dependence can be simulated if we know the texture (as the orientation distribution function, ODF) for different assumed stress. However, there is no direct way to determine the stress directly from such d vs. $\sin^2\psi$ dependence. Moreover, it has been shown that fitting a straight line into such oscillating dependence may lead to wrong results (e.g., [49, 50]).

3.6 X-ray reflectivity

X-ray reflectivity (XRR) is an important X-ray method for studying the structure of thin films and multilayers. Similarly to the reflectivity in optics, its based on dispersion of X-rays close to the area of total scattering. The basic principle lies in the interference of the radiation reflected at each interface of the layered structure. The method is very sensitive to details of the multilayer structure, namely to the thickness, roughness and density of the layers.

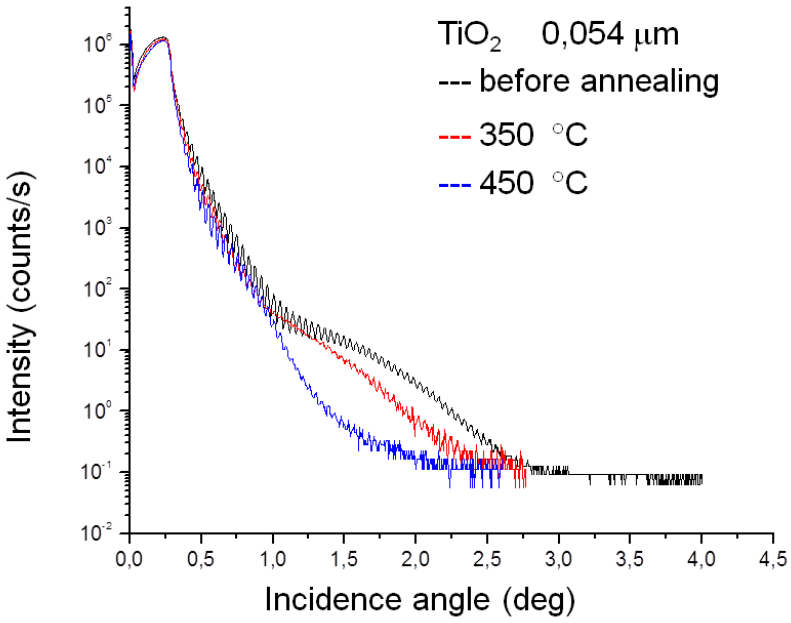

Figure 3.7: Reflectivity curve of 54 nm titanium dioxide thin film, before annealing (black curve) and after annealing at 350°C and 450°C. The small oscillations are so-called Kiessig fringes.

The reflectivity technique does not require any particular preparation of the sample but the surface of the sample must be smooth and the layer must be homogeneous. It is non-destructive and usually quite fast technique. The instrumental requirements for XRR measurement are monochromatic X-ray source with a small divergence, which guarantees a good angular resolution, and also a very thin incidence X-ray beam so that it is scattered entirely within the sample even at very small incidence angles [51].

The reflectivity is a function of the grazing incident angle and the surface roughness as it is shown in the following derivation. For refractive index n it can be written

$$n = 1 - \delta - i\beta = 1 - r_0\lambda^2/2\pi N_{at}(f_1 + if_2), \tag{3.37}$$

where r_0 is electron radius, λ is wavelength of the radiation, N_{at} is atomic number density and $f_1 + if_2$ is atomic scattering length including the dispersion correction. (The refractive index of real materials in X-ray

region is always less than one.) When the incidence angle is equal to the critical angle θ_c it can be written

$$\sin\theta_c = \sqrt{2\delta}. \tag{3.38}$$

The effect of surface roughness is easier to analyze farther from the total reflection region where the reflectivity decreases to lower values and the interaction of the electromagnetic wave with matter is weaker. For reflectivity the following formula can be derived

$$R = R_0 e^{-\frac{16\pi^2\sigma^2\sin^2\theta_i}{\lambda^2}}, \tag{3.39}$$

where R_0 is the reflectivity of the ideally smooth surface, θ_i is the incidence angle and σ is the surface roughness.

As a consequence of interference of waves reflected from the top and bottom interfaces, oscillations can be observed on reflectivity curves – these oscillations are known as Kiessig fringes (see Fig. 3.7). The relation of angular position α_{im} of the maximum of m-th interference and the film thickness t can be expressed as

$$2t\sqrt{\sin^2\alpha_{im} - \sin^2\alpha_c} = m\alpha, \tag{3.40}$$

where α_c is the critical angle. Therefore, from the reflectivity measurements the film roughness, density and thickness can be estimated [52].

Chapter 4

Whole pattern fitting

The films investigated in this work were relatively thin: from tens to hundreds of nanometers, and therefore, conventional symmetric $\theta - 2\theta$ scans (Bragg-Brentano) were not very suitable. Instead, the parallel-beam geometry with an incident beam mirror and a diffracted beam collimator was used and 2θ scans at low angles of incidence were applied in order to obtain information from the low penetration depths predominantly, which is crucial for study of thin films. The drawback of this technique is its several times poorer resolution.

Moreover, for the present TiO_2 samples the diffraction peaks were broadened due to strains and small crystallite sizes, and display considerable overlapping, as it will be shown in the following chapters. In such cases, the analysis of individual peaks or fitting of peak clusters can hardly be applied, and the diffraction patterns should be evaluated by nowadays popular whole pattern fitting.

There are several groups of whole pattern fitting programs available. The most famous ones are Rietveld type programs such as FULLPROF [53] and GSAS [54], which are mainly dedicated for crystal structure determination and also can be used for quantitative phase analysis. These programs include phenomenological description of the anisotropic line broadening, and thus can be used for estimation of crystallite size and microstrains.

In the second group the programs [55, 56] usually do not include structural part of the refinements but are concentrated on physically correct description of the real structure parameters, such as the distribution of crystallite sizes, or the presence of dislocations and stacking faults.

None of all these programs is suitable for the study of thin films, though. The fitting procedure requires appropriate evaluation of the 2θ scans taken for thin films at low angles of incidence and should include absorption correction, refraction correction, consideration of residual stress and texture. For this case, only the program [57] with many suitable options is available. However, it suffers from the lack of documentation, and also some additional models such as dislocation broadening are not included. Therefore, we have decided to write our own software for total diffraction pattern fitting and modelling. This was mainly developed by Z. Matěj in M'Struct software [58].

4.1 Software description, effects and parameters

The program has been written as an extension of the FOX system and it is used to solve several problems. It can be downloaded from webpage www.xray.cz/mstruct free of charge.

The core principle of the whole pattern fitting is that all relevant effects are usually modelled in the real space and the diffraction profiles are calculated directly by means of the Fourier transform and subsequently compared with the measured data. Besides effects affecting peaks positions, such as residual stresses and instrumental aberrations, and peak intensities (texture), the model function should include all necessary instrumental and physical parameters – by convoluting the instrumental function with physical profiles. Various other defects such as dislocations and stacking-faults have characteristic influence on the width and position of different *hkl* diffraction lines, and therefore, they can be often also distinguished [32, 55, 56].

4.1.1 Peak positions

Peak positions are determined by variable unit-cell parameters and zero shift error is not considered for the parallel-beam geometry but included for symmetrical θ-2θ scans. For low angles of incidence, close to the angle of total reflection, the refraction correction must be included. This is done via relation

$$\Delta 2\theta = \alpha - \frac{1}{\sqrt{2}} \sqrt{(\alpha^2 - 2\delta) + \sqrt{(\alpha^2 - 2\delta)^2 + 4\beta^2}}, \tag{4.1}$$

where α is the angle of incidence and δ and β are real and imaginary parts of refraction index. The shifts due to the refraction have the same effect as the zero-shift error and they are both independent of diffraction angle. However, the inclusion of refraction effect has several advantages, for example in the case of multiple angles of incidence or multilayers.

4.1.2 Peak intensities

The structure factors are calculated and used as constraints for the peak positions and intensities. The effects of absorption and texture can be included.

Absorption

The intensity correction for diffraction from one layer with thickness T_i can be calculated (if the refraction effects are neglected) from the path length of both the incident and diffracted beams through the film

$$I_i = \frac{T_i^p}{\sin \omega} [1 - \exp(T_i / T_i^p)], \tag{4.2}$$

where ω is the angle of incidence and T_i^p is the so-called penetration depth for a given layer:

$$\frac{1}{T_i^p} = \mu_i \left[\frac{1}{\sin \omega} + \frac{1}{\sin(2\theta - \omega)} \right]. \tag{4.3}$$

Texture

In general, the texture correction can be obtained from a known model of the ODF after appropriate integration over all crystallites with diffracting $\{hkl\}$ planes perpendicular to the direction of the measured diffraction vectors. For asymmetric scans this is, of course, different from the situation for the conventional Bragg-Brentano geometry. At present, a simple ”brute force” numerical integration algorithm for such task is implemented in the system. Currently, only a simple model using the Gaussian distribution of crystallites and possible inclinations of texture with respect to the sample normal is available for the refinement.

If the texture is unknown or difficult to describe, the peak intensities can be varied also independently by multiplication of intensities of individual peaks by refinable factors. This is called an "arbitrary texture", e.g., in the MAUD software. Of course, this can lead to more correlations between parameters in the fitting.

4.1.3 Line profiles

Peak profiles are given by numerical convolution of a known instrumental function and physical profiles (see Section 3.3). In principle, the total profile of *hkl* reflection can be expressed as follows:

$$I_h kl(\Delta s) = \int_{-\infty}^{\infty} T_{pV}^{IP} A_{hkl}^{D} A_{hkl}^{s} \left[A_{hkl}^{\mathrm{SF}} \cos(2\pi L \Delta s) - B_{hkl}^{\mathrm{SF}} \sin(2\pi L \Delta s) \right] dL, \quad (4.4)$$

where T corresponds to the instrumental profile, A^D is the Fourier transform of size broadening and A^s is the FT of strain broadening. Fourier terms with indices SF correspond to the stacking faults

Instrumental function

Instrumental function is described by the pseudo-Voigt (pV) function as a weighted sum of the Gauss and Cauchy functions

$$pV(x) = \eta G(x) + (1 - \eta) C(x), \quad (4.5)$$

$$C(x) = \frac{k}{\pi} \left(\frac{1}{1 + k^2 x^2} \right), \quad (4.6)$$

$$G(x) = \frac{k}{\sqrt{\pi}} \exp[-k^2 x^2]. \quad (4.7)$$

The 2θ-dependent parameters, the full width at half maximum (FWHM), mixing parameter η in the pseudo-Voigt, and asymmetry A, are given by the commonly used relations:

$$FWHM = W + V \tan\theta + U \tan^2\theta, \quad (4.8)$$

$$\eta = \eta_0 + \eta_1 2\theta, \quad (4.9)$$

$$A = A_0 + A_1/\sin(2\theta) + A_2/\sin^2(2\theta). \tag{4.10}$$

The parameters U, V, W, η_0, η_1, A_0, A_1, and A_2 are determined by the fitting of standard diffraction pattern LaB_6 measured on the same instrumental arrangement as the one used for the measurement of the investigated samples.

Crystallite size

Physical effects can be conveniently modelled by the real space Fourier coefficients. The size broadening effect is described by the model function for log-normally distributed spherical crystallites with two refinable parameters: the *median of crystallite size* and the *variance* of the distribution, or alternatively by the distribution histogram.

Log-normal distribution can be described by the relation

$$g(D_{\mu\sigma}) = \frac{1}{D\sigma\sqrt{\pi}} \exp\left[\frac{-(\ln D - \mu^2)}{2\sigma^2}\right] \tag{4.11}$$

with corresponding Fourier coefficients:

$$\begin{aligned} A^D(L) &= \frac{m^3 \exp\left[\frac{9}{4}(\sqrt{2}\sigma)^2\right]}{3} \mathrm{erfc}\left[\frac{\ln|L|}{\sqrt{2}\sigma m} - \frac{3}{2}\sqrt{2}\sigma\right] \\ &- \frac{m^2 \exp[(\sqrt{2}\sigma)^2]}{2} |L| \mathrm{erfc}\left[\frac{\ln|L|}{\sqrt{2}\sigma m} - \sqrt{2}\sigma\right] \\ &+ \frac{|L|^3}{6} \mathrm{erfc}\left[\frac{\ln|L|}{\sqrt{2}\sigma m}\right], \end{aligned} \tag{4.12}$$

where $\mu = \ln(m)$. This relation looks cumbersome but it is not problematic and has just two parameters for fitting: μ and σ.

Strain, lattice defects

The strain broadening can be described by the dislocation model including three parameters: dislocation density ρ, cutoff radius R_e for the dislocation-correlation, and fraction of edge dislocations q assuming that possible dislocation types, and consequently, the contrast factors are known. Most frequently used relation for the Fourier coefficients is

$$A^s(L)_{hkl} = \exp\left[-\frac{1}{2}\pi b^2 \chi_{hkl} \rho L^2 d_{hkl}^2 f\left(\ln\frac{L}{R_e}\right)\right], \tag{4.13}$$

where b is the Burgers vector of dislocations (should be known or guessed, e.g, from transmission electron microscopy), d is the lattice spacing for the $\{hkl\}$ planes, and χ is the orientation factor, which depends on the orientation of the dislocation line with respect to the Burgers vector (type of the dislocation) and the diffraction vector. These factors depend also on elastic characteristics of the material and have been calculated for several structure types and materials. f is quite complicated function taking into account correlation in dislocation arrangements.

However, since the types of crystal defects in TiO_2 crystalline phases, that are related to microstrain, are not known and cannot be simply observed, the phenomenological microstrain broadening function is used (see Section 3.3). It would be necessary to know the analytical expression for the dependence of $\varepsilon^2(L)$, though. In M'Struct a simplified procedure was implemented. The peak broadening, dependent on the diffraction vector magnitude, was modeled by the pV function. Its FWHM dependence with diffraction angle 2θ is given by the Cagliotti polynomial containing only the quadratic term U. This means that the FWHM in reciprocal space units is linearly increasing with the diffraction vector magnitude. The shape factor η of the pV function common for all $2\theta_{hkl}$ diffraction peaks of a particular phase can also be refined. The relation for FWHM can be converted into the integral breadth and one parameter, microstrain e, is determined:

$$FWHM = U\tan^2\theta; \quad \beta(2\theta) = 4e\tan\theta$$
$$4e = \left(\frac{1-\eta}{\phi_G} + \frac{\eta}{\phi_C}\right)\sqrt{U}, \tag{4.14}$$

where $\phi_G = 2\sqrt{\frac{\ln 2}{\pi}}$ and $\phi_c = \frac{2}{\pi}$ are the well-known Gauss and Cauchy shape parameters, respectively.

4.1.4 Residual stress

The stress can cause shift of peaks in a 2θ scan varying with 2θ according to the sign and magnitude of the stress. However, it can also result in a significant anisotropy of these shifts in case of elastic anisotropy. Imposing constraints on the peak positions and/or intensities in total pattern fitting of TiO_2 films with severe peak overlaps is absolutely necessary as can be seen from a typical segment of the diffraction pattern, shown in Fig. 4.1.

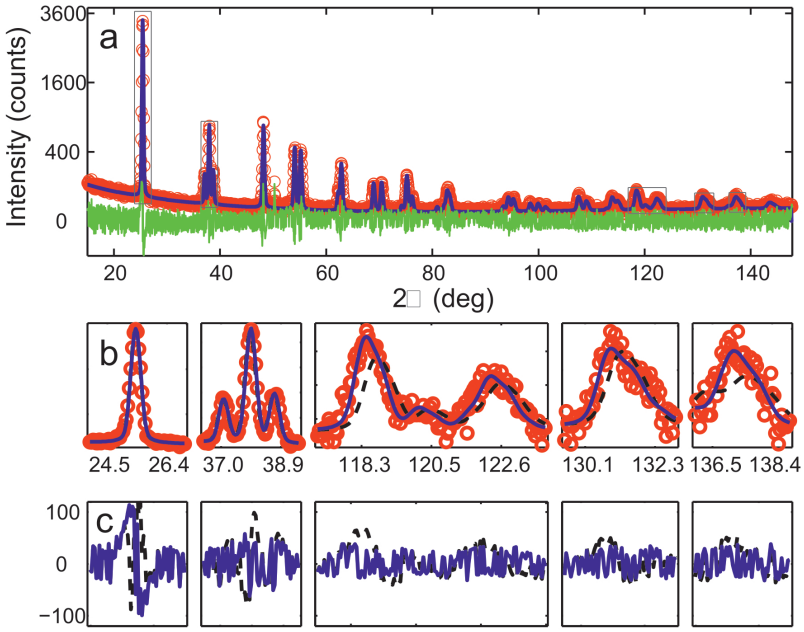

Figure 4.1: An example of comparison of measured and calculated diffraction patterns (a). The (b) panel displays details of the selected parts of the (a) plot in case the residual stress in the film is included (solid line) and in case no residual stress is assumed and only unit-cell parameters are refined (dashed dark line). Difference plots for these two cases in the (b) plot is shown in (c) panel.

The effect of residual stress in the current version of M'Struct is included for a simple symmetrical biaxial stress in the plane of a sample surface (see Section 3.5). In the case of a 2θ scan the inclination angle ψ can be written as $\psi = \theta - \omega$, where ω is the fixed angle of incidence.

Each *hkl* reflection in a powder pattern measures the interplanar distance d_{ψ}^{hkl} of (*hkl*) lattice planes, the normal of which is inclined by an angle $\psi^{hkl} = \theta^{hkl} - \omega$ to the sample surface normal. From the model the stress-free unit-cell parameters (stress-free interplanar distance d_0^{hkl}) can be calculated. By combining information from multiple *hkl* reflections, the residual stress parameters can be determined from a single powder pattern. X-ray elastic constants s_1^{hkl}, s_2^{hkl} are calculated in two extreme models of grain interactions: Reuss and Voigt (see Section 3.5) and weight factor of these limiting cases is refined.

Chapter 5

TiO_2 sample preparation

There are many sophisticated techniques how to prepare TiO_2 thin films, e.g., vacuum evaporation, magnetron sputtering, molecular beam epitaxy, laser-assisted vacuum evaporation, chemical vapor deposition, chemical bath deposition, spin-coating process, sol-gel process etc. [59, 60], and the quality and character of the samples strongly depends on the preparation method. Each preparation method has its advantages and disadvantages, for example, the technical advantages of sol-gel process are simplicity, good chemical and mechanical stability, high porosity and ease of control of the microstructure and stoichiometry [61], while the thin films prepared by this method are often not homogeneous and of lower quality.

Samples in this work were prepared by dc-pulsed reactive dual magnetron by Dr. Šícha from the Faculty of Applied Sciences at University of West Bohemia. More about the samples preparation, stabilization of the deposition process, the correlation between the deposition process parameters, film structure and film properties is discussed in some of his works. [1]

Compared to other preparation techniques the magnetron sputtering process has many advantages for the deposition of oxide coatings [62, 63]. A very good adhesion, crystalline structure and thickness uniformity of the oxide coatings can be achieved, in contrast to wet deposition processes (example sol-gel, painting, spraying, and thermal decomposition), and problems such as delamination, non-uniformity and requirement for post-deposition annealing can be effectively eliminated [64, 65, 66]. Besides, the magnetron method is versatile as different kind of oxides can be deposited by simply changing the target materials, without exposi-

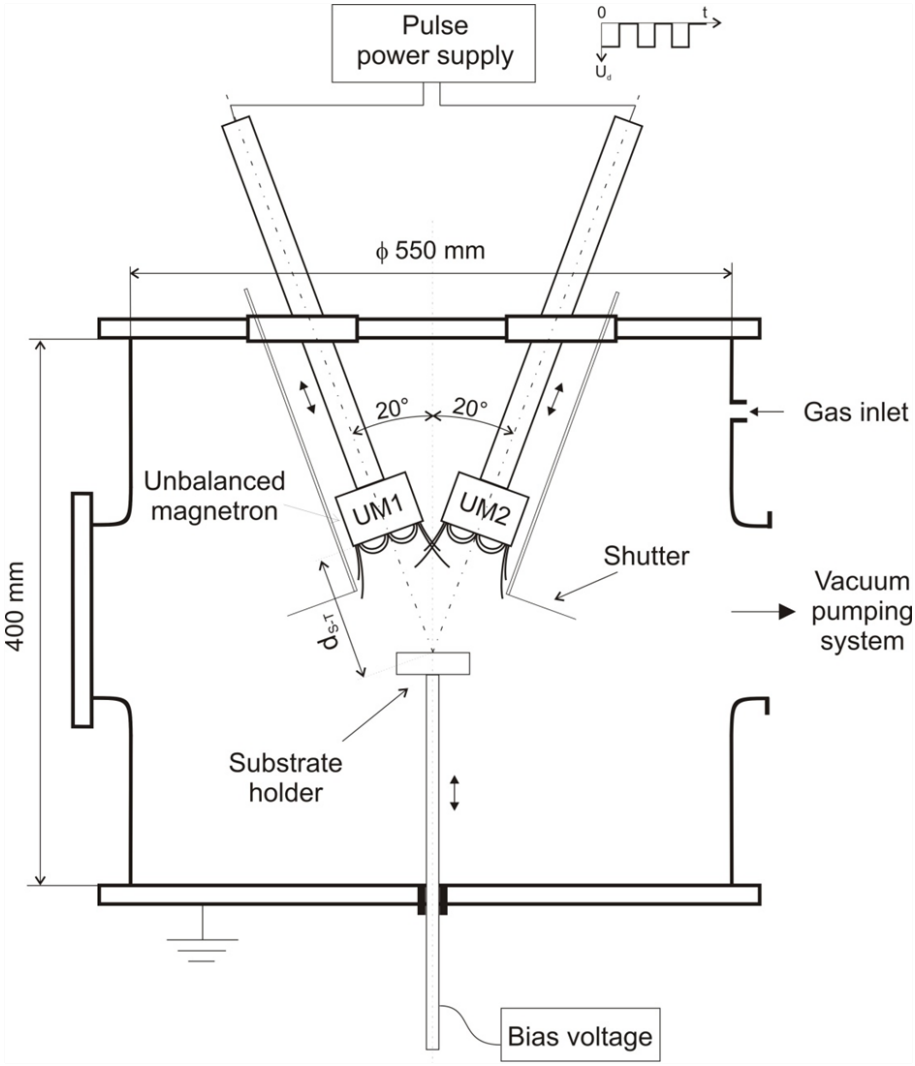

Figure 5.1: The scheme of the deposition chamber in the dual magnetron system.

tion to toxicity or flammability, inherent to the metal precursors required in chemical vapour deposition (CVD) or without the environmental concerns of electroplating processes [67, 68]. The illustration of the deposition chamber of the pulse dual magnetron (DM) system is shown in Fig. 5.1.

According to the authors the film depositions were made in a grounded cylindrical stainless steel vacuum chamber with h = 400 mm and ϕ = 550 mm with four lateral and two top/bottom flanges as it is shown in Fig. 5.1.

The function of the top and bottom flange is that it makes possible

to configure the position of the substrate holder and the dual magnetron (DM). It is possible to heat the substrate or apply bias voltage. The substrate holder is also electrically isolated from the grounded chamber. The vertical position of the substrate holder can be adjustable. This enables the control of the substrate-target distance d_{s-t}. According to the authors of the samples [1] this distance was for most of the experiments kept at 100 mm. The tilt of DM's magnetrons from the substrate axis was 20°. More details about the pulsed dual magnetron, about the gas feeding system and the feedback control of the reactive gas flow can be found in [1].

Chapter 6

Films prepared with different partial oxygen pressure

The crystallinity and phase composition of the TiO_2 films, as well as the surface properties, strongly affect the film photoactivity [69, 70]. However, not only the phase composition governs the desired properties, also the microstructure affects the photoactivity of the film. For example, films composed of mixture of the anatase and rutile had almost as good photoactivity as pure anatase films, which was explained as higher film surface roughness (R_a) and higher surface area of the mixture films [1]. Or similarly, anatase films with structure close to X-ray amorphous had almost the same photoactivity as films with good anatase structure, due to their fine microstructure.

In our previous experiments [71] it was shown that structure of the films gradually changes from an amorphous one through the mixture of anatase and rutile phase toward the films with dominant anatase phase, in dependence on the thickness h of the film. The dependence of phase crystallinity on thickness h had then a strong effect on resulting properties: with increasing h the film photoactivity improved, as was manifested by faster decrease of the water droplet contact angle. Therefore, to avoid the undesired influence of varying thickness, all films were prepared with the same thickness $h = 1$ μm. The composition and properties of the films were modified by preparation under different partial oxygen pressure.

In this chapter TiO_2 films with equal thickness but different deposition conditions are studied. The samples were prepared with different partial oxygen pressure, which resulted in different composition and properties,

as observed and described in the following text. The phase composition, size of the crystallites and reflectivity was evaluated and compared with hydrophilicity measurements.

Sample preparation

As well as in our previous work [71], the samples were prepared by magnetron sputtering. However, this time, the partial oxygen pressure was changed during the deposition process and the effect of this parameter on structure (studied in detail by various X-ray methods) and the final superhydrophilic behaviour was observed.

All TiO_2 films were 1000 nm thick and were deposited at higher total working pressure $p_T = 0.9$ Pa. The $p_T = 0.9$ Pa was chosen as the maximum pressure, enabling a stable feedback control of the partial oxygen pressure p_{O_2}. Three samples were deposited: with low ($p_{O_2} = 0.05$ Pa), medium ($p_{O_2} = 0.085$ Pa) and high ($p_{O_2} = 0.15$ Pa) partial oxygen pressure with deposition rates $a_D = 45$, 20 and 9 nm/min, respectively.

6.1 X-ray results

The X-ray measurements were performed on Panalytical X'Pert MRD diffractometer in parallel beam setup by the 2θ scans with the angle of incidence fixed at 0.5°. More about the parallel beam setup can be found in Chapter 3.

All three samples were measured as prepared and also after annealing at 400 °C for 30 minutes in air. The phase composition was determined and the measured diffraction patterns were evaluated by means of total pattern fitting using M'Struct program [58], in order to obtain also the crystallite size and microstrain. More details about the fitting can be found in Chapter 4.

The sample with low partial oxygen pressure was found to be amorphous as deposited and after the annealing the film was well crystallized anatase with crystallite size 350 nm and microstrain 0.16 %, see Fig. 6.1 top.

The sample prepared at medium partial oxygen pressure was already partially crystallized even as prepared and a mixture of anatase and rutile was observed in the diffraction pattern (see Fig. 6.1 middle). After annealing the crystallization improved, as the size of the rutile crystallites grew from 6 to 10 nm and the anatase crystallites grew from 20 to 37 nm;

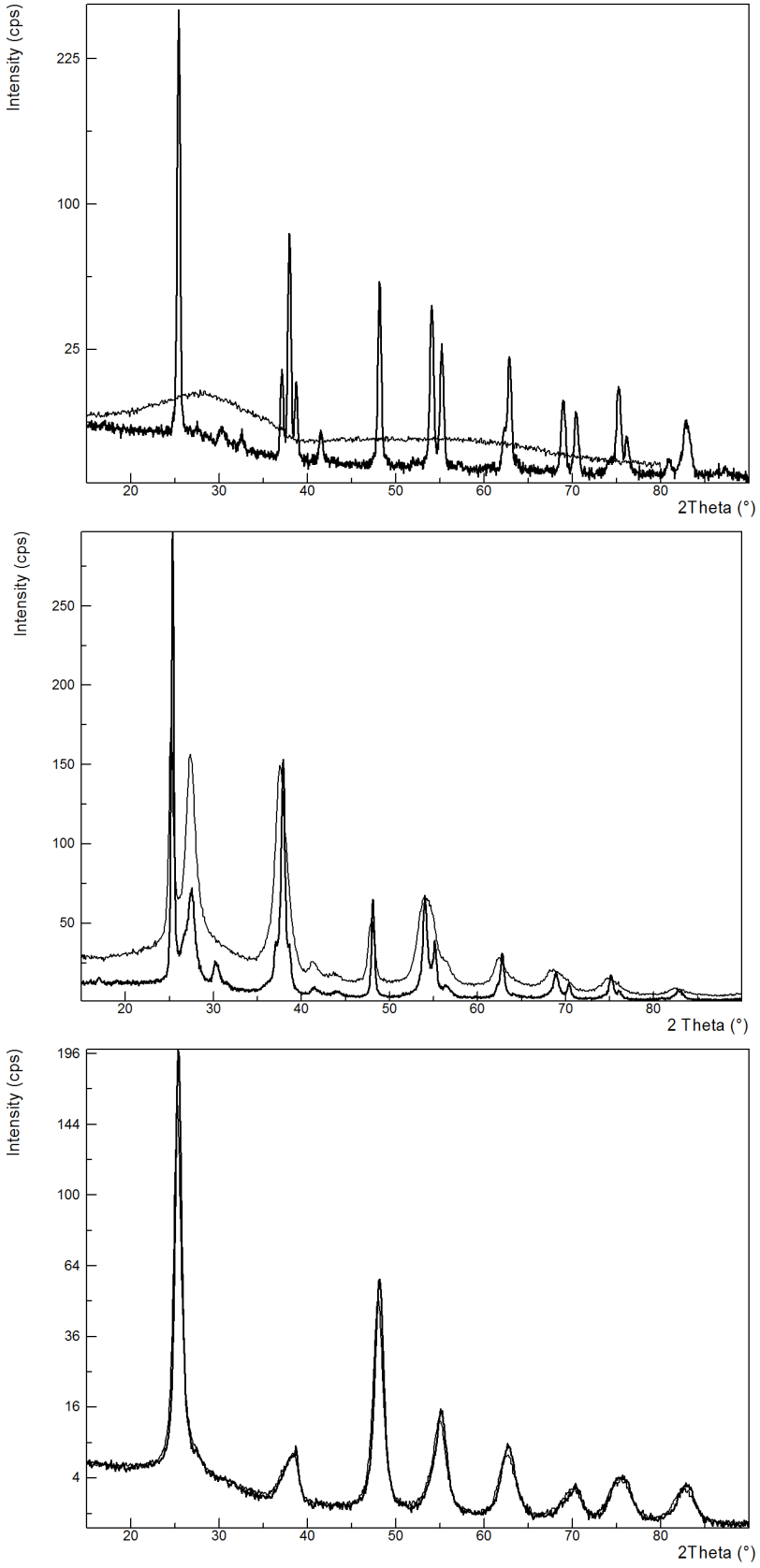

Figure 6.1: The diffraction patterns of 1000 nm thin films, prepared with low (top panel), medium (middle) and high (bottom) partial oxygen pressure. Each sample was measured as prepared and after annealing at 400 °C (thicker curve).

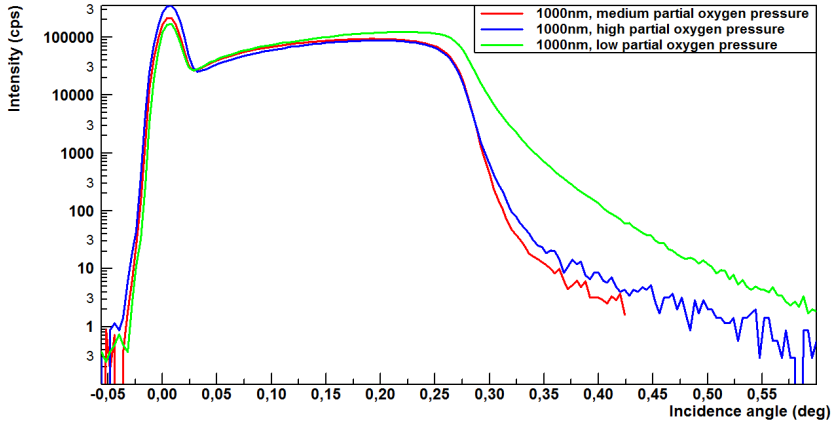

Figure 6.2: The reflectivity curves for 1000 nm thin samples, prepared with different partial oxygen pressure.

the corresponding microstrain dropped from 0.6 to 0.13 %. Rutile has significantly smaller crystallites, which seems to be typical for a mixture of both phases.

The high partial oxygen pressure leads to a well crystallized as prepared sample, with anatase being the dominating phase in the film (Fig. 6.1 bottom). Unlike for the other two samples, here the subsequent annealing at 400 °C did not have significant effect on microstructural parameters: size of the crystallites changed only slightly from 8.8 to 10.5 nm and microstrain remained 0.3 %.

Reflectivity

To obtain the information about the structure of surface, which is important for the superhydrophilicity and related properties, the reflectivity measurements were performed, again before and after the annealing at 400 °C. (For details about reflectivity measurements see Section 3.6.) The measured reflectivity curves for the whole set of as prepared samples are shown in Fig. 6.2. It can be seen that the roughness of the samples prepared at medium and high partial oxygen pressure is similar and is higher than that of prepared at low pressure.

After the annealing, the samples prepared with low and high pressure had their reflectivity re-measured under the same conditions (see Fig. 6.3). While the reflectivity of the low pressure sample changed with annealing, surface of the high pressure sample remained almost intact.

The measured reflectivity curves were fitted by X'Pert Reflectivity

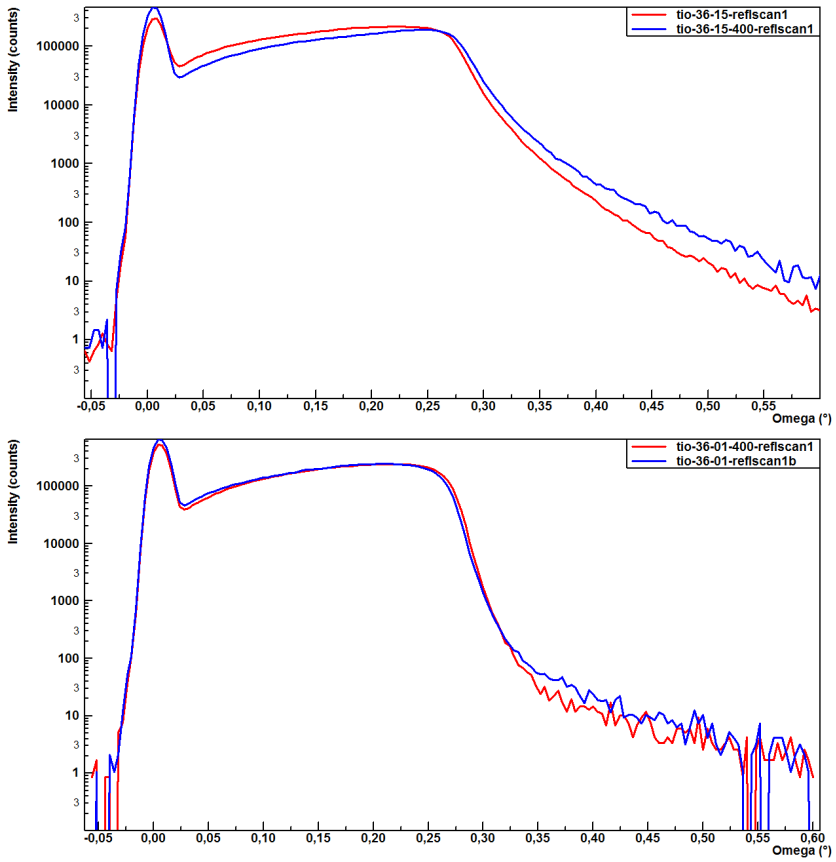

Figure 6.3: The change of reflectivity curves with annealing for samples prepared with low (top panel) and high (bottom panel) partial oxygen pressure.

program and the roughness and density of the surface was evaluated. Thickness of the samples was not fitted due to the absence of visible thickness oscillations; the resulting fits are shown in Fig. 6.4. The observed change of reflectivity with annealing for the low pressure sample is due to change of surface roughness (from 4.2 to 3.9 nm), while the surface density remained constant (~3.66 g/cm^3).

Hydrophilicity

After annealing the high pressure sample displayed excellent hydrophilicity properties with contact angles of water droplet 12, 8 and 7 degrees after UV irradiation of 20 minutes, 1 and 5 hours, respectively. The medium pressure sample showed slightly worse hydrophilicity values (30, 10 and 9 degrees for the same UV irradiation), while the low pressure sample

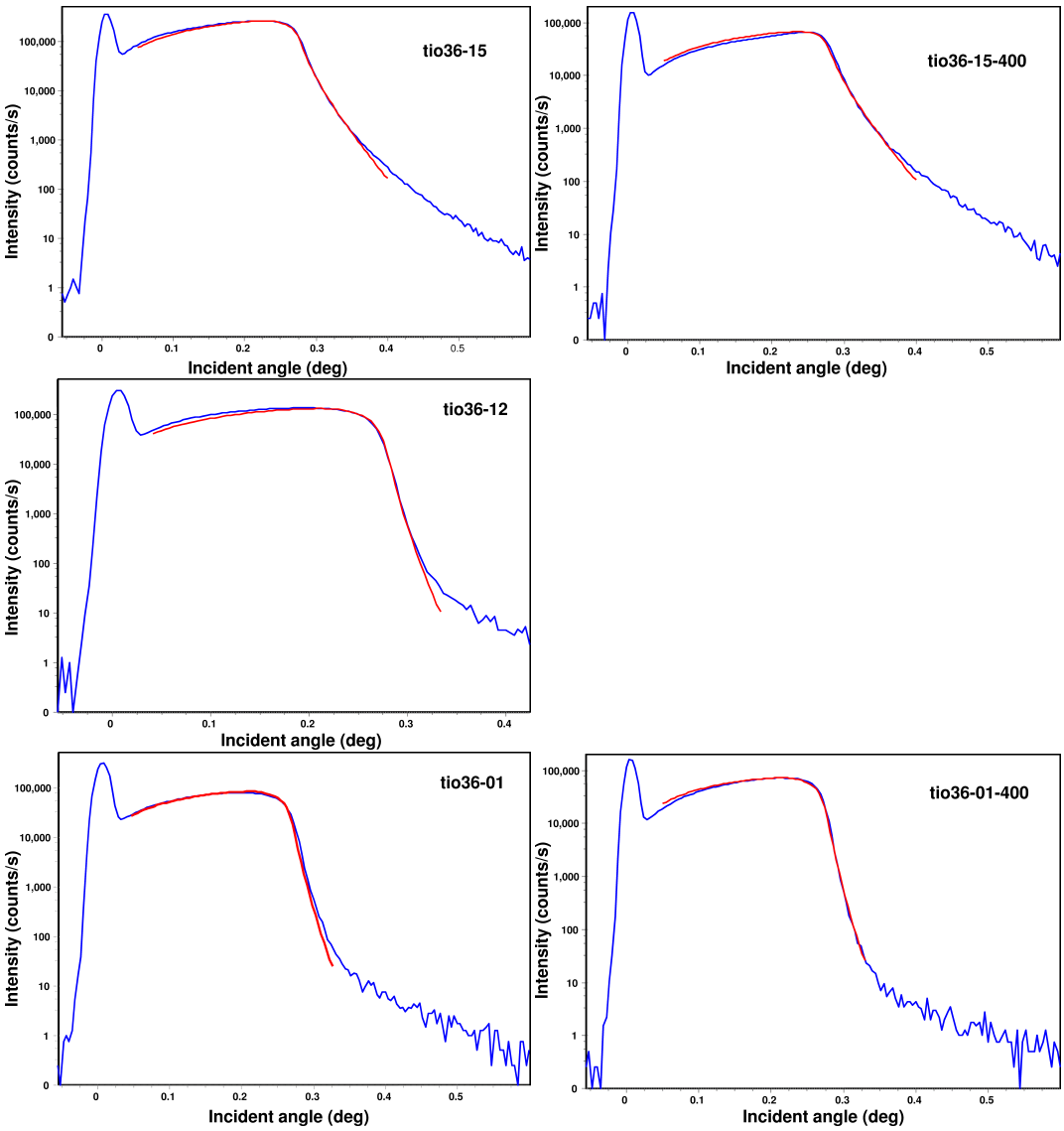

Figure 6.4: The reflectivity curves for samples prepared with low (top left panel as prepared, top right panel annealed), medium (middle left panel as prepared) and high partial oxygen pressure (bottom panels). Blue curve is the measured data, red curve is the fit.

had the worst hydrophilicity (82, 80 and 70 degrees). This outcome is connected with the high pressure sample being the purest anatase from all three samples and having the smallest crystallites.

6.2 Summary

Different partial oxygen pressure upon preparation affected strongly the composition of the studied films: the lowest pressure resulted in amorphous sample, medium pressure lead to a partially crystallized sample with a mixture of rutile and anatase phases, and only the highest partial oxygen pressure yielded a well crystallized as prepared sample with dominating anatase. From reflectivity measurements of as-prepared samples the roughness of medium and high pressure samples was similar and higher than that of prepared at low pressure.

In the first two cases, annealing at 400 °C improved the crystallinity and roughness, while the latter (highest pressure) sample the annealing did not have significant effect on microstructural parameters nor surface quality. Only the high pressure sample displayed excellent hydrophilicity which is connected with this sample being the purest anatase from all three samples and having the smallest crystallites.

Chapter 7

Films prepared as nanocrystalline

The unique properties of titanium dioxide thin films, such as superhydrophilicity, are bound to crystalline (or even nanocrystalline) material only. The first experiments lead mainly to deposition of amorphous films which were later subjected to annealing in order to obtain nanocrystalline films. This approach related also to thermal stability of films was studied in detail in next chapters. Finally, by suitable setting of deposition parameters nanocrystalline films could be obtained directly. In this chapter, the films of different thickness from 100 to 2000 nm were deposited on a silicon or glass substrate and thermal stability of these films was studied by in-situ XRD measurements.

After a short description of sample preparation and their basic characterization by X-ray phase analysis, the evaluation of X-ray line broadening is described and information on size of the crystallites is extracted. Structure and quality of films surface is analyzed from X-ray reflectivity measurements and the overall picture is complemented by analysis of residual stress, as well as evaluation of the texture. The results are put into context with results of hydrophilicity measurements.

Sample preparation

TiO_2 films were prepared by dual magnetron sputtering on unheated microscope glass slides $26 \times 26 \times 1$ mm^3 or silicone (100) substrates $26 \times 26 \times 1$ mm^3. The thickness of the samples was controlled by the time

of the sputtering process, while other parameters, such as total working pressure and pulse discharge current, were kept constant. Samples with thicknesses 100, 220, 515, 935, and 2000 nm were prepared. The maximum substrate surface temperature during the deposition was lower than $T_{surf} \approx 160$ °C. All samples were prepared by Dr. Šícha at West Bohemian University.

To enhance the crystalline character of the films, the samples were annealed up to 1000 °C. Samples were annealed in high temperature chamber in air at 100, 200, 318, 400, 500, 600, 700, 800, 900, 1000 °C. The films were annealed for 30 minutes at each temperature. The changes due to annealing are analyzed and discussed below.

7.1 Line profile analysis and phase analysis

In the following text we describe the characterization of the titanium dioxide samples, with respect to phase composition and size of crystallites. In addition, a rough phase analysis was also performed with various incidence angles, i.e., at various penetration depths.

The aim is not only to check whether any of the samples was amorphous, but also to observe how the phase composition and the size of crystallites influence the super-hydrophilic behaviour of the films.

The X-ray measurements were mainly performed on Philips (Panalytical) X'Pert MRD in parallel beam setup, 2θ scans with the angles of incidence $0.5 - 1.5°$ with parallel plate collimator placed in the diffracted beam and the Goebel mirror inserted in the primary beam. In titanium dioxide such values of incidence angles correspond to penetration depths 100–300 nm. The annealed samples were also studied with the Panalytical system MPD in double-mirror setup (with mirror also in the diffracted beam), since this arrangement has about three times better resolution, however, at the cost of reduced intensity.

As the samples are nanocrystalline thin films, stress and texture could be expected as well as pronounced line broadening and line shifts. As a consequence, the diffraction patterns cannot be simply evaluated with a standard software for powder diffraction. Therefore, all the diffraction patterns were evaluated by total pattern fitting method using M'Struct program, which has been developed by Dr. Z. Matěj in our group [58]. This advanced software allows to perform the fitting procedure even in such complicated cases. The example of fit for sample 2000 nm as

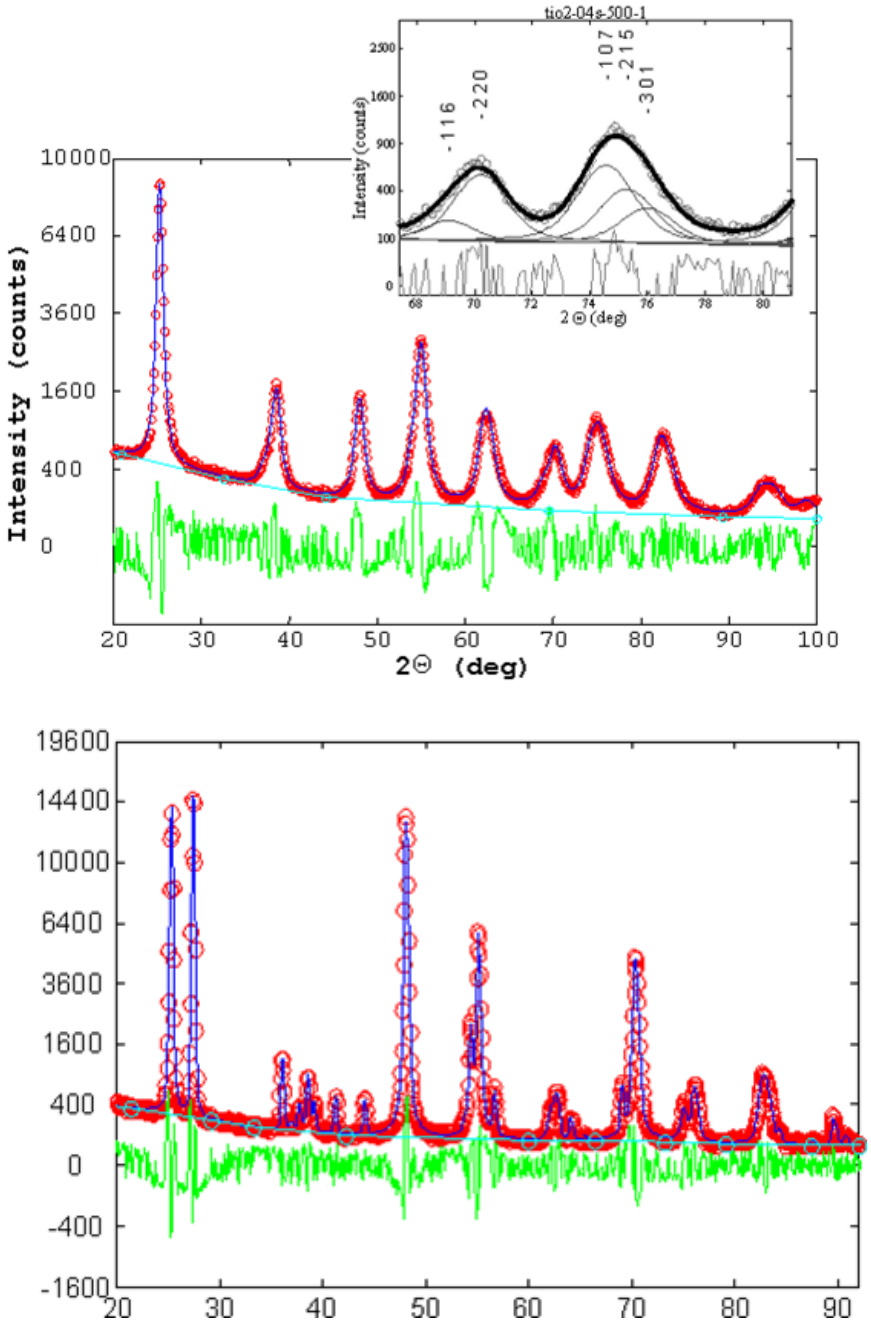

Figure 7.1: Fit of the diffraction pattern for 2000 nm thin film, as prepared (top and the inset detail) and after annealing at 800 °C (bottom). The incidence angle was 0.5 degrees.

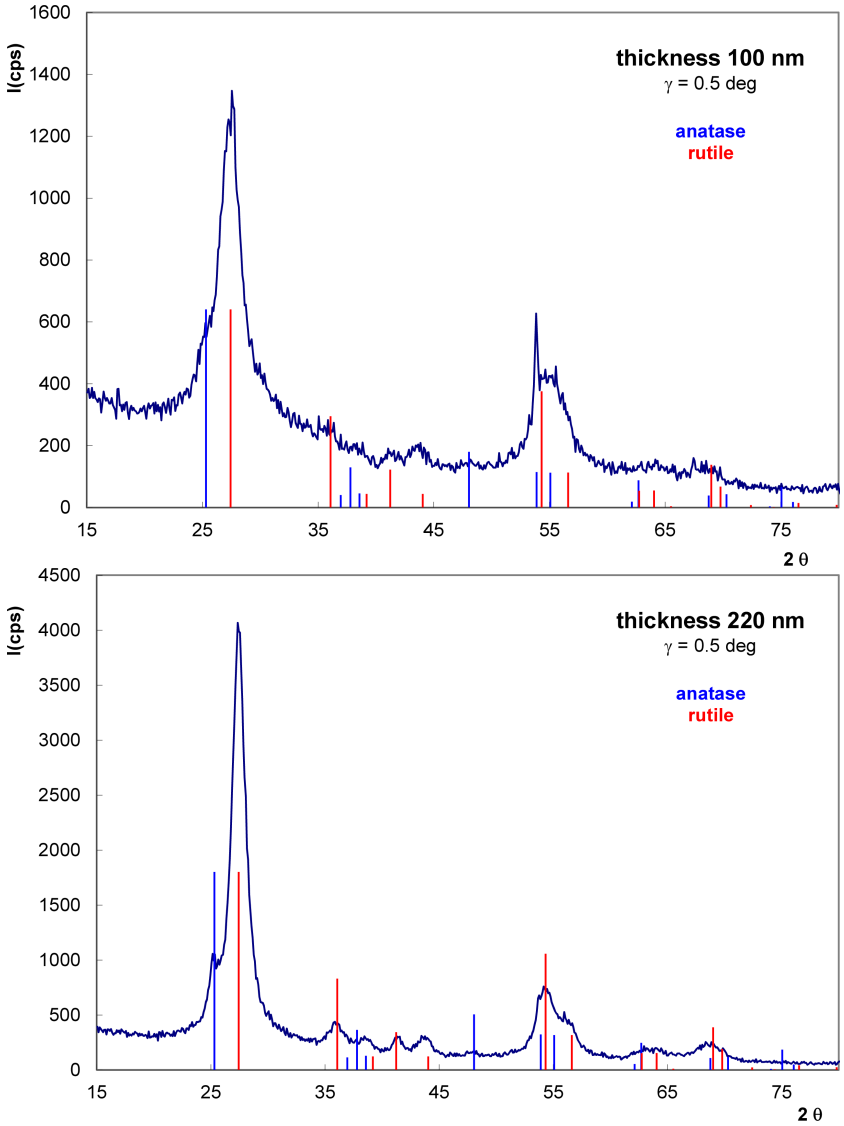

Figure 7.2: The diffraction pattern for as-prepared 100 nm (top) and 220 nm thin film (bottom). The incidence angle was 0.5 degrees. In both films broad rutile peaks are dominating, for 220 nm an indication of narrower anatase peaks can be noticed.

prepared and after annealing at 800 °C is shown in 7.1

Diffraction patterns of the nanocrystalline films with different thicknesses displayed considerable differences. The patterns for thinner films (thickness 100 and 220 nm) showed dominating rutile phase with a small indication of anatase, as can be seen in 7.2. On the other hand, in the films thicker than 500 nm mainly the anatase phase was observed (Fig. 7.3).

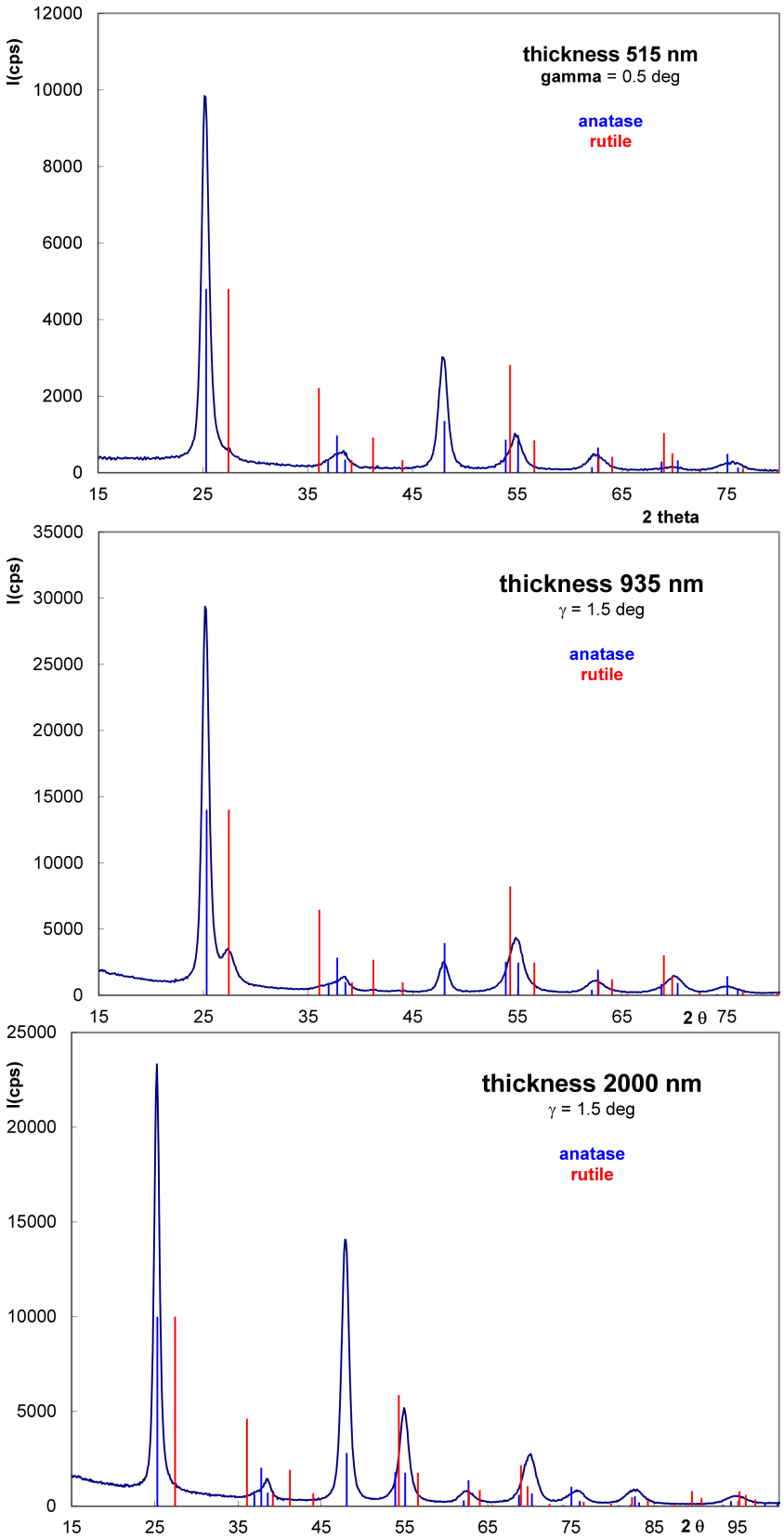

Figure 7.3: The diffraction pattern for as-prepared 515 nm (top), 935 nm (middle) and 2000 nm thin film (bottom). The incidence angle was 1.5 degrees. In all the anatase peaks are dominating, in case of 2000 nm there nearly no indication of rutile.

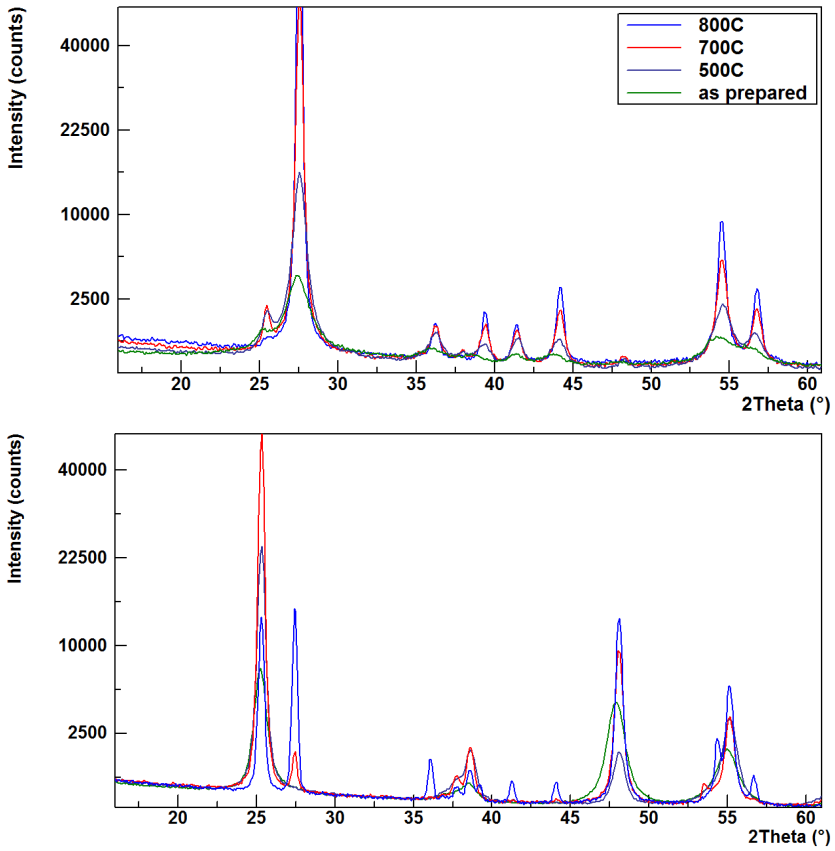

Figure 7.4: Evolution of phase composition of thin film (220 nm) with annealing (top panel). While the as prepared sample is a mixture of rutile and anatase, at highest annealing temperatures the sample almost entirely transforms to rutile. In the bottom panel analogous dependence is displayed for thick (2000 nm) sample, where anatase phase transforms to rutile at higher annealing temperatures.

With annealing there were no significant changes, neither in phase composition nor in microstructure of the films, up to the temperatures of 600 – 700°C, when the transformation of anatase phase into rutile starts. For thinner, rutile rich films the reduction of anatase can be well observed, as shown in Fig. 7.4 (top) with a comparison of diffraction patterns for as prepared 220 nm film and the sample annealed at temperatures 500, 700 and 800 °C. The 101 peak at 25.2° diminished after annealing at 700 °C and anatase phase completely disappeared at 1000 °C. For thicker, mostly anatase films the rutile peaks clearly appeared (e.g., 110 peak at 27.4°) after annealing at 700 °C (see Fig. 7.4 bottom, with example of 2000 nm sample). At 800 °C both phases coexisted in 2000 nm thick sample, at 900 °C the

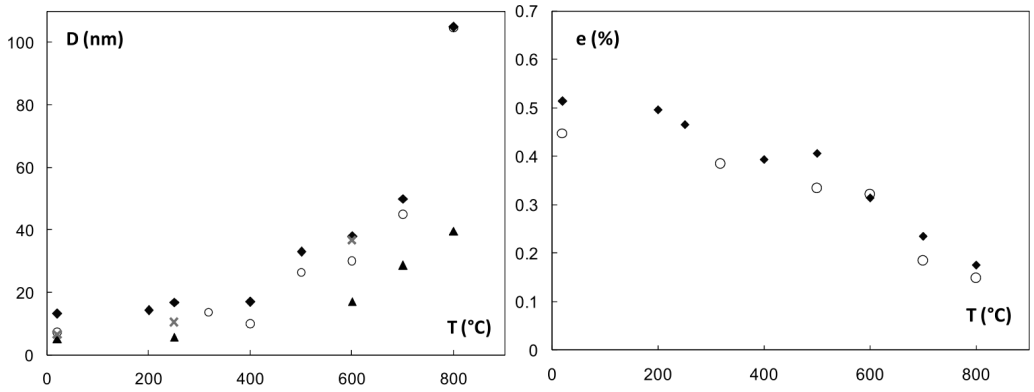

Figure 7.5: Dependence of crystallite size D (left) and microstrain e (right) on annealing temperature; for anatase – 2000 nm thick film (◆), 935 nm (○), 220 nm (×) and rutile 220 nm (▲).

anatase peaks were negligible, and entirely missing after annealing at 1000 °C.

For the conditions of preparation, the growth of anatase phase is preferred, however, it is likely that the lattice parameter of substrate is more suitable for growth of the rutile phase. Therefore, the thinner films contain a relatively large content of rutile, while the thicker films are more similar to a bulk (anatase) material.

The annealing process influenced not only the phase composition but also the crystallite size. The mean crystallite size in the as-deposited films was 5–7 nm, with exception of the thickest film where sizes of 14 nm were found, and no increase of the crystallite size with annealing temperature was observed – up to 500 °C. At about 500 °C the crystallite sizes started to increase, while the microstrain started decreasing (Fig. 7.5), and at about 1000 °C the crystallite size reaches the limit of X-ray sensitivity (several hundreds of nm). Besides these trends, we note that in the thinner (mixed phase) films the crystallites of anatase are larger in the whole temperature range. Microstrain in rutile in these films is approximately constant (about 1 %) up to 800 °C.

The above mentioned picture of thin rutile layer between the substrate and the rest of the anatase film was verified by changing the incidence angle. For sample with thickness 935 nm we observed the dependence of phase composition on depth using incidence angles in range of 0.5–2.0 degrees. It was found that for lower incidence angles only anatase (101) reflection could be observed, while for higher angles rutile (110) reflection appeared (Fig. 7.6). This confirms that there is only anatase

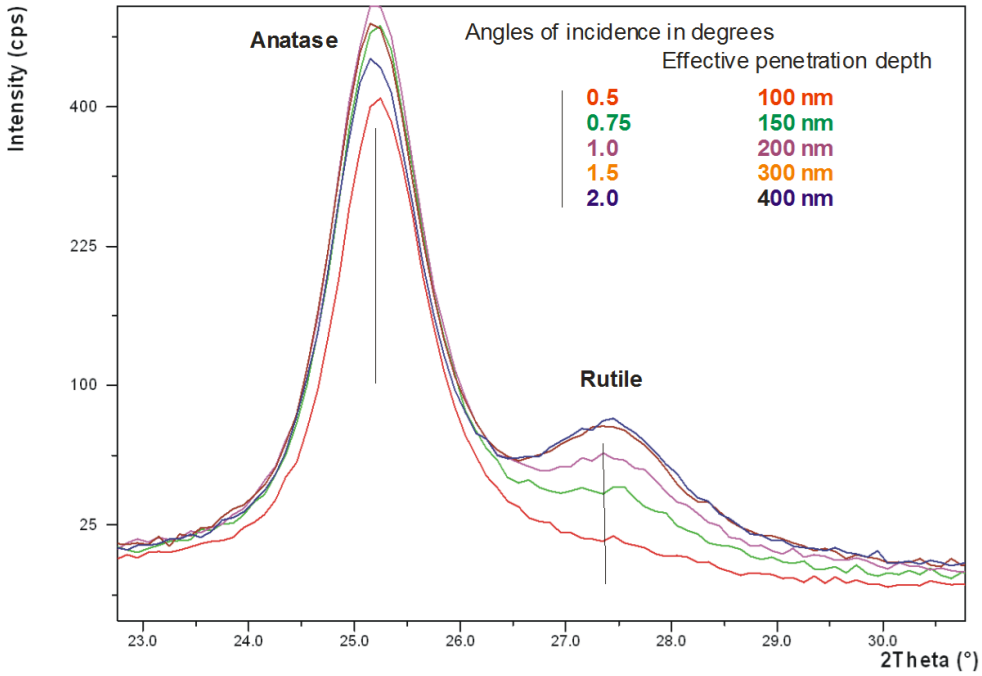

Figure 7.6: Depth profile of the sample 935 nm on silicon substrate. The first peak belongs to anatase (101) reflection, the second one is rutile (110).

sample	thickness (nm)	density (g/cm^3)	roughness (nm)
45-05	100	3.86 ± 0.01	1.78 ± 0.02
45-01	220	3.89 ± 0.01	3.36 ± 0.02
45-03	515	3.65 ± 0.01	5.04 ± 0.02
45-02	935	3.65 ± 0.01	6.07 ± 0.02
45-04	2000	3.51 ± 0.01	6.36 ± 0.02

Table 7.1: The values of the electron density and roughness evaluated from fitting of X-ray reflectivity. The displayed uncertainties are rough estimates based on the final populations.

phase close to surface of the sample and that there is a mixture of rutile and anatase or pure rutile deeper in the film, closer to the substrate.

7.2 Reflectivity

In case of a thin film, the structure of the surface has a significant impact on the properties of the film as a whole. To observe the changes of surface roughness and density with increasing film thickness, we performed X-

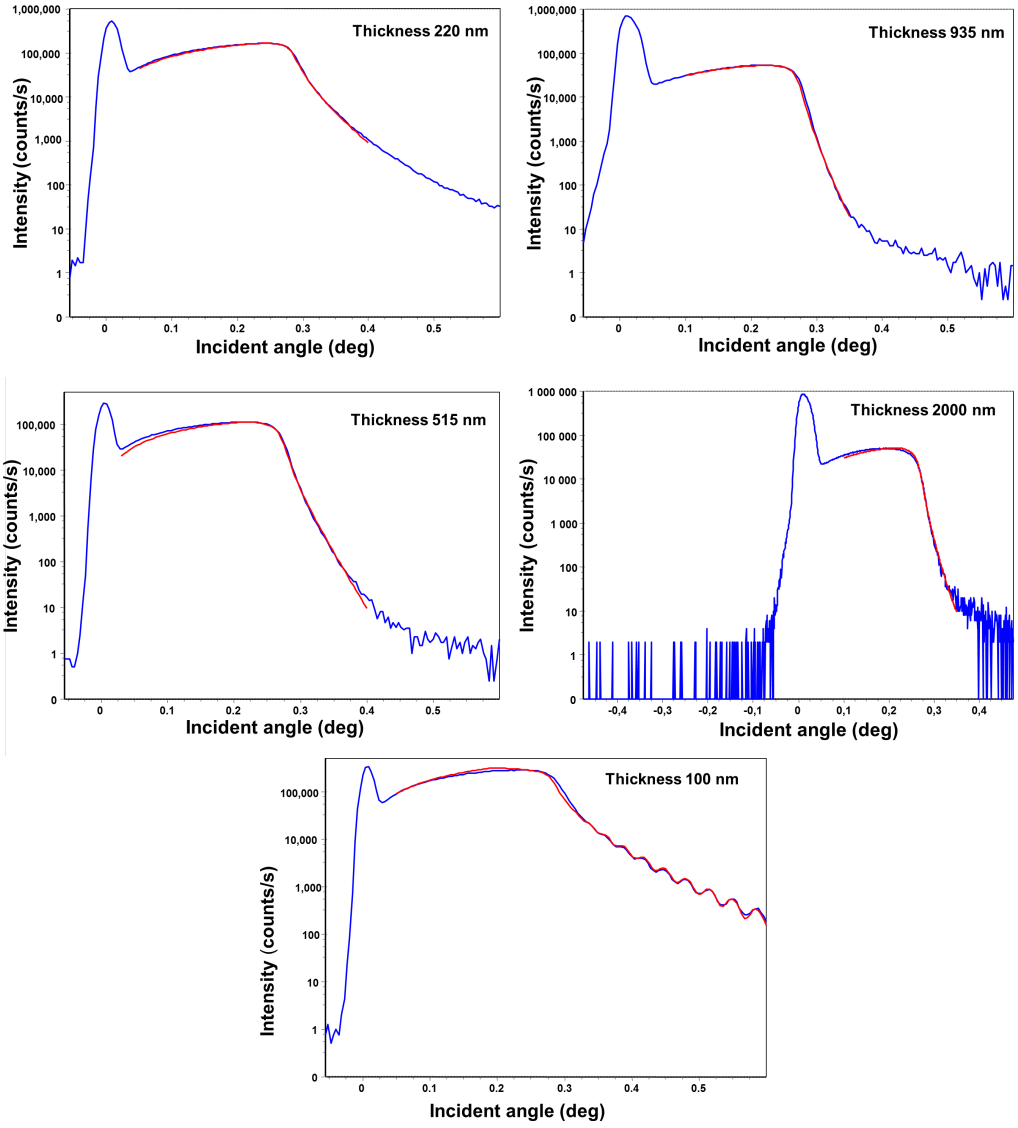

Figure 7.7: The reflectivity curves and their fits for all measured titanium dioxide thin films. Blue curve represents the measured data and red curve is the fit.

ray reflectivity experiments.

Measured X-ray reflectivity curves were fitted with X'Pert Reflectivity program (the measured and fitted reflectivity curves are displayed in Fig. 7.7), which allows to extract three fundamental properties from the experimental data: density, roughness and thickness of the film (see Table 7.1). In general, when the film structure is of high quality and its thickness less then approximately 1 μm, it is possible to observe Kiessig fringes. They are thickness oscillations which result from the interference between the X-rays reflected from the surface of the TiO_2 film and the interface between the TiO_2 film and the Si substrate [72]. In our case only the thinnest sample (100 nm) allowed for reasonable fit of the fringes (value from the fit 108.8 ± 0.5 nm, Fig. 7.7 bottom), for thicker samples the thickness parameter was not fitted. The disappearing of thickness oscillations in the diffraction patterns of thicker samples is due to reaching the limits of X-ray reflectivity method.

The roughness and density evaluated from the fits of reflectivity measurements are shown in Table 7.1. The roughness parameter is inversely related to the density since rougher surface will naturally have lower density on average. In our data the surface roughness increased with thickness of the film while the density at surface decreased. This is in agreement with the results of previous section where the thicker samples were found to have larger average size of the crystallites.

7.3 Residual stress

The process of sputtering of the nanocrystalline thin films always, to some extent, induces internal stress into the structure. This residual stress, which can be well studied by X-ray methods, is quite expected for the samples deposited at relatively low temperatures as the migration of atoms is limited.

Samples with two different substrates (silicon and glass) were measured and analyzed; the film thicknesses were: 515, 935, and 2000 nm. Additionally, the sample with thickness 515 nm deposited on a silicon was measured after annealing at 400 °C.

The measurements were carried out by using Eulerian cradle in order to allow the $\sin^2\psi$ method for evaluation of the residual stresses (see Chapter 3 for details of the method), a polycapillary was applied in order to increase the X-ray flux. The analysis was performed using the X'Pert

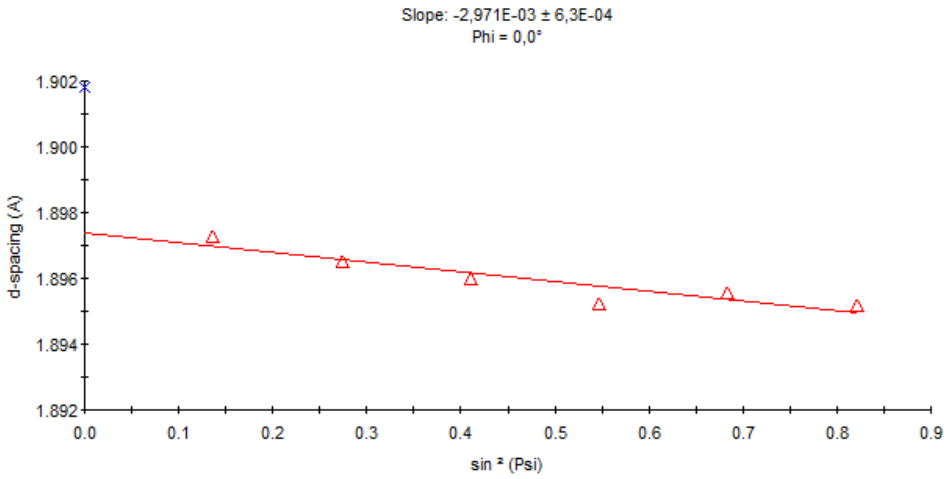

Figure 7.8: Dependence of spacing d on $\sin^2\psi$ for reflection 200 of 2000 nm sample on glass.

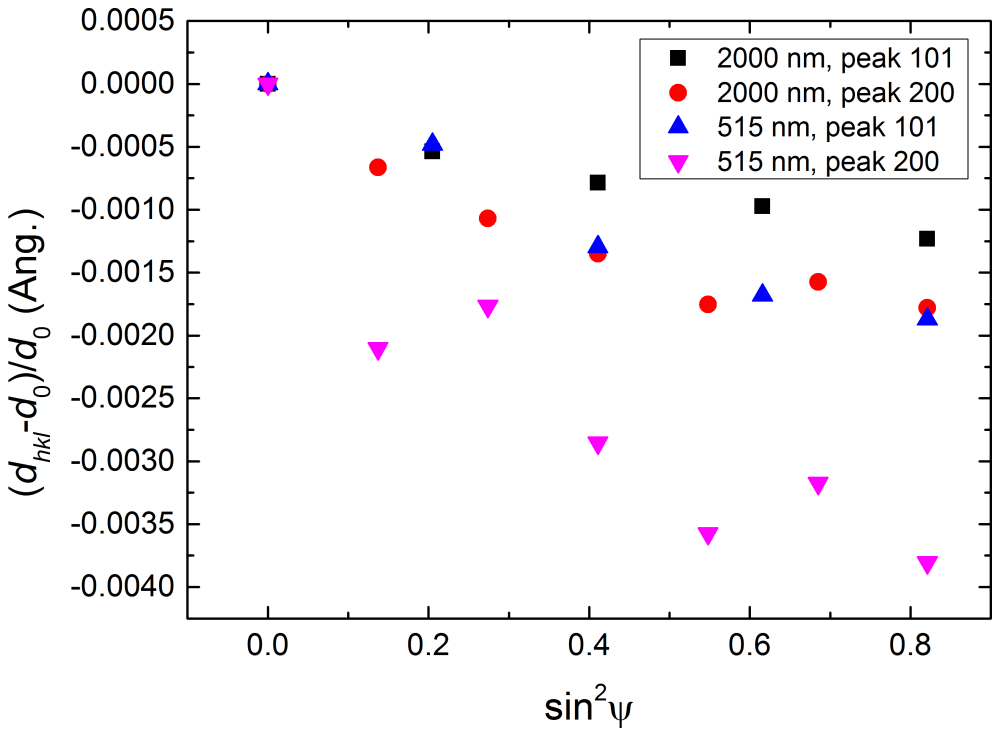

Figure 7.9: Dependence of $\frac{d_{hkl}-d_0}{d_0}$ on $\sin^2\psi$ for different reflections of two samples.

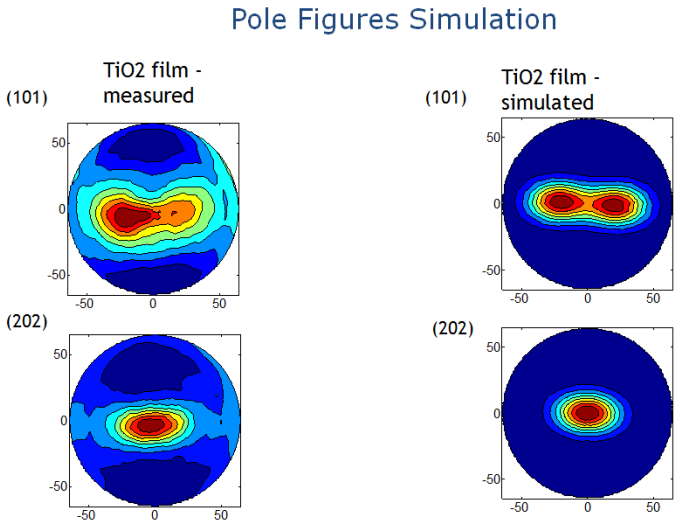

Figure 7.10: Measured and simulated pole figures of (101) and (202) diffractions for the 200 nm film .

stress software for selected diffraction peaks with reasonable intensity: 101, 200 and 105. An example of a $\sin^2 \psi$ dependence for 2000 nm sample on glass is displayed in 7.8.

From the measurements it seemed that residual stress had compressive character (Fig. 7.8). Closer look at dependences of $d_{hkl} - d_0/d_0$ on $\sin^2 \psi$ for different reflections in Fig. 7.9 reveals that the residual stress is quite complicated.

7.4 Texture

Due to the fact that all the samples were too thin for proper texture measurements, only sample with the thickness 2000 nm was measured. The pole figure was measured for two diffractions (101) and (202). The texture was not fiber. Measured and simulated pole figures for 2000 nm film can be seen in Figure 7.10. The Gauss model was included into M'Struct software used for simulated pole figures.

7.5 Hydrophilicity

The results from X-ray measurements were complemented with results of hydrophilicity measurements (again performed at University of West

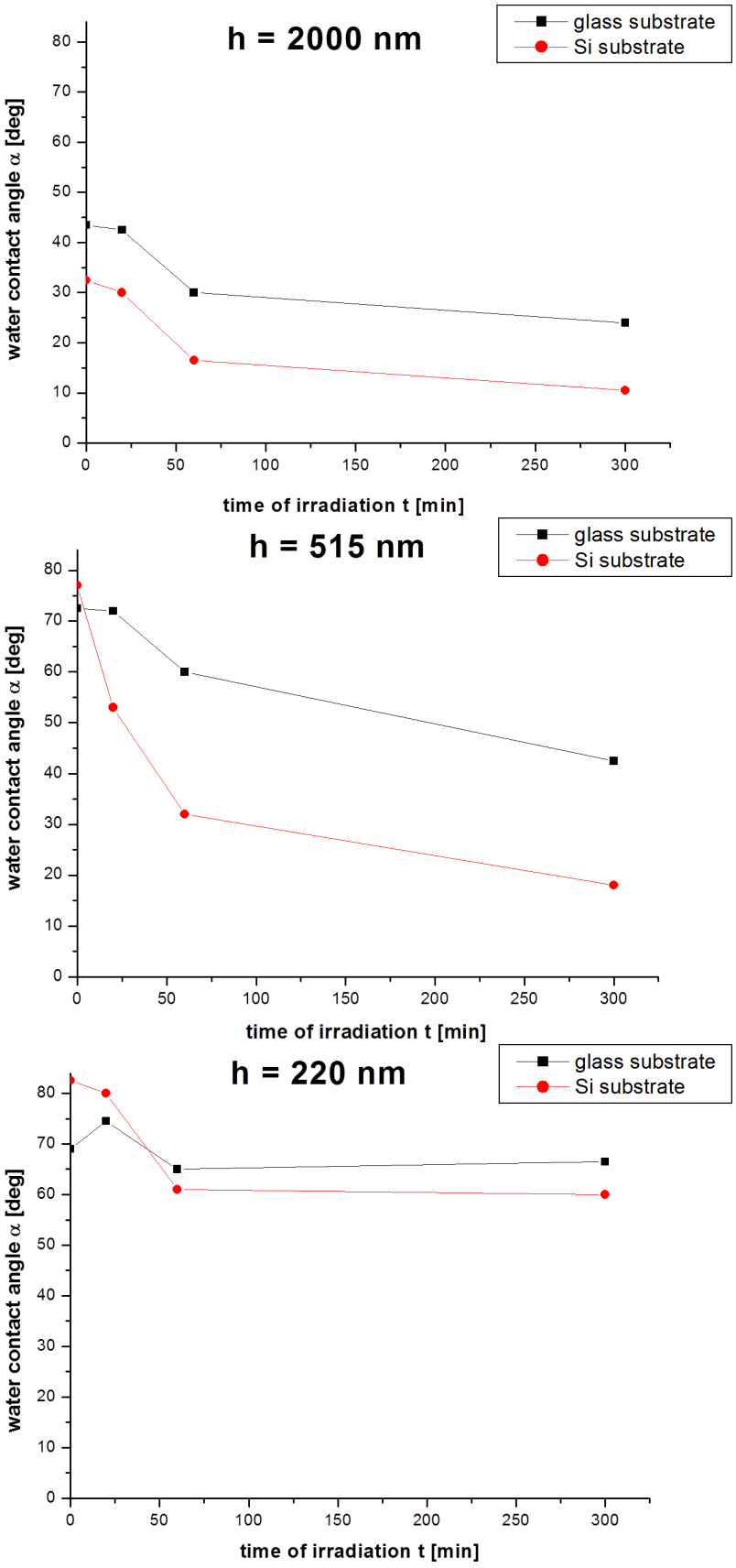

Figure 7.11: Water contact angle measurement of 2000 nm, 515 nm and 220 nm thin film (from top to bottom).

Bohemia). Only the thickest sample (2000 nm) showed good hydrophilicity, the other measured samples 515 and 220 nm thin showed poorer hydrophilicity. The results of hydrophilicity measurements are shown in Fig. 7.11.

7.6 Summary

Samples prepared as nanocrystalline were studied with methods of X-ray diffraction. Unlike the series of samples prepared as amorphous [71], this set of samples had smaller crystallites which were stable up to high temperatures. In dependence on sample thicknesses the samples in series displayed considerable differences: the thinner films consisted of dominating rutile phase with a small indication of anatase, while the films thicker than 500 nm were composed mainly from the anatase phase. Annealing above 700 °C, when the transformation of anatase phase into rutile starts, caused reduction of the anatase phase in rutile-rich thin films until the anatase completely disappeared at about 1000 °C. For the thicker, anatase-rich films the rutile peaks clearly appeared after 700 °C and gradually replaced the anatase phase until 1000 °C.

The annealing process influenced also the crystallite size, which at about 500 °C started to grow from 5–7 nm (for as-deposited samples) to reach the limit of X-ray sensitivity (several hundreds of nm) at 1000 °C. In the thinner (mixed phase) films the crystallites of anatase were larger in the whole temperature range.

The samples were not homogeneous across their depth, as noted from changing the incidence angle: there is only anatase phase close to surface of the sample and while mixture of rutile and anatase or pure rutile deeper in the film, closer to the substrate.

The roughness and density was evaluated from the fits of reflectivity measurements - the surface roughness increased with thickness of the film while the density at surface decreased, which is in accord with the thicker samples having larger average size of the crystallites.

Residual stress (and also texture) for these samples was quite complicated and possible to estimate only approximately. The aim was to prepare samples with good hydrophilic properties. But only the thickest sample showed good hydrophilic properties.

Chapter 8

In situ study of temperature stability

Titanium dioxide thin films display a complex behaviour during the growing and annealing, as shown in the previous chapter for samples prepared as nanocrystalline. In order to understand better the processes during the crystallization, such as the connection between the crystal structure, sample thickness, annealing temperature and annealing time, we focused on observing the structural transformation from amorphous to crystalline state using *in situ* high-temperature X-ray experiments.

In the following text, first, a short description of sample preparation and basic characterization by X-ray phase analysis is given. The study of crystallization process during the annealing is presented, when the selected diffraction peaks are observed in detail – especially to evaluate the X-ray line broadening. After the annealing, the film surfaces are analyzed from X-ray reflectivity measurements and the development of residual stress is evaluated.

8.1 Amorphous samples

TiO_2 thin film samples were again prepared by magnetron sputtering by Dr. Šicha at the West Bohemian University in Pilsen [73]. The films were deposited as amorphous on unheated silicon (100) substrates. Two identical sets of samples were studied, each with thicknesses: 48 nm, 100 nm, 130 nm, 180 nm, 300 nm, 440 nm, 630 nm, and 800 nm. The first

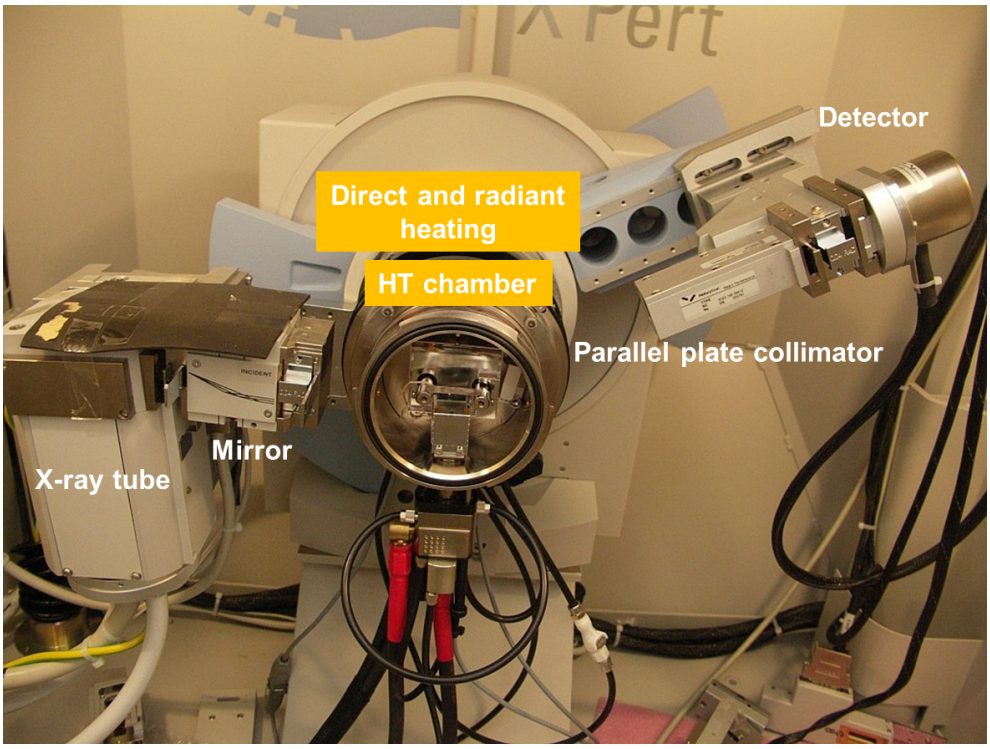

Figure 8.1: MRI diffractometer with high temperature chamber.

set was used for preliminary measurements, in order to find out the exact temperature of crystallization for a given sample thickness. In the second set time-evolution of diffraction patterns was *in situ* in high-temperature chamber.

8.2 High temperature XRD measurements

The crystallization process was observed by using *in situ* high-temperature measurements, performed in MRI high-temperature (HT) chamber with both direct and radiant heating. In case of the direct heating the sample was fixed to a platinum plate that was directly heated. Such procedure possesses a risk of an unequal distribution of heat and consequent temperature gradients. In order to avoid such complications the U-shaped Pt radiant heater was also used, which involves surrounding the holder with the measured sample by a heated cell radiating the heat more evenly. The scheme of the high-temperature chamber is displayed in Fig. 8.1.

The films deposited on Si substrate were fixed on top of a PtRh strip heater with a silver paste, which is an approach applicable for tempera-

tures below 700 °C. The temperature was measured by a thermocouple fixed to the bottom of the strip. Calibration of actual temperature on the film surface was realized by using a thin Ag and Al layer on the same substrate. Both materials, Al in particular, have rather high thermal expansion coefficients, and consequently, the peak positions are very sensitive to the changes of temperature. Despite the films being heated primarily by the radiant heater, the temperatures on the top of the films were about 8–10 °C higher than the values measured by the thermocouple.

The HT chamber was placed on the vertical Panalytical X'Pert Pro theta-theta goniometer. The parallel beam diffraction geometry consisted of parabolic Goebel mirror with slit and mask in the primary beam, and proportional point gas detector in the diffracted beam. The angle of incidence of 1° was used for all the 2θ scans of the *in situ* HT measurements.

Each time, after setting the temperature, alignment of the specimen was checked by measurement of primary beam and, if necessary, the specimen position was corrected in order to keep the irradiated area in the centre of the specimen. The alignment took always less then 3 minutes, which was important for isochronal annealing experiments.

The room temperature measurements were performed on Panalytical X'Pert MRD horizontal diffractometer in a similar parallel beam setup, by the 2θ scans with the angle of incidence fixed at 0.5°.

8.3 Isochronal annealing

The *in situ* isochronal annealing experiments started at 180 °C with a step of 20 °C up to 500 °C. The (101) anatase peak was measured and two subsequent scans (12 minutes each) were taken at each fixed temperature. The total time of the specimen staying at the temperature was 30 minutes.

As an example, temperature dependence for samples 800 nm and 180 nm is displayed in Fig. 8.2. It can clearly be seen, that for thinner films the temperature of crystallization was higher, however, there is an ambiguity in the definition of the crystallization temperature since it depends also on time – given enough time, the sample would fully crystallize even at lower temperature, eventually. Therefore, we define a "temperature of fast crystallization" where the "fast" means, in this case, the appearance of the diffraction peak within a few minutes. Such temperature was found to be 220 °C for the films thicker than 300 nm. For thiner films the temperature of "fast" crystallization increased to 240 °C for 180 nm, 260 °C

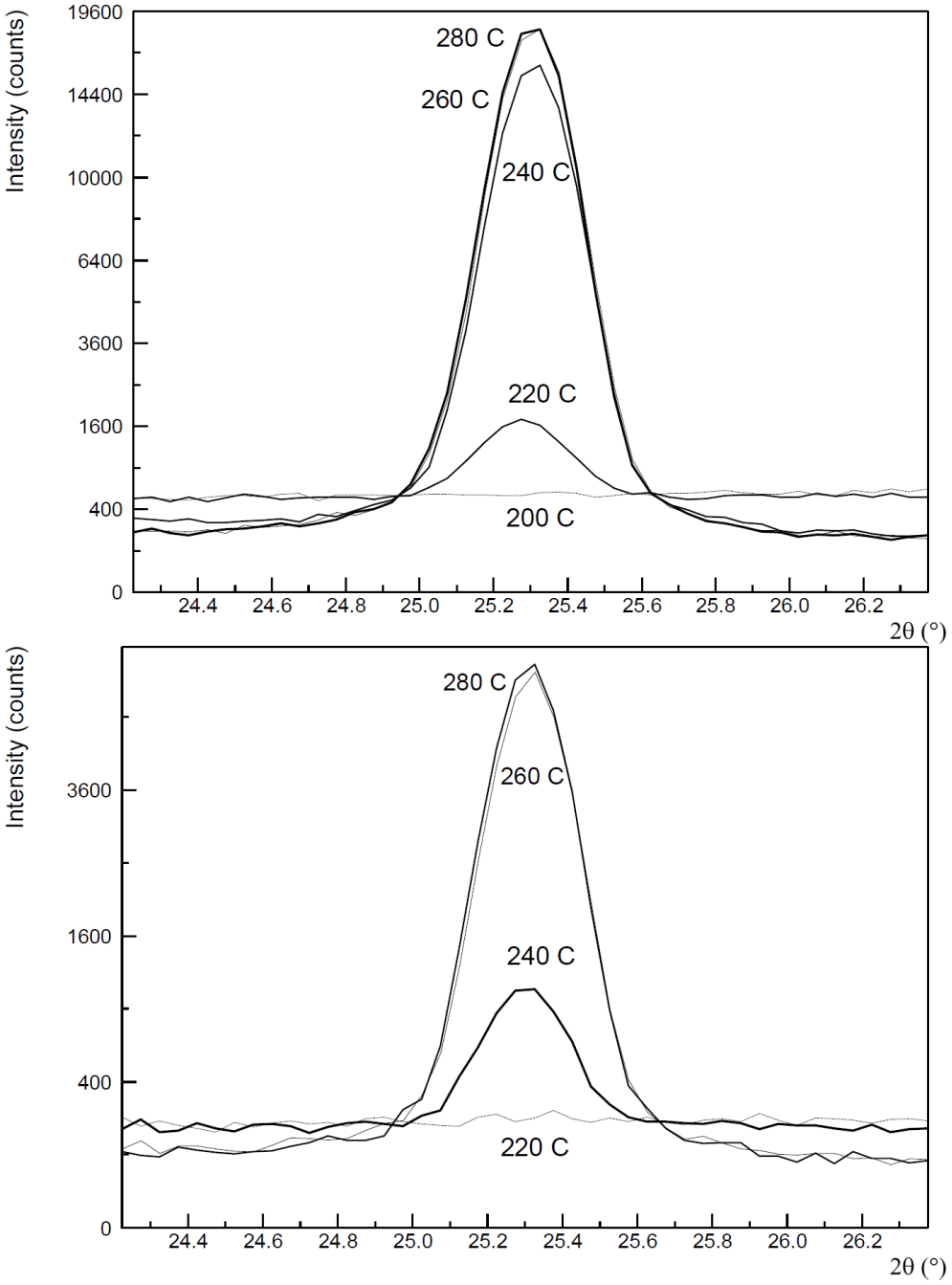

Figure 8.2: XRD line profiles of 101 anatase peak for film with thickness 800 nm (top) and 180 nm (bottom) for different temperatures.

for 100 nm and 280 °C for 48 nm, respectively.

The line widths of all the peaks were relatively narrow immediately after the appearance of the peak, which can be interpreted in the way that crystallites with sizes larger than about 100 nm were formed rapidly. This is very different from the behavior of the as-deposited nanocrystalline films of both rutile and anatase (see previous chapter 7), for which the crystallite size remained small, less than 10 nm, below 400 °C and increased significantly up to 100 nm only at temperatures about 800 °C [74].

8.4 Isothermal annealing

For detailed studies of the crystallization in dependence on time, we used temperatures lower than those of the so-called fast crystallization, for which the temperature was determined in the previous experiments. In such case the crystallization still proceeds, yet at much slower pace, therefore, it does not require synchrotron radiation and can be well studied even in laboratory conditions.

The annealing temperature was chosen as 180 °C for all samples – with exception of the thinnest films (thickness of 48 nm and 130 nm) where the full crystallization process would last too long, therefore, the temperature for these two samples was raised to 215 °C, in order to speed up the process. The following anatase peaks were observed (101), (103), (004), (112), for some samples also (200) and (116), however, the intensity of (101), (004) and (200) only was strong enough to obtain statistically good data. As an example, time evolution of (101) peak for films with several different thicknesses is shown in Figure 8.3. The dependences of the peak intensity on annealing time were normalized with respect to the maximum value reached for each sample after the full crystallization. The shape of the obtained curves resembles well known Avrami dependences of solid-solid transformations [75, 76]. The time dependence of crystalline (or recrystallized) volume fraction $x(t)$ can be described by Johnson-Mehl-Avrami-Kolmogorov (JMAK) equation [77, 78], which in usual form reads:

$$x(t) = 1 - \exp(-kt^n), \tag{8.1}$$

where k is the rate of the process and n is the transformation index related to the dimensionality of the growth and to the kinetic order of nucleation. For a three dimensional growth, combined with the first order nucleation (i.e., a constant nucleation rate), n is equal to 4.

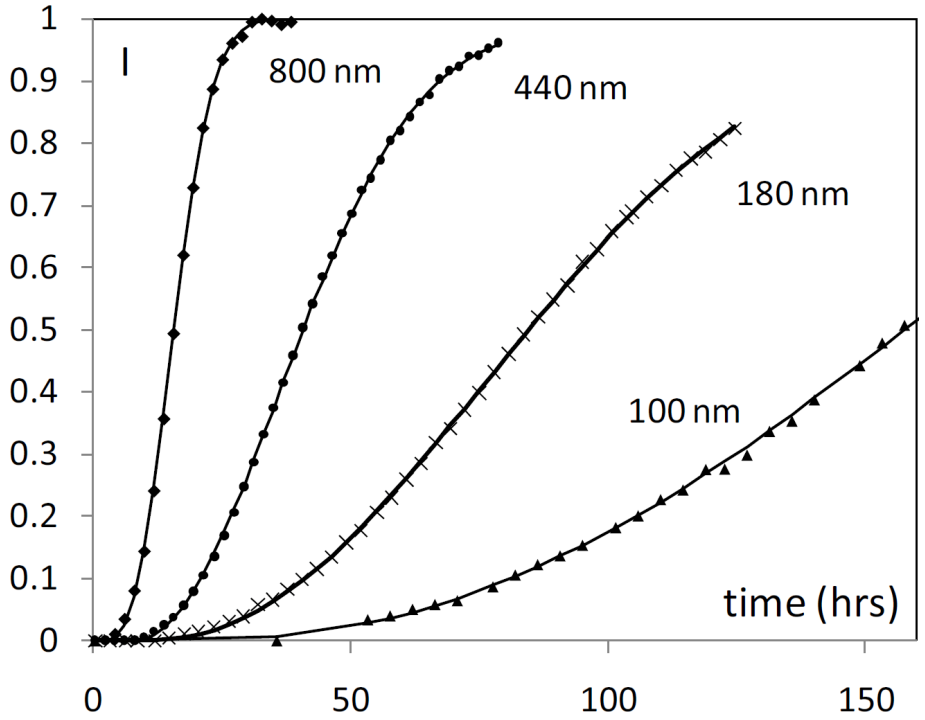

Figure 8.3: Integrated intensities of anatase diffraction peak 101 normalized to the value reached after crystallization are displayed in dependence on annealing time for films with several different thickness. The experimental data were fitted by Avrami equations.

In our case, the exact moment when the crystallization process starts may not necessarily coincide with the beginning of the measurement. Therefore, it was necessary to modify the equation 8.1 by additional parameter corresponding to initial time of crystallization t_0. This initial time of crystallization t_0 significantly improved the Avrami fits. We evaluate it as a time when any significant diffracted intensity appears above the background in the position of the expected diffracted peak. The modified equation

$$I = 1 - \exp[-k(t - t_0)^n], \tag{8.2}$$

was then applied to fit the integrated (normalized) intensities I of the diffraction peaks – the crystallization onset t_0 was fitted together with the rate k and exponent n.

The fits performed on the thicker samples gave a very good agreement ($R \sim 0.999$), while for samples thinner than about 200 nm the measured intensities during the early stage of crystallization were found to be slightly above the expected values ($R \sim 0.994$). The fit was not very appropriate

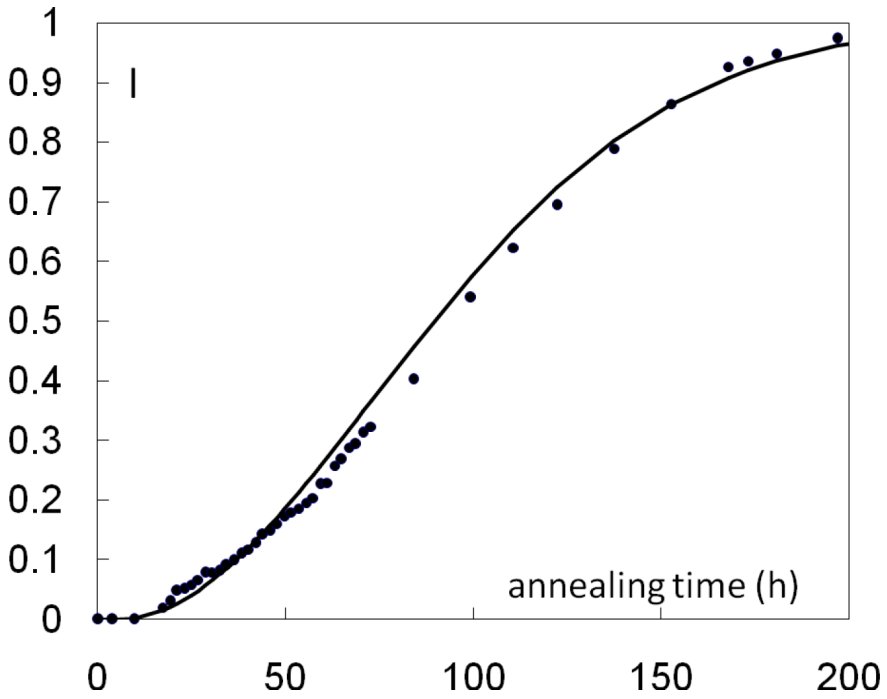

Figure 8.4: Dependence of the integrated intensities of anatase diffraction peak 101 normalized to the value reached after crystallization on annealing time for the thinnest film (48 nm). The symbols represent experimental values, the line is fitted Avrami equation.

for the thinnest film (48 nm) as it can be see in Figure 8.4. Nevertheless, the results for this sample still go down well with the tendency of the whole series: the rate of the crystallization process strongly increases with increasing film thickness, as can be clearly seen in the comparison of fitted curves in (Fig. 8.5, note the higher temperature for the two thinnest samples).

The onset of crystallization t_0 decreases with increasing thickness of the film, and thus follows the behaviour of crystallization rate k: the new phase is observable approximately at the same part of the overall process for all samples. The exponent n changes only slightly with the film thickness, as can be seen in Fig. 8.6; again note that some films were annealed at higher temperature (215 °C).

Although the physical interpretation of the Avrami constants k and n is usually not unambiguous, we can attempt to describe the most probable mechanism of the crystallization process. Since the final crystallite sizes were very large (~ 100 nm as noted above), we can assume that the nucleation rate was very low (or even zero and the growth occurred

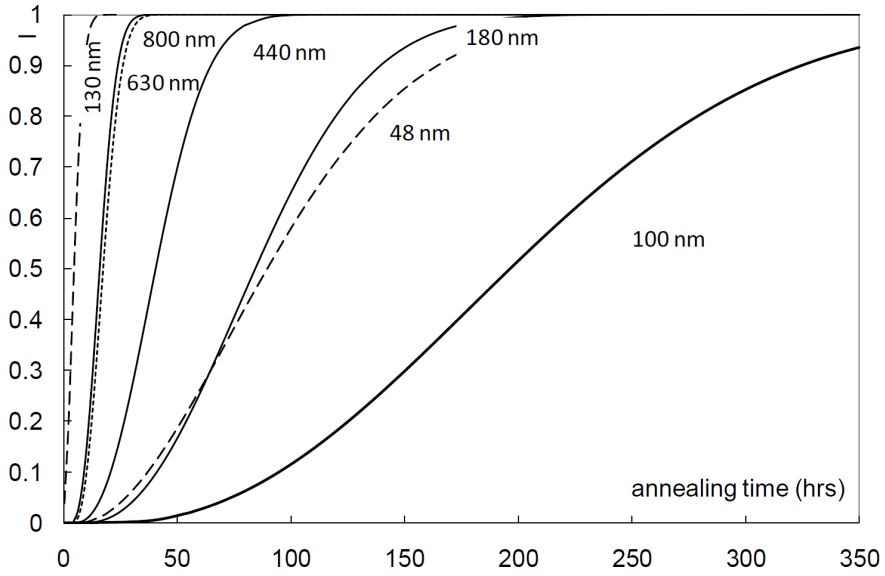

Figure 8.5: Full set of dependences of the integrated intensities of anatase diffraction peak 101 calculated from the fitted Avrami equations on the annealing time. Solid lines and dashed line (short lines, for 630 nm) correspond to the films annealed at 180 °C, dashed lines correspond to the films anealed at 220 °C.

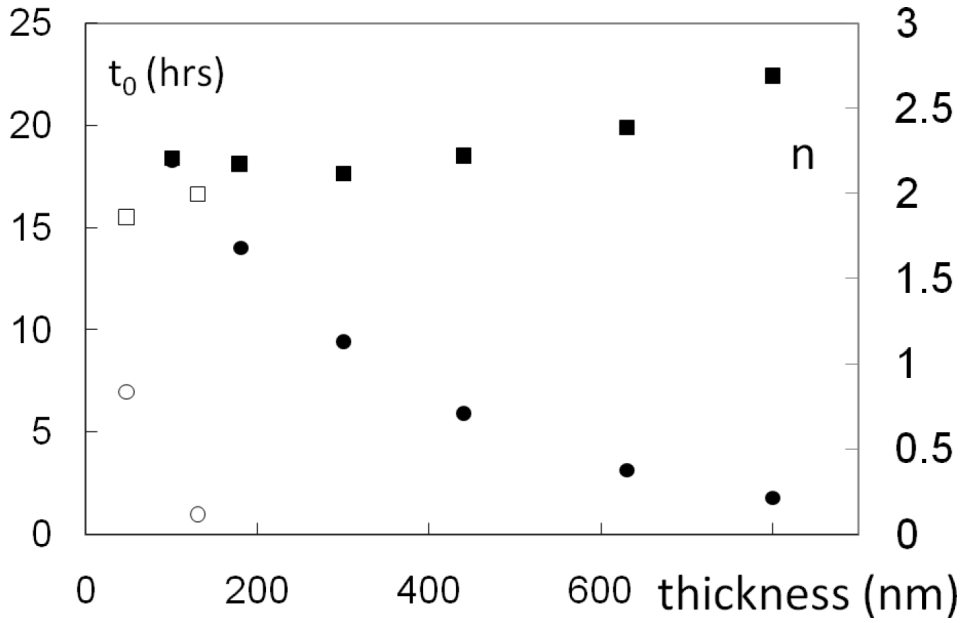

Figure 8.6: Dependence of crystallization onset t_0 (●) and exponent of the Avrami equation n (■) on the film thickness. Filled symbols correspond to the film annealed at 180 °C and open symbols to the films annealed at 220 °C.

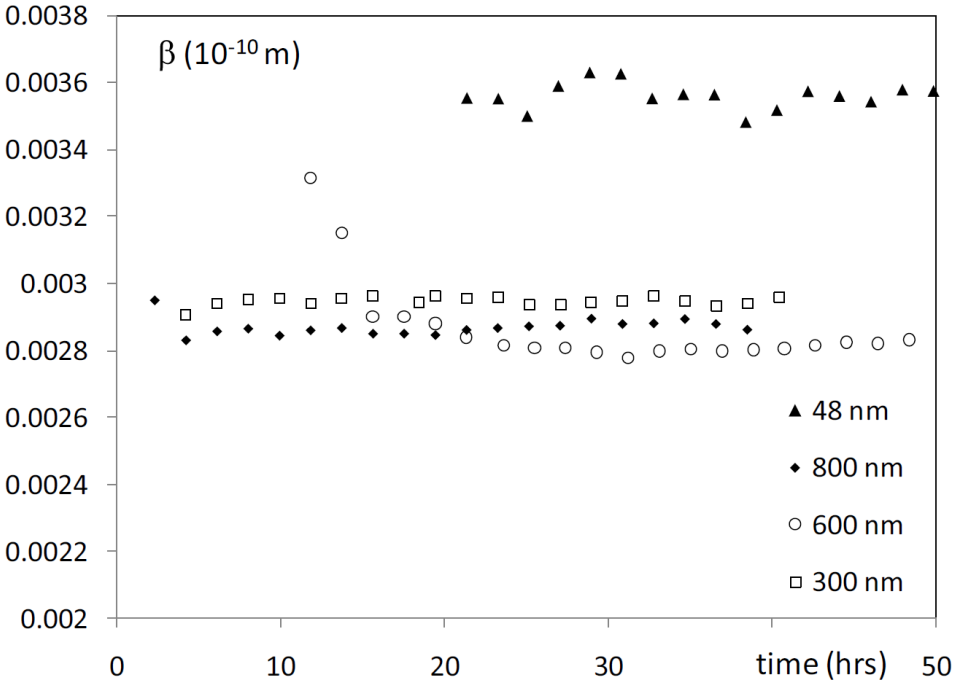

Figure 8.7: Measured integral breadth of 101 anatase peak (in reciprocal space units, 1/d) vs. annealing time for different film thicknesses. The level of instrumental broadening in the parallel beam geometry was at about 0.0027 10^{-10} m.

only from the initial nucleation sites) – in such case the n should correspond to the dimensionality of the growth. The evaluated value of the exponent n lies in the range 2.2-2.7, which can be attributed to a three-dimensional growth that is partially constrained in one dimension. Such an interpretation is in accord with the fact that n slightly increases with increasing thickness of the films. Furthermore, the initial nucleation sites are probably relatively randomly distributed in the film, since a nucleation occurring only at the surfaces of the film would restrict the growth to one dimension and cause a marked decrease of n.

8.5 Line broadening

Experimental values of integral breadths vs. annealing times for several films are shown in Fig. 8.7. For this series of samples the line broadening was quite small already from the very beginning of the crystallization and did not change significantly during the annealing. This indicates fast growth of relatively large crystallites already from the beginning of

sample	annealing	density (g/cm^3)	thickness (nm)	roughness (nm)
48	200 °C	3.88 ± 0.03	46.2 ± 0.2	1.5 ± 0.1
130	200 °C	3.92 ± 0.02	133.1 ± 0.5	1.45 ± 0.05
180	as prepared	3.65 ± 0.07	193 ± 30	1.59 ± 0.05
180	200 °C	3.79 ± 0.05	193 ± 15	1.93 ± 0.05
300_A	as prepared	3.66 ± 0.01	297 ± 100	2.52 ± 0.01
300_A	230 °C	3.70 ± 0.01	not fitted	2.68 ± 0.01
300_B	200 °C	3.80 ± 0.01	not fitted	2.14 ± 0.01
300_C	230 °C	3.80 ± 0.01	not fitted	2.60 ± 0.01
440	200 °C	3.72 ± 0.01	not fitted	2.97 ± 0.01
630	200 °C	3.89 ± 0.05	not fitted	3.03 ± 0.01
800	as prepared	3.72 ± 0.02	not fitted	3.70 ± 0.01
800	200 °C	3.44 ± 0.02	not fitted	3.38 ± 0.05

Table 8.1: The values of the density, film thickness (only for the thinnest films) and roughness evaluated from fitting. The displayed uncertainties are rough estimates based on the final populations.

the crystallization. Even if we ascribed the whole observed broadening to the size of the crystallites only (thus disregarding any instrumental contributions or microstrain, which is not very realistic), the estimated crystallite sizes would be at least about 100 nm, except for the thinnest film.

The situation is, therefore, completely different from the films deposited as nanocrystalline discussed in previous Chapter (7), where the crystallite sizes were 5–10 nm and remained nanocrystalline up to relatively high temperatures (600 °C) [79]. When the process starts from amorphous state, the nucleation rate is too low and the crystallites grow relatively unconstrained. This suggests that it is not possible to prepare nanocrystalline TiO_2 thin films from magnetron-sputtered amorphous films by annealing only, which is a common approach for preparation of nanocrystalline powders, i.e., annealing for specific time at specific temperature for the desired size of nanocrystals.

8.6 X-ray reflectivity

To extract the information about the roughness, density and thickness of the film, the X-ray reflectivity measurements were performed in the same set-up as for the series of films prepared as nanocrystalline (see Chapter

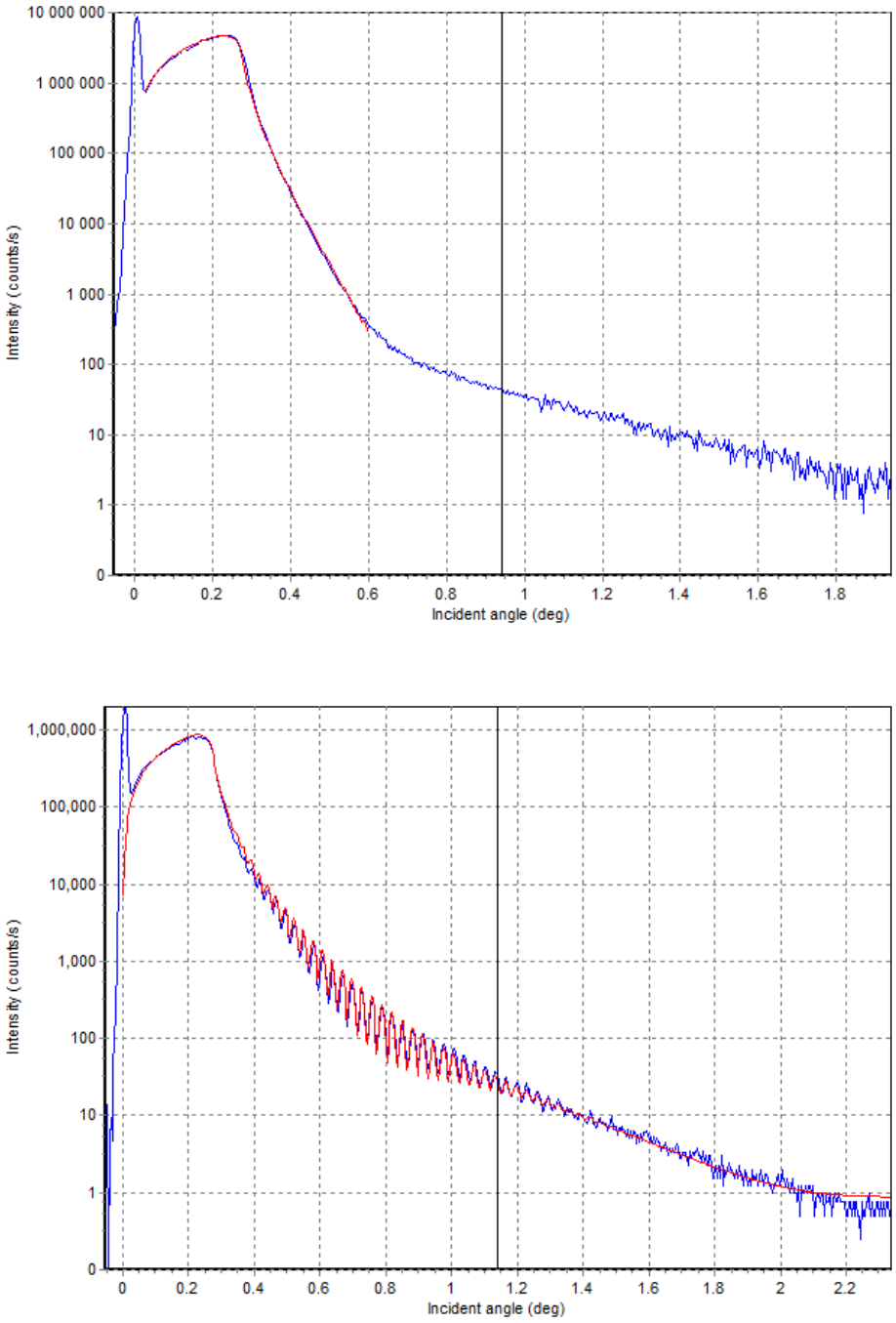

Figure 8.8: The reflectivity curves (blue) with corresponding fits (red) for the samples with thickness 300 nm (top) and 130 nm (bottom), annealed at 200 °C.

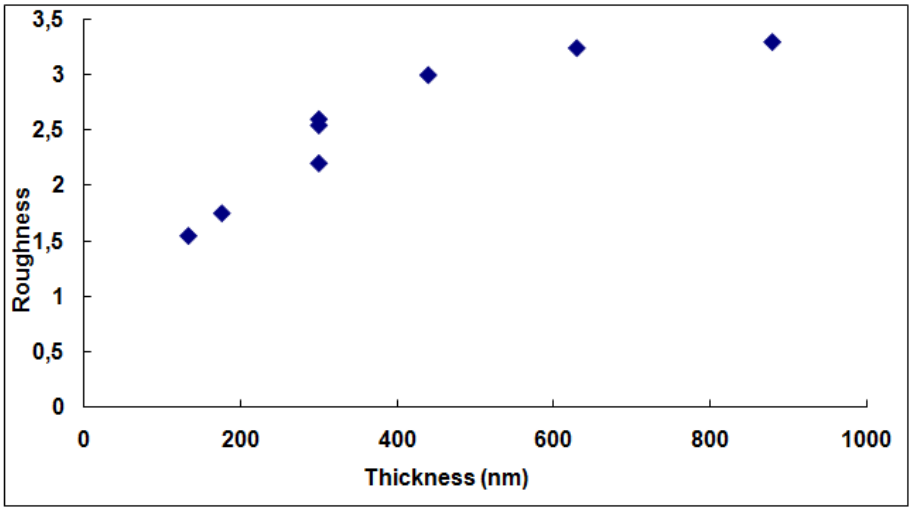

Figure 8.9: Dependence of the surface roughness on the film thickness.

7). The reflectivity curves were analyzed with software X'Pert Reflectivity by Panalytical, the genetic algorithm was used for all the samples. The quality of the fits was improved by introducing a very thin (units of nm) SiO_2 layer between the substrate and the TiO_2 film in the fitting model. Moreover, reflectivity curves for thicker films (630 and 800 nm) had to be fitted with a two-layer model using an additional TiO_2 layer since no good agreement could be achieved with a single-layer model. Such an additional thin film can represent a highly porous layer on the surface.

The thickness oscillations (Kiessig fringes) were observed only for the three thinnest films: 48, 130 and 180 nm. In cases where the thickness oscillations were observed, also thickness of the film was fitted, otherwise only the density and the roughness were evaluated. As an example, fits of the film with thickness 300 nm and 130 nm, both annealed at 200 °C, are shown in Fig. 8.8.

An increase of the surface roughness with increasing film thickness was observed (Fig. 8.9), which is in agreement with results for nanocrystalline films in the previous chapter. The values of the density, film thickness and roughness evaluated from the fitting are shown in Table 8.1. The X-ray reflectivity measurements confirm the thickness of the films for the thinnest films, where it was possible to observe the thickness oscillations.

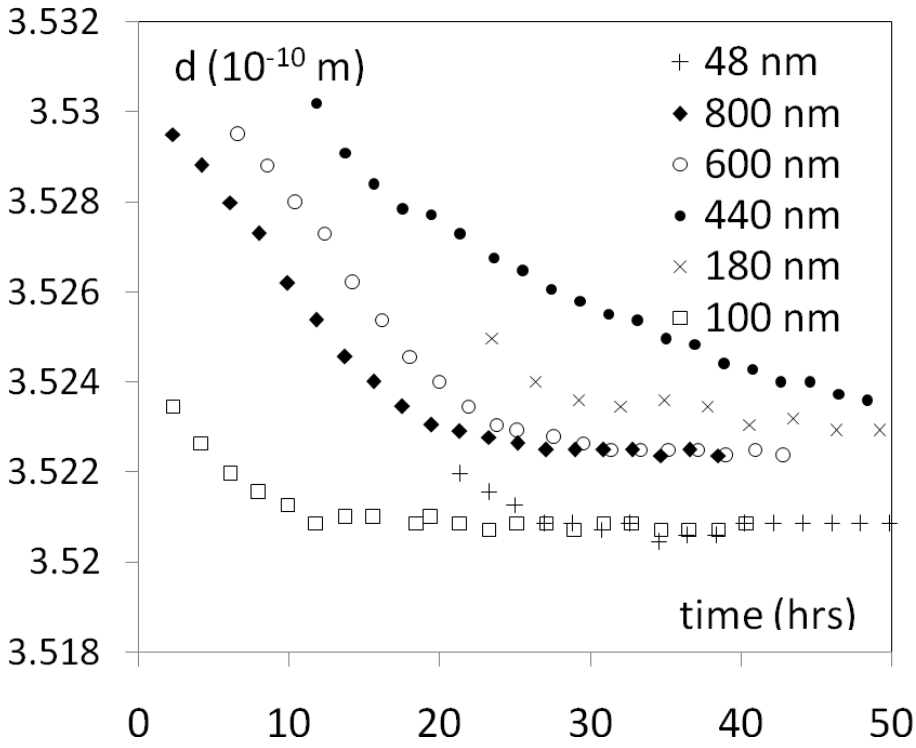

Figure 8.10: Changes of lattice spacing d of anatase lattice plane (101) with annealing time in dependence on film thickness. Annealing temperatures were 180 °C for films with thickness 800, 600, 440, and 180 nm and 225 °C for 130 and 48 nm.

8.7 Peak shifts - stress development

During the *in situ* high-temperature XRD measurements, significant shifts of diffraction peaks with time were observed and tensile residual stresses were confirmed for different diffraction peaks on post-annealed samples measured at room temperature. In the course of the annealing the interplanar spacing of the (101) plane is decreasing with time to some saturated value (Fig. 8.10), which corresponds to evolution of stress with the annealing and it is well visible, in particular, for the thicker films (800 nm, 630 nm), where the stress changes practically during the whole crystallization process. It seems, on the contrary, that for thinner films the stress was formed quite rapidly and only the final stage of its evolution could be observed.

Applying the $\sin^2\psi$ method (see Chapter 3) on the films at room temperature after the annealing revealed that the stresses significantly decreased with increasing film thickness. The results agree well with the

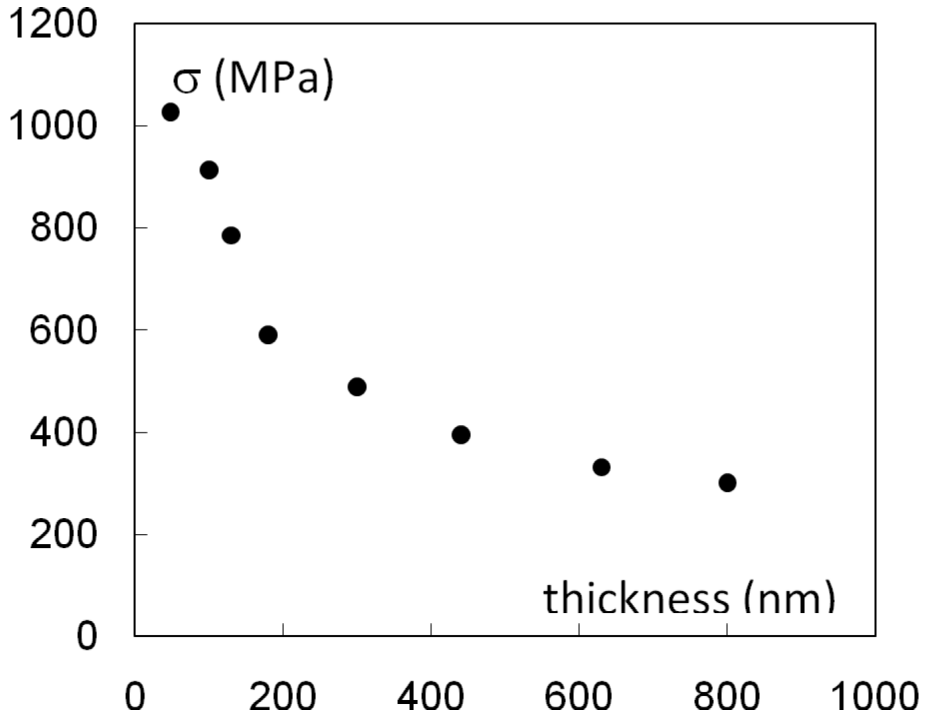

Figure 8.11: Dependence of tensile stress determined by the $sin^2\psi$ method on the film thickness.

values obtained on these samples by total pattern fitting (using M'Struct program) of 2θ scans [74, 45], see Fig. 8.11.

8.8 Residual stress and elastic anisotropy

TiO_2 thin films prepared on various substrates (silicon, glass, saphire) exhibit different residual stress [80, 81]. This is partly caused by the deposition process itself, but often it is due to different thermal expansion coefficients of the coating and the substrate or by their lattice parameter mismatch. For anatase thin films, it was also shown that introduction of large tensile stress in the film can enhance its photo-induced hydrophilic behaviour significantly [80, 81].

XRD does not measure the stress directly, but rather the strain in the material which then must be converted into the stress via material elastic constants and by considering an appropriate grain interaction model and strain-stress relation in the sample [44, 82]. Proper accounting for crystal elastic anisotropy is often the critical aspect of the method, and unfortunately, for the anatase the single-crystal elastic constants are un-

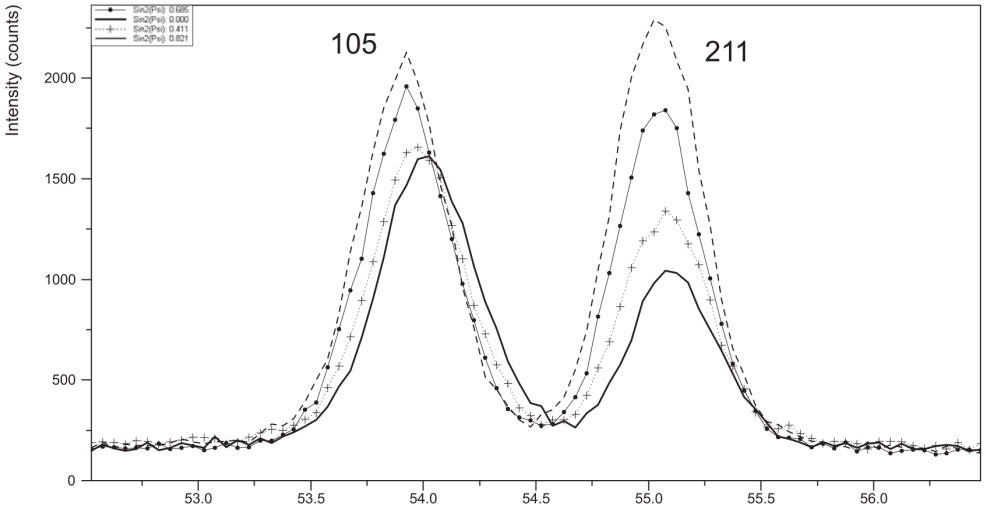

Figure 8.12: Two diffraction profiles (diffracted intensity vs. 2 theta), 105 and 211, are shown for different diffracting plane inclinations ψ with respect to the film surface ($\psi = 0°$ – thick line, $\psi = 40°$ – crosses, $\psi = 56°$ – dots, and $\psi = 65°$ – thin dashed line). Relative peak shifts for $\psi = 65°$ were $-0.116°$ and $-0.071°$ for 105 and 211 reflections, respectively.

known. Lack of this information can discourage the XRD stress analysis of anatase films or can lead to an incorrect results. In order to minimize such errors, we utilized results of *ab initio* theoretical studies that revealed a single-crystal stiffness tensor C_{ij} for anatase [83, 84, 85].

To analyze our series of TiO_2 thin films the XRD residual stress measurements were performed on a PANalytical X'Pert MRD diffractometer with a point focus Cu X-ray tube and polycapillary optics passing X-ray beam with vertical and horizontal divergence of 0.3 degree. The sample was mounted on an Eulerian cradle, and a point detector with graphite monochromator and parallel plate collimator with acceptance of 0.27 deg in the diffracted beam were used.

The residual-stress measurements were done by symmetric $2\theta - \theta$ scans for different inclination angles ψ of diffracting lattice planes with respect to the sample surface. Since the high-angle anatase reflections of the studied films were weak and also significantly overlapped, only the following low-angle peaks were measured: (101), (200); (103), (004), and (112) triplet; and two doublets: (105), (211), and (116), (220). For the thinnest films only two or three strongest reflections were analyzed. Further details about the residual stress measurements and $\sin^2\psi$ method are given in Chapter 3.

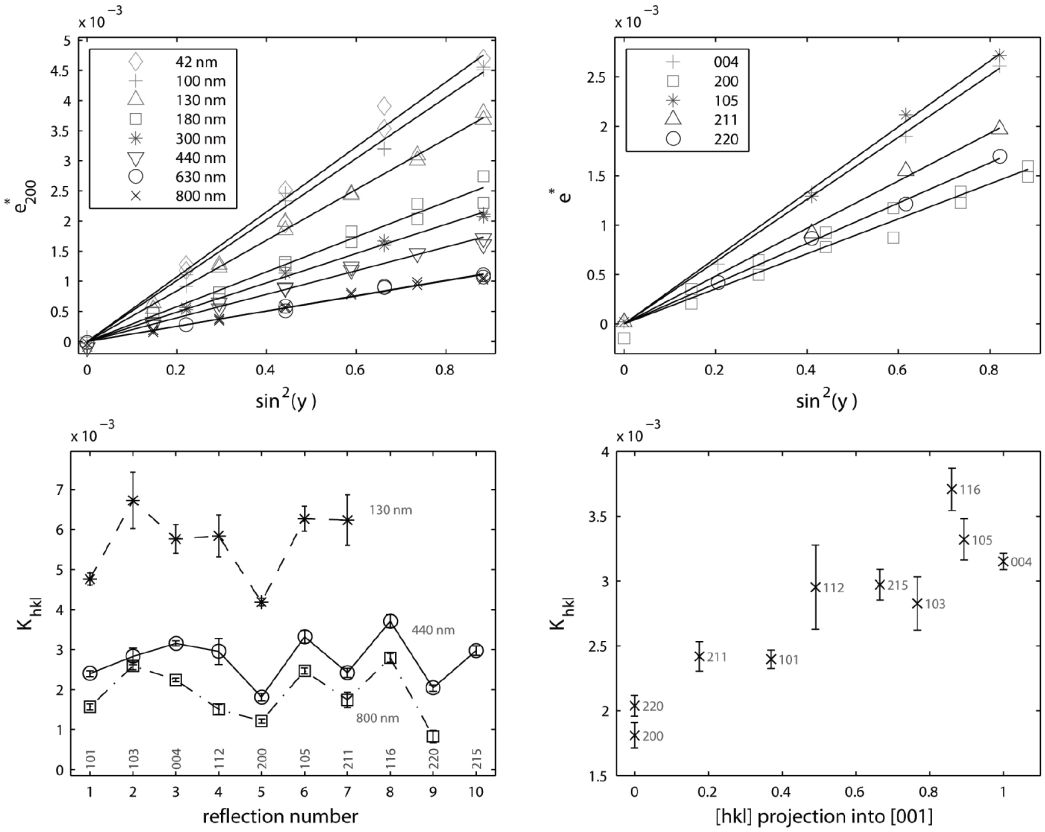

Figure 8.13: Top left panel: strain measured on the (200) plane for thin TiO_2 films with different thicknesses. Top right: strain measured for the 440 nm TiO_2 film on different lattice planes. Bottom left: strain anisotropy, K_{hkl}, ratio of d_{hkl} vs. $\sin^2\psi$ slope to the d_{hkl} vs. $\sin^2\psi$ intercept plotted for different lattice planes and the films with different thicknesses. Bottom right: the slopes K_{hkl} for 440 nm sample and different *hkl* reflections vs. projection of the [*hkl*] diffraction vector direction onto the reciprocal space [001] direction.

Two measured profiles, (105) and (211), for different inclinations of diffraction planes with respect to the surface ψ are shown in (Fig. 8.12). The tensile stress clearly shifts both peaks toward lower values of 2θ with increasing angle of plane inclination ψ. Besides, the (105) peak is significantly larger than the (211) – varying shifts for different peaks are due to strain anisotropy.

In order to evaluate the stresses, the peak positions for all the measured inclination angles ψ, all reflections, and all samples were fitted by the PANalytical X'Pert Stress software and lattice plane distances $d_{hkl}(\psi)$ were obtained. The strain related to the interplanar spacing perpendicular to

the surface can be defined as

$$\epsilon^*_{hkl} = \frac{d_{hkl}(\psi) - d_{hkl}(\psi = 0)}{d_{hkl}(0)}, \tag{8.3}$$

where $d_{hkl}(0)$ is lattice parameter for unstressed material.

As an example, relative differences of $d_{200}(\psi)$ planes spacing with respect to $d_{200}(\psi = 0)$ for all samples, i.e., strain ϵ^*_{hkl}, are plotted in Fig. 8.13, top left panel. Clearly, the strain (given by the slope), and hence also the stress, decreases with the sample thickness.

Linearity of $\epsilon^*_{hkl}(\sin^2 \psi)$ dependences, independent of the sign of ψ, confirms the initial assumption of a simple biaxial stress state in the films. The supplementary measurements verified that the results are independent of the rotation around the sample axis (angle ϕ).

In Fig. 8.13 top right panel, the strain ϵ^* is plotted for a few different *hkl* reflections of the 440 nm sample. It is apparent that the result strongly depends on used *hkl* reflection – the slopes K_{hkl} of the $\epsilon^*_{hkl}(\sin^2 \psi)$ dependences are not equal. From K_{hkl}, and knowing the Young modulus and Poisson ratio, the residual stress can be calculated using the formula

$$\sigma = \frac{K}{d_0 \frac{1+\nu}{E}}. \tag{8.4}$$

The slopes K_{hkl} display a strong systematic anisotropy as evidenced for several measured reflections of three different samples in Fig. 8.13, bottom left panel. Analyzing details of the dependences in top right and bottom left panels in Fig. 8.13 it is also clear that *hkl* reflections with high *l* indexes and small *k* show larger strain, whereas those with small *l* indexes have smaller strain values. This dependence is depicted in Fig. 8.13, bottom right panel, where the slopes for different *hkl* reflections in the 440 nm film are plotted against the projection of the [*hkl*] diffraction vector onto the reciprocal lattice [00*l*] direction. Large induced strains in directions close to the [00*l*] reciprocal lattice direction indicate that the anatase [00*l*] direction is elastically soft while the anatase [*hk*0] directions are hard.

For the relatively strong strain anisotropy, found in the studied samples, the isotropic elasticity model is insufficient and a model predicting strain anisotropy is required. Slopes k_{hkl} and intercepts I_{hkl} of d_{hkl} vs. $\sin^2 \theta$ plots obtained from fitting the data by using the X'Pert Stress (PANalytical B. V.) software together with their fitting errors were considered further as experimentally determined data. They can also be calculated from the model from the values of C_{ij} constants, the stress-free lattice parameters *a*

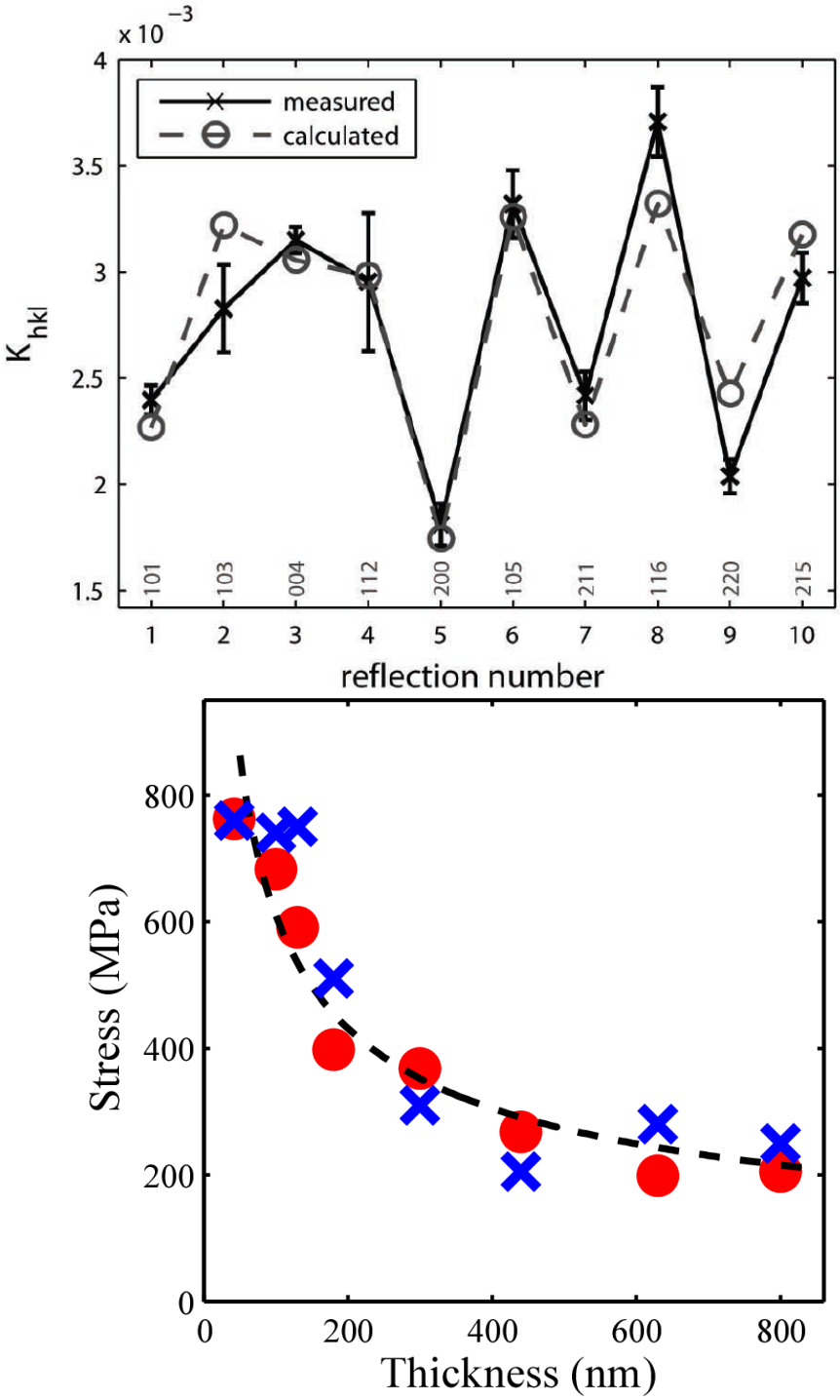

Figure 8.14: Slopes K_{hkl} for 440 nm sample and various *hkl* reflections (top). Dependence of the XRD residual stress on the film thickness (bottom). Values obtained from direct XRD stress measurements (×) are compared with values obtained from the whole pattern fitting (●).

Number	T (nm)	σ (MPa)	w	a (nm)	c (nm)
1	42	690±40	0.3	0.3786	0.9512
2	100	640±20	0.3	0.3786	0.9512
3	130	580±10	0.4±0.1	0.3786±0.0001	0.9512±0.0007
4	180	420±10	0.2±0.1	0.3786±0.0002	0.9512±0.0005
5	300	380±10	0.1±0.2	0.3784±0.0002	0.9503±0.0003
6	440	280±10	0.1±0.1	0.3787±0.0001	0.9506±0.0003
7	630	210±10	0.0±0.1	0.3786±0.0002	0.9506±0.0003
8	800	200±10	0.0±0.2	0.3787±0.0003	0.9505±0.0004

Table 8.2: Evaluated XRD residual stresses. T is the film thickness, σ is the residual stress, w is the weight of the Voigt model, and a and c are the lattice parameters.

and c, the residual stress value σ, and the Reuss-Voigt weighting factor w.

$$\begin{aligned} y_{hkl,k}^{meas} &= k_{hkl} \\ y_{hkl,k}^{calc} &= \frac{1}{2} S_2(hkl) d_{hkl}^0(a,c)\sigma \\ y_{hkl,I}^{meas} &= \text{intercept of } d_{hkl} \textit{ vs. } \sin^2\psi \\ y_{hkl,I}^{calc} &= d_{hkl}^0(a,c) + 2S_1(hkl) d_{hkl}^0(a,c), \end{aligned} \tag{8.5}$$

where d^0 is the stress-free lattice spacing.

For very thin samples (42 to 130 nm), only a few reflections (typically 2 through 4) were available. Therefore, some parameters had to be fixed and stress was determined with a lowered accuracy.

The sum of weighted squares of measured and calculated data differences for all measured *hkl* reflections for the given sample was minimized to find the stress-free lattice parameters, the residual stress in the film, and the Reuss-Voigt weighting factor:

$$\min \sum_{\text{all hkl measured}} \left[\left(\frac{y_{hkl,k}^{meas} - y_{hkl,k}^{calc}}{\sigma_{hkl,k}} \right)^2 + \left(\frac{y_{hkl,I}^{meas} - y_{hkl,I}^{calc}}{\sigma_{hkl,I}} \right)^2 \right] \tag{8.6}$$

Results are shown in Fig. 8.14. The residual stress model and the elastic constants C_{ij} describe the measured XRD data very well, see [45] for more details.

For this evaluation also the M'Struct software was extended and the influence of anisotropic residual stress was included for the fitting of 2θ scan (see Chapter 4 and [58]).

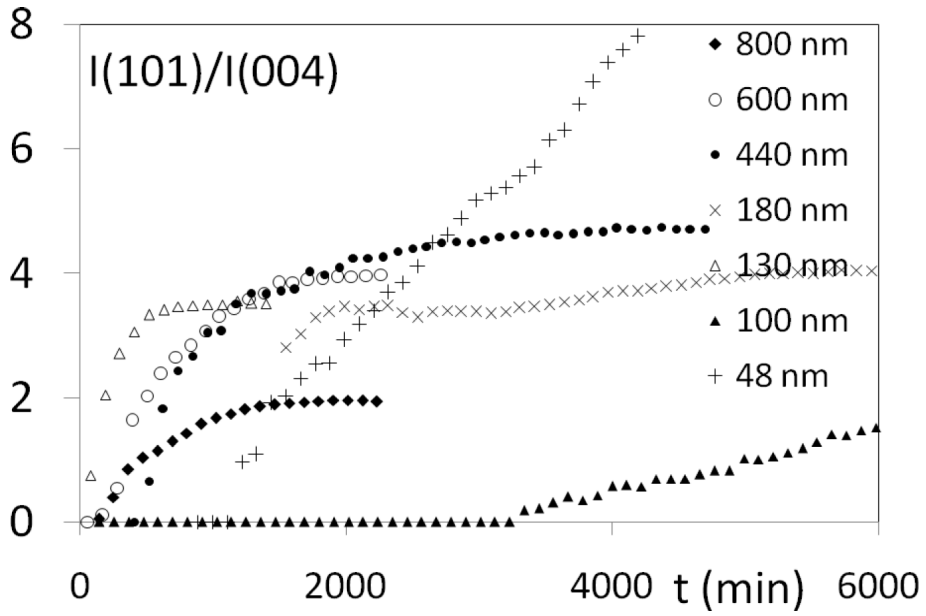

Figure 8.15: Ratios of integrated intensities of diffraction peaks 101 and 004 vs. annealing time. The annealing temperatures were 180 °C for the films with thickness 800, 600, 440, 180, 100 nm and 225 °C for films 130 and 48 nm.

The results of XRD residual stress determined by both methods are shown in dependence on sample thickness Fig. 8.14 (bottom). It can be concluded that the results of both methods agree very well and therefore both methods can be used for reliable determination of residual stresses.

8.9 Texture

XRD peak intensities were varied with the annealing time. Ratios of intensities of two diffraction peaks 101 to 004 are shown in Fig. 8.15 in dependence on annealing time for several thin films with different thickness. The dependences are not identical but a common tendency is apparent: the ratio increases up to a certain saturation value can be seen for all the films. The saturated value of the ratio is usually between 3 and 4 except for the thickest film (800 nm), where it reduces to 2, and the thinnest film (48 nm), for which it reaches much higher values. In PDF-2 (or PDF-4) ICDD database the anatase records have the following ratios of intensities: calculated for random grain distribution - 5.4 (rec. No. 89-4921, 78-2486), experimental on powder - 5.0 (21-1272). This is somewhat

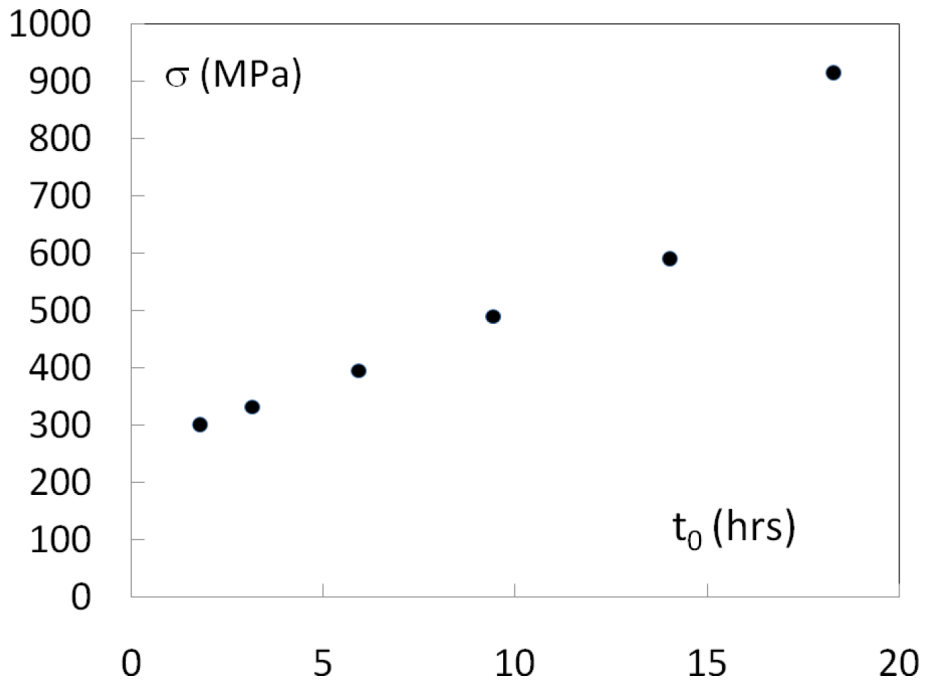

Figure 8.16: Relation between the determined tensile stress and crystallization onset.

higher than the saturated value here but it must be taken into account that in the present case the measured crystallographic planes are not parallel to the surface in the 2θ scans but inclined by small angles 13.6 and 17.9° for planes (101) and (001), respectively (peak 004). Therefore, the values of ratios reaching 4 roughly correspond to a random grain distribution.

These results mean that grains oriented with the planes (001) parallel to the surface are preferentially developed, however, with proceeding time this preferred orientation is suppressed and the grains then grow isotropically. Comparing the development of texture in Fig. 8.15 with crystallization time dependences in Fig. 8.5, we see that the stage with initial anisotropic growth is very short compared to the overall process length.

Discussion

The results obtained in this chapter lead to a question what the reason for such a large thickness dependences is in case of titanium dioxide films crystallization. One possible explanation can be related to similarity of thickness dependences of the crystallization and tensile stress. These stresses hinder the crystallization and since they are rapidly increasing

with decreasing thickness of the film, it correlates well with the behaviour of crystallization, see Fig. 8.16 where the crystallization onset is plotted against the values of tensile stress. The displayed dependence is nearly perfectly linear down to the film thickness of 100 nm. For the films thinner than about 100 nm, the determination of the residual stress is difficult and burdened with inaccuracy because of low intensities of diffraction peaks. Similar plot could be constructed for the crystallization rate k but this parameter obtained by the fitting of the Avrami equation is less reliable (because of correlation between the parameters) than the crystallization onset – that can also be determined directly.

8.10 Summary

By *in situ* high temperature XRD measurements it was confirmed that the crystallization of amorphous TiO_2 thin films depends strongly on the film thickness and it is rather slow for the films thinner than about 400 nm. Evolution of the integrated intensities of anatase diffraction peaks with annealing time follows the JMAK equation, modified by the introduction of initial time of the crystallization. This time, as well as the overall length of the transformation, increases rapidly with decreasing thickness of the film. The exponent of the JMAK equation may be interpreted as a three-dimensional growth, partially restricted in one direction. Crystallites seem to be quite large (> 100 nm) already from the beginning of crystallization. According to variation of texture at very early stages of the crystallization process the growth is preferentially along [001] direction, but then for the majority of the crystallization the growth is almost isotropic.

Apparent strain anisotropy in the films could be interpreted by using *ab initio* calculated single-crystal elastic constants. The evaluated elastic anisotropy shows that anatase [00l] direction is elastically soft axis, whereas the directions in the basal [h00] × [hk0] plane are elastically stiff. It was found that the tensile residual stresses were formed during the crystallization process and increased rapidly with reduced film thickness. Then they inhibited the crystallization which was, as already mentioned, very slow in the thinnest films.

Chapter 9

Comparison with other TiO_2 films

In order to verify the results obtained from the studies of temperature stability of the magnetron-deposited films, other sets of samples were prepared and studied [86].

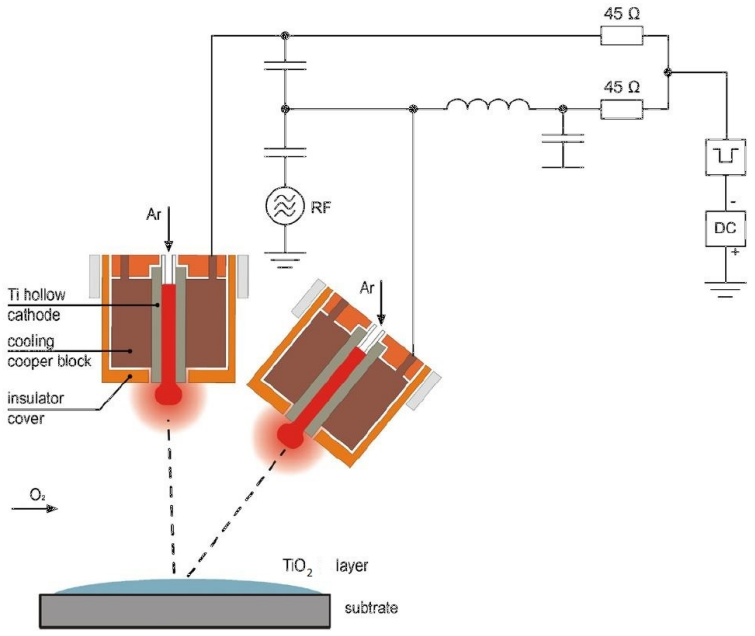

Figure 9.1: Scheme of double hollow plasma jet sputtering

The first set of films was prepared with the help of pulsed double hollow Ti cathodes plasma jet sputtering (Fig. 9.1) in the Institute of Physics, Czech Academy of Sciences, Prague. The cathodes were placed in the ultra-high vacuum chamber (106 Pa) and the operating pressure level was set at 3.5 Pa. Argon with the flow rate of 80 sccm (standard cubic centimeter per minute) was used as a carrier gas passing through both jets with the same velocity. Oxygen (80 sccm) streams were supplied to the reactor via a lateral entry. Cylindrical nozzles (hollow cathodes) were made of pure Ti (internal diameter 5 mm) and their distance from the surface was exactly 30 mm. The jets were connected to the supply of DC pulse current with frequency 2.5 kHz. Sputtered particles were blown with help of Ar out of the nozzle into the reactor and carried by the plasma jet toward the substrate. All layers were simultaneously deposited on single crystalline silicon (100). The titanium atoms reacted with oxygen only after hitting the film in this case.

The second set was prepared by a completely different method – the sol-gel method in the Institute of Inorganic Chemistry, Czech Academy of Sciences, Prague. Ti isopropoxide ($Ti(OCH(CH_3)_2)_4$, Sigma Aldrich), was used as the metal precursor. Calculated amount of $Ti(OCH(CH_3)_2)_4$ was dissolved in iso-butanol, mixed and heated for several hours. Subsequently, a suitable amount of 2,2-diethanolamine (DEA) used as a modifier was added. All reactions and handling were carried out under dry nitrogen atmosphere to prevent reaction with air humidity. Polished Si(111) was used as a substrate. Thin films were deposited by spin-coating technique (RC 8 Gyrset, KarlSuss France) and dried at 110 °C in air for 60 minutes. This deposition cycle was repeated several times until the desired thickness was obtained.

The first study was subject of the bachelor thesis by Bc. A. Kadlecová [87].

Set of seven samples with the thickness in the range of 100 – 1000 nm was studied. As in previous case, for the estimation of the temperature of "fast crystallization" the samples were subject of isochronal annealing and it was found that this temperature is between 230 and 250 °C. It was decided to perform isothermal annealing for *in situ* study at slightly higher temperatures than for magnetron-sputtered films, i.e., at 210 °C and 220 °C. More reflections of anatase were measured: 101, 004, 200 and also weak 103 and 112. The dependences could also be well described by the JMAK equation. In Fig. 9.2 the results for samples of thickness 100 and 200 nm, respectively are shown for three different reflections.

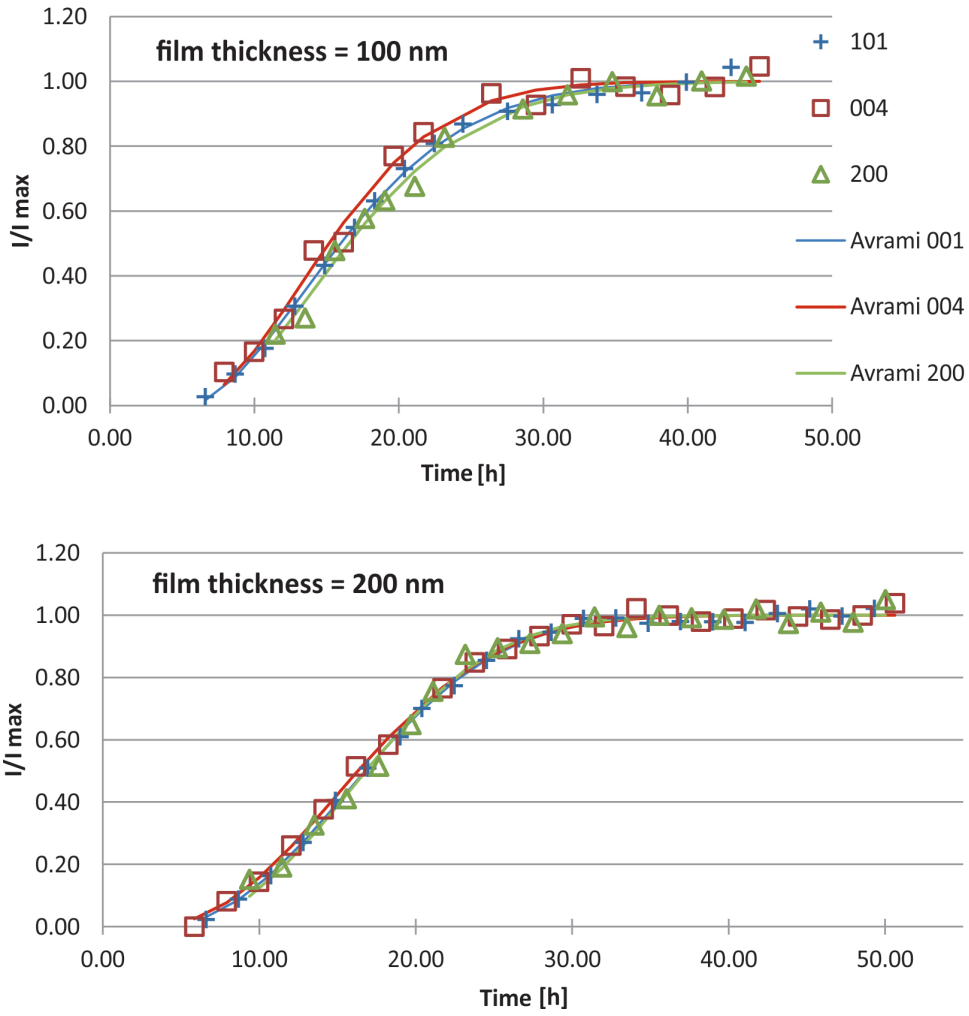

Figure 9.2: Dependences of normalized intensities of three reflections for two films with different thickness as indicated in graphs.

They give essentially the same results. Unfortunately, the dependences of crystallization rate on the film thickness was not so nicely systematic as for magnetron-deposited samples. Later measurements of the films by the surfometer and ellipsometry shown that some of them were quite inhomogeneous in thickness, which can largely influence the results.

Significant differences were found for the texture. For magnetron-sputtered films there was significant increase of ratio of intensities I_{101}/I_{004} with the annealing time, up to a certain saturated value corresponding roughly to random distribution of crystallites. Here, it was completely different and the ratio was decreasing with the time – going even further away from the random distribution (see Fig. 9.3). The preferred

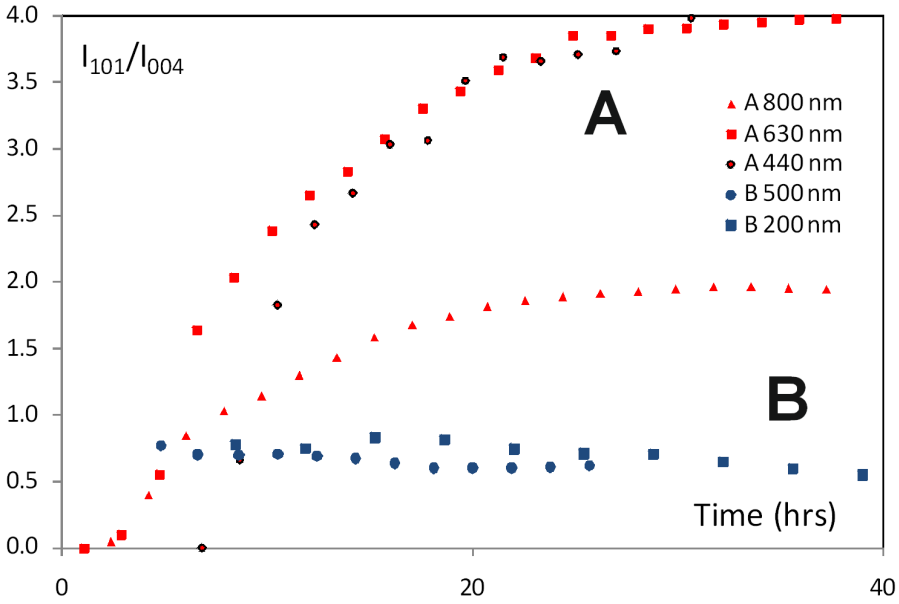

Figure 9.3: Change of the ratio of intensities I_{101}/I_{004} with annealing time for magnetron-sputtered films (set A) and for plasma jet sputtered films (set B). The results for films of different thickness as indicated in the figure are shown.

orientation was more pronounced in thicker films.

Shifts of diffraction peaks towards higher diffraction angles with annealing time until certain saturated value was reached were also observed and corresponding changes of interplanar spacings are shown in Fig. 9.4.

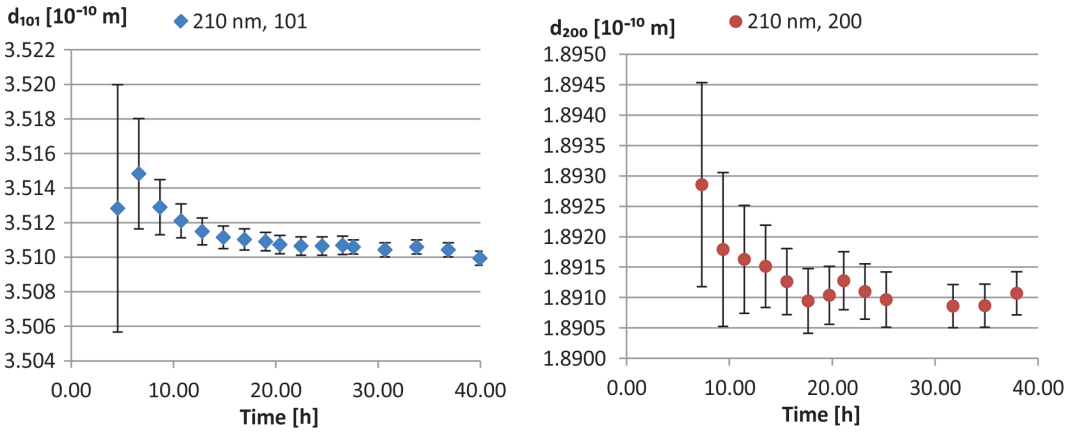

Figure 9.4: Change of interplanar spacings with annealing time for the 210 nm thick film and two diffraction maxima: 101 and 200.

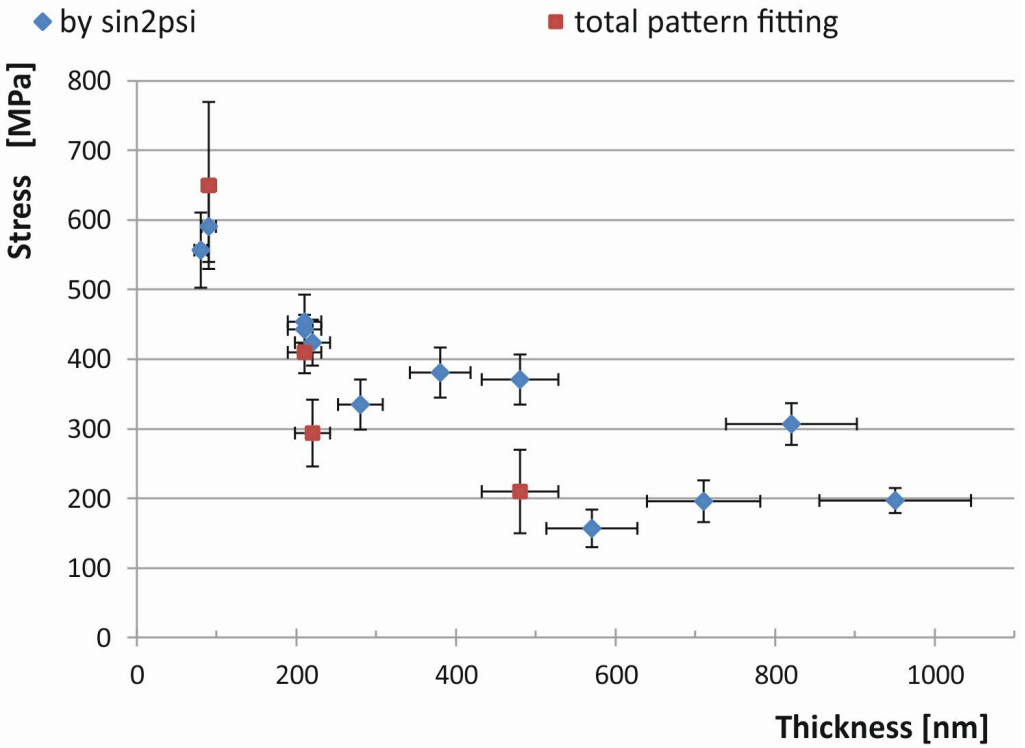

Figure 9.5: Tensile residual stress in dependence on film thickness by both $\sin^2\psi$ method and total pattern fitting as indicated in the plot.

For some samples these shifts were quite small.

This non-systematic effects can be explained by thickness inhomogeneity in the films (see above). The change of interplanar spacing could in principle be caused by more factors. For example by change of oxygen content in the films during the heating in air. However, the present tensile stresses were analyzed by careful measurements after annealing at room temperature and also by measurements of more reflections with different plane inclinations to the surface during the annealing.

As in previous case, residual stresses in the film was studied by both approaches: d vs. $\sin^2\psi$ plots for several diffraction peaks and also by the whole pattern fitting with the program M'Struct. Dependence of the stress on the film thickness, observed for the magnetron-sputtered films, was in principle confirmed and is shown in Fig. 9.5. From total pattern fitting also the values of crystallite size and microstrain were estimated to 30–100 nm and 0.2 %, respectively.

Differences between magnetron- and plasma jet-deposited films (e.g., less systematic dependences for the latter) are probably caused by thick-

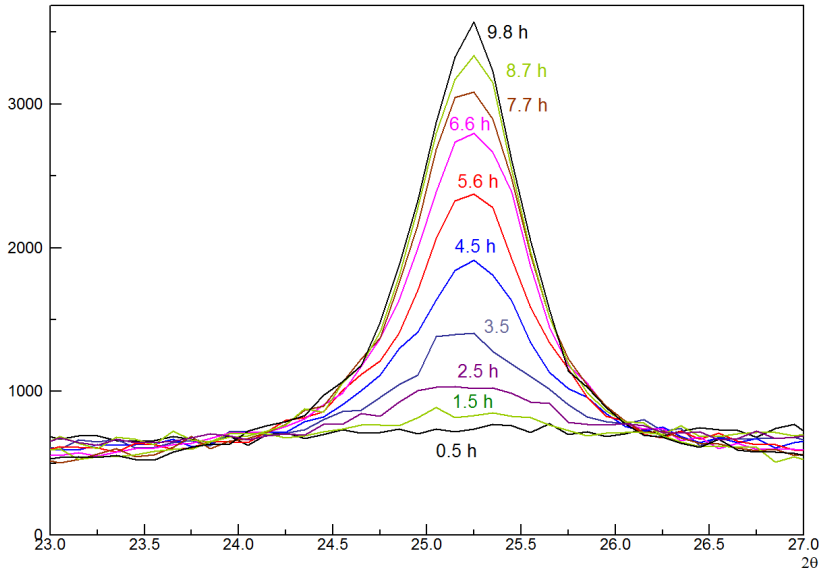

Figure 9.6: Evolution of diffraction anatase peak 101 with time (in hours) at 390 ° for sol-gel films.

ness inhomogeneity and also lower density of the latter films.

Annealing of the sol-gel films showed behavior clearly different from

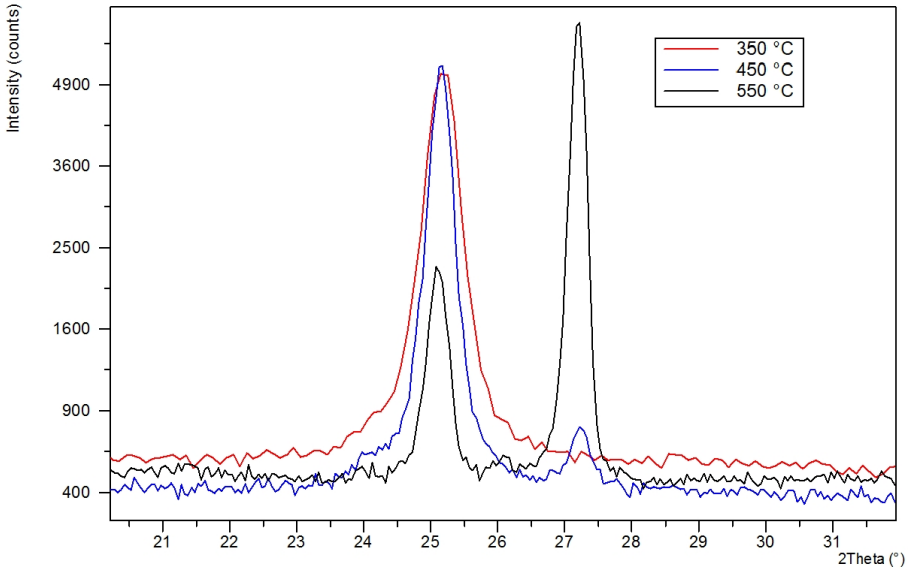

Figure 9.7: Evolution of diffraction anatase peak 101 with temperature during isochronal annealing (100 °/h) for sol-gel film. The peak on the right corresponds to rutile.

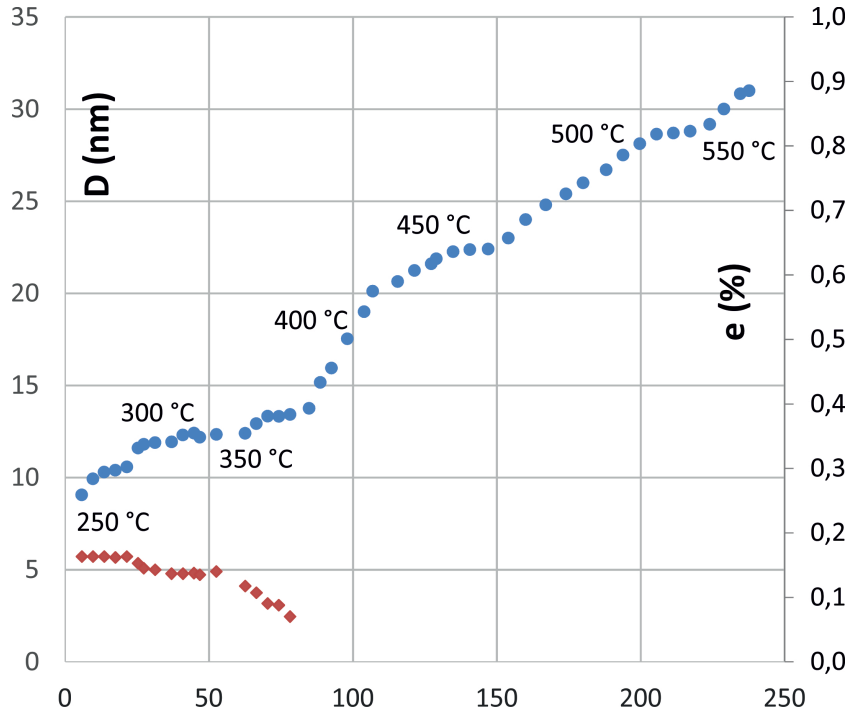

Figure 9.8: Dependence of the mean crystallite size (left axis) on the annealing time (change of temperatures indicated).

the other films. At lower annealing temperatures the diffraction peaks were very broad indicating small crystallite sizes and this broadening decreased with increasing temperature (Fig. 9.6). Phase transition into rutile appeared at about 450 °C unlike plasma-jet films where no rutile was detected below 930 °C (max. used temperature), see Fig. 9.7. During isothermal annealing the diffracted intensity varied again in agreement with the JMAK model and with $n = 1.8$. However, the peak broadening was decreasing with time. At each temperature a saturated value was reached after certain time. Then the temperature had to be increased in order to further reduce the broadening. The evaluation was performed by the M'Struct software, i.e., by the whole pattern fitting, and it was found that crystallite size effect was dominantly causing the broadening. The evolution of mean crystallite size with annealing time and also temperature can be seen in Fig. 9.8. Microstrain e is also shown there. This behavior is similar to amorphous titania powders when predetermined crystallite size can be obtained by annealing of amorphous powders for specific time at specific temperature. The procedure cannot be well used for neither magnetron-sputtered nor plasma jet sputtered films.

Chapter 10

Summary of the thesis

Structure, microstructure, phase composition and other features of TiO_2 thin films were studied mainly by X-ray diffraction and X-ray reflectivity. The results were also correlated with the measurement of hydrophilicity after irradiation with UV radiation. Many different sets of samples deposited on different substrates were studied also in dependence on deposition conditions. For the thesis, mostly the films deposited by dc-pulse reactive dual magnetron were selected. Such films are often amorphous after deposition but later nanocrystalline films could also be obtained. Presented studies were mainly focused on the influence of different film thickness on the properties, structure and thermal stability of the films.

In the first set, however, samples with the same film thickness, yet prepared with different partial oxygen pressure, were studied. Higher partial oxygen pressure resulted in well-crystallized films with dominating anatase phase and small crystallites, and displaying excellent hydrophilicity (Chapter 6).

Based on these results, samples prepared already as nanocrystalline were studied (Chapter 7). Unlike the series of samples prepared as amorphous, this set of samples had smaller crystallites of about 10 nm that start to grow at relatively high temperatures. The thinner films consisted of dominating rutile phase while the films thicker than 500 nm appeared to contain only pure anatase phase. Depth-profiling X-ray diffraction revealed that the rutile was always present only close to the substrate. Annealing above 700 °C caused reduction of the anatase phase until the anatase was completely replaced by rutile at about 1000 °C. The crystallite sizes started to grow significantly at about 500 °C from 5–7 nm to several

hundreds of nm at 1000 °C. Microstrain was decreasing at the same time. In the thinner, mixed phase films the crystallites of anatase were larger than rutile ones in the whole temperature range. This feature was found basically in all films containing both phases.

Much time was devoted to the study of crystallization of the films deposited as amorphous. *In situ* high temperature XRD measurements were performed (Chapter 8) in order to find crystallization temperature and also to investigate time development of the crystallization. It was found that the crystallization of amorphous TiO_2 thin films depends strongly on the film thickness and it is rather slow for the films thinner than about 400 nm. Evolution of the integrated intensities of anatase diffraction peaks with annealing time follows the Avrami (or JMAK) equation, modified by the introduction of initial time of the crystallization - a crystallization onset, which increases rapidly with decreasing thickness of the film. The exponent of the Avrami equation may be interpreted as a three-dimensional growth, partially restricted in one direction.

Crystallites seem to be quite large already from the very beginning of crystallization. This means that, unlike powders for magnetron-deposited films, nanocrystalline layers cannot be obtained by annealing of amorphous films for specific time at specific temperature.

From the diffraction peak shifts with proceeding crystallization it was deduced that tensile stresses were generated. They were confirmed by careful measurements at room temperature after crystallization and calculated by two different methods. Later they were also confirmed by additional *in situ* measurements. The strain anisotropy in the films was observed and interpreted using *ab initio* calculated single-crystal elastic constants, and it was found out that anatase [00l] direction is elastically soft axis, whereas the directions in the basal [h00] $\times$ [hk0] plane are elastically stiff. These tensile residual stresses increased rapidly with reducing film thickness and they can be well-correlated with the dependence of crystallization rate on the film thickness (decrease with decreasing film thickness). The tensile stresses generated during the crystallization inhibited further crystallization process. They were larger for thinner films that crystallize more slowly. This study showed that there may be a close relation between crystallization temperature and time, residual stresses and film thickness.

These basic features were confirmed also by other studies of films prepared by plasma jet sputtering. However, also some differences were found for these films such as, for example, small preferred grain orien-

tation, slightly different crystallization temperature, or different phase transitions at high temperatures. Sol-gel TiO_2 films show similar time evolution of crystallization but other features are more similar to powders, i.e., the crystallites are small at the beginning of crystallization and grow with time and temperature. This means that, as it might be expected, film properties depend to certain extent on the deposition technique.

There was one more benefit of these studies of TiO_2 thin films, which was a stimulation for extension and development of the software for powder diffraction pattern fitting M'Struct, namely the inclusion of presence of residual stresses and also texture.

Bibliography

[1] J. Šícha. *Pulsed reactive deposition of photoactive oxide films*. Ph.D thesis, Plzeň, 2008. [cited at p. 2, 41, 43, 44]

[2] R. Wang, K. Hashimoto, A. Fujishima, M. Chikuni, E. Kojima, A. Kitamura, M. Shimohigoshi, and T. Watanabe. *Nature*, 388:431–432, 1997. [cited at p. 4, 11]

[3] D. Zhang, J. A. Downing, F. J. Knorr, and J. L. McHale. *J. Phys. Chem. B*, 110:21890–21898, 2006. [cited at p. 4]

[4] R. W. Wyckoff. *Crystal Structures*. Wiley, New York, 1963. [cited at p. 6, 110]

[5] M. Horn, C. F. Schwerdtfeger, and E. P. Meagher. *Z. Kristallogr*, 136:273–281, 1972. [cited at p. 6, 110]

[6] E. P. Meagher and G. A. Lager. *Can. Mineral*, 17:77–85, 1979. [cited at p. 6, 110]

[7] X. Nie, S. Zhuo, G. Maeng, and K. Sohlberg. *Int. J. Photoenergy*, page 294042, 2009. [cited at p. 8]

[8] J. K. Burdett, T. Hughbanks, G. J. Miller, J. W. Richardson, and J. V. Smith. *J. Am. Chem. Soc*, 109:3639–3646, 1987. [cited at p. 8]

[9] S. D. Mo and W. Y. Ching. *Phys. Rev. B*, 51:13023–13032, 1995. [cited at p. 8]

[10] D. Reyes-Coronado, G. Rodríguez-Gattorno, M. E. Espinosa-Pesqueira, C. Cab, R. de Coss, and G. Oskam. *Nanotechnology*, 19:145605, 2008. [cited at p. 8]

[11] T. Luttrell, S. Halpegamage, J. Tao, A. Kramer, E. Sutter, and M. Batzill. *Sci. Rep*, 4:4043, 2014. [cited at p. 8, 9]

[12] G. S. Samsonov. *The Oxide Handbook*. IFI/Plenum Press, 1982. [cited at p. 8, 9, 105]

[13] L. S. Dubrovinsky, N. A. Dubrovinskaia, V. Swamy, J. Muscat, N. M. Harrison, R. Ahuja, B.'Holm, and B. Johansson. *Nature*, 410:653–654, 2001. [cited at p. 8]

[14] Anon. *Min. Mag*, 159:397–405, 1988. [cited at p. 8]

[15] W. A. P. J. Premaratne and N. A. Rowson. *Phys. Separ. Sci. Eng*, 12:13–22, 2003. [cited at p. 8]

[16] M. Anpo and M. Takeuchi. *J. Catal*, 216:505–516, 2003. [cited at p. 8]

[17] U. Diebold. *Surf. Sci. Rep*, 48:53–229, 2003. [cited at p. 8]

[18] A. Fujishima and X. Zhang. *C. R. Chim*, 9:750–760, 2006. [cited at p. 8, 10, 11, 105]

[19] N. Sakai, A. Fujishima, T. Watanabe, and K. Hashimoto. *J. Phys. Chem*, 105:3023–3026, 2001. [cited at p. 8]

[20] M. Ni, M. K. H. Leung, D. Y. C. Leung, and K. Sumathy. *Renew. Sust. Energ*, 11:401–425, 2007. [cited at p. 8]

[21] A. Fujishima, K. Hashimoto, and T. Watanabe. *TiO_2 Photocatalysis: Fundamentals and Applications*. BKC, 1999. [cited at p. 8, 10]

[22] A. Fujishima, K. Honda, and S. Kikuchi. *Kogyo Kagaku Zasshi*, 72:108–113, 1969. [cited at p. 8]

[23] A. Kubacka, M. Fernández-García, and G. Colón. *Chem. Rev*, 112:1555–1614, 2012. [cited at p. 9, 10]

[24] G. L. Chiarello, M. V. Dozzi, and E. Selli. *J. Energy Chem*, 26:250–258, 2017. [cited at p. 9]

[25] A. Mills and S. Hunte. *J. Photochem. Photobiol. A: Chem*, 108:1–35, 1997. [cited at p. 10]

[26] A. Fujishima, T. N. Rao, and D. A. Tryk. *J. Photochem. Photobiol. C: Photochem. Rev*, 1:1–21, 2000. [cited at p. 11]

[27] A. Mills and S. K. Lee. *J. Photochem. Photobiol. A: Chem*, 152:233–247, 2002. [cited at p. 12, 105]

[28] W. Huang, Y. Chen, C. Yang, Y. Situ, and H. Huang. *Ceram. Int*, 41:7573–7581, 2015. [cited at p. 12]

[29] B. E. Warren. *X-Ray Diffraction*. Dover Publications, 1990. [cited at p. 18]

[30] G. Lim, W. Parrish, C. Ortiz, M. Bellotto, and M. Hart. *J. Mater. Res*, 2:471–477, 1987. [cited at p. 18]

[31] R. W. James. *Solid State Phys*, 15:53–220, 1963. [cited at p. 18]

[32] J. Lhotka, R. Kužel, G. Cappuccio, and V. Valvoda. *Surf. Coating. Tech*, 148:95–100, 2001. [cited at p. 18, 19, 35, 106]

[33] H. S. Peiser, H. P. Rooksby, and A. J. C. Wilson. *X-Ray diffraction by polycrystalline materials*. Chapman & Hall, London, 1960. [cited at p. 18]

[34] P. F. Fewster. *Rep. Prog. Phys*, 59:1339–1407, 1996. [cited at p. 18]

[35] P. Colombi, P. Zanola, E. Bontempi, and L. E. Depero. *Spectrochim. Acta B Atom. Spectros*, 62:554–557, 2007. [cited at p. 19]

[36] E. J. Mittemeijer and P. Scardi, editors. *Diffraction Analysis of the Microstructure of Materials*. Springer Berlin, Heidelberg, 2004. [cited at p. 19]

[37] Th. H. de Keijser, J. I. Langford, E. J. Mittemeijer, and A. B. P. Vogels. *J. Appl. Cryst*, 15:308–313, 1982. [cited at p. 21]

[38] H. P. Klug and L. E. Alexander. *X-ray Diffraction Procedures*. John Wiley & Sons, New York, 1974. [cited at p. 23, 25]

[39] J. I. Langford and A. J. C. Wilson. *J. Appl. Cryst*, 11:102–113, 1978. [cited at p. 23]

[40] B. E. Warren. *X-Ray Diffraction*. Addison-Wesley, 1969. [cited at p. 25]

[41] A. March. *Z. Kristallogr*, 81:285–297, 1932. [cited at p. 27]

[42] W. A. Dollase. *J. Appl. Cryst*, 19:267–272, 1986. [cited at p. 27]

[43] I. Kraus and V. V. Trofimov. *Rentgenová tenzometrie*. Academia, Praha, 1988. [cited at p. 29]

[44] I. C. Noyan and J. B. Cohen. *Residual Stress. Measurement by Diffraction and Interpretation*. Springer, New York, 1987. [cited at p. 29, 78]

[45] Z. Matěj, R. Kužel, and L. Nichtová. *Metall. Mater. Trans. A*, 42:3323, 2011. [cited at p. 31, 78, 83]

[46] R. A. Winholtz and J. B. Cohen. *Aust. J. Phys*, 41:189–199, 1988. [cited at p. 31]

[47] V. M. Hauk. *Adv. X-Ray Anal*, 27:101–120, 1984. [cited at p. 31]

[48] H. Dolle. *J. Appl. Cryst*, 12:489–501, 1979. [cited at p. 31]

[49] M. Barral, J. L. Lebrun, J. M. Sprauel, and G. Maeder. *Metall. Trans. A*, 18:1229–1238, 1987. [cited at p. 31]

[50] P. Penning and C. M. Brakman. *Acta Cryst. A*, 44:157–167, 1988. [cited at p. 31]

[51] A. Erko, M. Idir, T. Krist, and G. Michette. *Modern Developments in X-Ray and Neutron Optics*. Springer, 2008. [cited at p. 32]

[52] J. Als-Nielsen and D. McMorrow. *Elements of Modern X-ray Physics*. Wiley, 2011. ISBN-10: 0470973943. [cited at p. 33]

[53] J. Rodriguez-Carvajal. Fullprof program. *Physica B*, 192:55–69, 1993. [cited at p. 34]

[54] A. C. Larson and R. B. Von Dreele. General structure analysis system (gsas). Los Alamos National Laboratory Report LAUR 86-748, 2004. [cited at p. 34]

[55] P. Scardi and M. Leoni. Whole powder pattern modelling. *Acta Cryst A*, 58:190–200, 2002. [cited at p. 34, 35]

[56] G. Ribárik, T. Ungár, and J. Gubicza. Mwp-fit: a program for multiple whole-profile fitting of diffraction peak profiles by ab initio theoretical functions. *J. Appl. Cryst*, 34:669–676, 2001. [cited at p. 34, 35]

[57] L. Lutterotti. Total pattern fitting for the combined size-strain and stress-texture determination in thin film diffraction. *Nucl. Instrum. Methods Phys. Res. B*, 268:334–340, 2010. [cited at p. 35]

[58] Z. Matěj and R. Kužel. Mstruct - program library for microstructure analysis by powder diffraction. http://xray.cz/mstruct/, 2011. [cited at p. 35, 45, 52, 83]

[59] Y. Suda, H. Kawasaki, T. Ueda, and T. Ohshima. *Thin Solid Films*, 453–454:162–166, 2004. [cited at p. 41]

[60] K. R. Patil, S. D. Sathaye, Y. B. Khollam, N. R. Pawaskar, and A. B. Mandale. *Mater. Lett*, 57:1775–1780, 2003. [cited at p. 41]

[61] L. C. Klein. *Sol-Gel Optics: Processing and Applications*. Springer, 1994. [cited at p. 41]

[62] X. Zhang, K. Cooke, P. Carmichael, and I. P. Parkin. *Surf. Coating. Tech*, 236:290–295, 2013. [cited at p. 41]

[63] J. Musil, P. Baroch, J. Vlček, K. H. Nam, and J. G. Han. *Thin Solid Films*, 475:208–218, 2005. [cited at p. 41]

[64] P. Navinsek, P. Panjan, and I. Milosev. *Surf. Coat. Technol*, 116–119:476–487, 1999. [cited at p. 41]

[65] T. P. Chou and G. Cao. *J. Sol-gel Sci. Technol*, 27:31–41, 2003. [cited at p. 41]

[66] K. E. Cooke, J. Hampshire, W. Southall, and D. G. Teer. *Surf. Coat. Technol*, 177–178:789–794, 2004. [cited at p. 41]

[67] N. Farahani, P. J. Kelly, G. West, M. Ratova, C. Hill, and V. Vishnyakov. *Thin Solid Films*, 520:1464–1469, 2001. [cited at p. 42]

[68] K. L. Choy. *Prog. Mater. Sci*, 48:157–170, 2003. [cited at p. 42]

[69] R. I. Bickley, T. Gonzalez-Carreno, J. S. Lees, L. Palmisano, and R. J. D. Tilley. *J. Solid State Chem*, 92:178–190, 1991. [cited at p. 44]

[70] H. Harada and T. Ueda. *Chem. Phys. Lett*, 106:229–231, 1984. [cited at p. 44]

[71] L. Nichtová. *RTG strukturní studium nanokrystalických tenkých vrstev*. Master thesis, Prague, 2005. [cited at p. 44, 45, 64]

[72] H. Kiessig. *Ann. Phys*, 402:715–768, 1931. [cited at p. 60]

[73] J. Musil, D. Heřman, and J. Šícha. *J. Vac. Sci. Technol. A*, 24:521, 2006. [cited at p. 65]

[74] Z. Matěj, R. Kužel, and L. Nichtová. *Powder Diffr*, 25:125–131, 2010. [cited at p. 69, 78]

[75] M. J. Avrami. *J. Chem. Phys*, 7:1103, 1939. [cited at p. 69]

[76] M. J. Avrami. *J. Chem. Phys*, 8:212, 1941. [cited at p. 69]

[77] A. N. Kolmogorov. *Izv. Akad. Nauk SSSR Ser. Mat*, 3:355, 1937. [cited at p. 69]

[78] W. A. Johnson and R. Mehl. *Trans. AIME*, 185:416, 1939. [cited at p. 69]

[79] R. Kužel, L. Nichtová, Z. Matěj, J. Šícha, and J. Musil. *Z. Kristallogr*, 27:287–294, 2008. [cited at p. 74]

[80] T. Shibata, H. Irie, and K. Hashimoto. *J. Phys. Chem. B*, 107:10696–10698, 2003. [cited at p. 78]

[81] T. Shibata, H. Irie, D. A. Tryk, and K. Hashimoto. *J. Phys. Chem. C*, 113:12811–12817, 2009. [cited at p. 78]

[82] U. Welzel, J. Ligot, P. Lamparter, A. C. Vermeulen, and E. J. Mittemeijer. *J. Appl. Crystallogr*, 38:1–29, 2005. [cited at p. 78]

[83] M. Iuga, G. Steinle-Neumann, and J. Meinhardt. *Eur. Phys. J. B*, 58:127–133, 2007. [cited at p. 79]

[84] H. Yao, L. Ouyang, and W. Y. Ching. *J. Am. Ceram. Soc*, 90:3194–3204, 2007. [cited at p. 79]

[85] E. Shojaee and M. R. Mohammadizadeh. *J. Phys. Chem. B*, 107:10696–10698, 2010. [cited at p. 79]

[86] R. Kužel, L. Nichtová, Z. Matěj, Z. Hubička, and J. Buršík. *Mater. Res. Soc. Symp. P*, 1352:57–62, 2012. [cited at p. 87]

[87] A. Kadlecová. *Rtg difrakční studium teplotní stability tenkých vrstev a prášků TiO_2*. Bachelor thesis, Prague, 2013. [cited at p. 88]

Articles related to the topic of the thesis:

1. R. Kužel, L. Nichtová, Z. Matěj, D. Heřman, J. Šícha, and J. Musil, Study of Crystallization of Magnetron Sputtered TiO_2 Thin Films by X-ray Scattering, *Z. Kristallogr.* 26 (2007) 247–252

2. R. Kužel, L. Nichtová, D. Heřman, J. Šícha, and J. Musil, Growth of Magnetron Sputtered TiO_2 Thin Films Studied by X-ray Scattering, *Z. Kristallogr.* 26 (2007) 241–246

3. R. Kužel, L. Nichtová, Z. Matěj, J. Šícha, and J. Musil, Magnetron Deposited TiO_2 Thin Films - Crystallization and Temperature Dependence of Microstructure and Phase Composition, *Z. Kristallogr.* 27 (2008) 287–294

4. L. Nichtová, R. Kužel, Z. Matěj, J. Šícha, and J. Musil, Time and Thickness Dependence of Crystallization of Amorphous Magnetron Deposited TiO_2 Thin Films, *Z. Kristallogr.* 30 (2009), 235–240

5. Z. Matěj, R. Kužel, and L. Nichtová, Microstructural Characterization of Nanocrystalline Powders and Thin Films by X-ray Powder Diffraction, Nanocon 2010, conference proceedings (2009) 53–60

6. Z. Matěj, L. Nichtová, and R. Kužel, Coplanar Grazing Exit X-ray Diffraction on Thin Polycrystalline Films, *Z. Kristallogr.* 30 (2009) 157–162

7. R. Kužel, L. Nichtová, Z. Matěj, and T. Brunatová, Temperature Evolution of Microstructure of TiO_2 thin films and powders studied by X-ray diffraction, Nanocon 2010, 2nd international conference, (2010) 346–351

8. Z. Matěj, R. Kužel, and L. Nichtová, XRD total pattern fitting applied to study of microstructure of TiO_2 films, *Powder Diffr.* 25 (2010) 125–131

9. R. Kužel, L. Nichtová, Z. Matěj, and J. Musil, In-situ X-ray Diffraction Studies of Time and Thickness Dependence of Crystallization of Amorphous TiO_2 Thin Films and Stress Evolution, *Thin Solid Films* 519 (2010) 1649–1654

10. Z. Matěj, R. Kužel, and L. Nichtová, X-Ray Diffraction Analysis of Residual Stress in Thin Polycrystalline Anatase Films and Elastic Anisotropy of Anatase, *Metall. Mater. Trans. A* 42 (2011) 3323–3332

11. R. Kužel, L. Nichtová, Z. Matěj, Z. Hubička, J. Buršík, *Materials Research Society Symposium Proceedings*, 1352 (2012) 57–62.

Article unrelated to the topic of the thesis:

12. M. Drabik, A. Choukourov, A. Artemenko, O. Polonskyi, O. Kylian, J. Kousal, L. Nichtová, V. Cimrova, D. Slavinska, and H. Biederman, Structure and Composition of Titanium Nanocluster Films Prepared by a Gas Aggregation Cluster Source, *J. Phys. Chem. C* 115 (2011) 20937–20944

List of Figures

2.1 Rutile (top) and anatase (bottom) diffraction patterns. 5
2.2 Rutile, anatase and brookite crystal structures, the red dots represent oxygen atoms and the green ones represent titanium atoms 6
2.3 Views on anatase (left) and rutile (right) structures along *a*, *b* and *c* axis as obtained by the program Diamond (Crystal Impact software). 7
2.4 Phase diagram of Ti-O system taken from Samsonov [12]. The region Ti_2O_3-TiO_2 contains Ti_2O_3, Ti_3O_5, seven descrete phases of the homologous series Ti_nO_{2n-1} (Magneli phases) and TiO_2. 9
2.5 Schematic diagram of an electrochemical photocell [18]. (1) n-type TiO_2 electrode; (2) platinum back counter electrode; (3) ionically conducting separator; (4) gas buret; (5) load resistance and (6) voltmeter 10
2.6 The principle of the photocatalytic processes and the formation of the highly reactive radicals on the surface of the TiO_2 particle [18] 11
2.7 Schematic illustration of the major processes associated with the photoinduced superhydrophilic property of titania. UV excitation of the semiconductor creates electron-hole pairs. The holes can oxidixe bridging O^{2-} species on the surface into oxygen, thereby creating vacancies. The photogenerated electrons can reduce the Ti^{4+} atoms to Ti^{3+}. Dissociative adsorption of water onto the irradiated surface hydroxylates it and renders it considerably more hydrophilic. The process is reversed in the dark as the oxygen oxidizes the Ti^{3+} species present and the reduced oxygen fills the bridging oxygen vacancies [27]. . 12

3.1 Bragg-Brentano conventional powder diffraction geometry - information from the grains oriented with the corresponding planes parallel to the surface 14
3.2 Bragg-Brentano conventional powder diffraction geometry. . . 15
3.3 Scheme of the parallel beam geometry. 16
3.4 Panalytical X'Pert MRD diffractometer in parallel beam geometry. 17
3.5 Definition of angles α, β and θ, [32]. 19
3.6 Illustration of the coordinate systems associated with the specimen and laboratory. 29
3.7 Reflectivity curve of 54 nm titanium dioxide thin film, before annealing (black curve) and after annealing at 350°*C* and 450°*C*. The small oscillations are so-called Kiessig fringes. 32

4.1 An example of comparison of measured and calculated diffraction patterns (a). The (b) panel displays details of the selected parts of the (a) plot in case the residual stress in the film is included (solid line) and in case no residual stress is assumed and only unit-cell parameters are refined (dashed dark line). Difference plots for these two cases in the (b) plot is shown in (c) panel. 40

5.1 The scheme of the deposition chamber in the dual magnetron system. 42

6.1 The diffraction patterns of 1000 nm thin films, prepared with low (top panel), medium (middle) and high (bottom) partial oxygen pressure. Each sample was measured as prepared and after annealing at 400 °C (thicker curve). 46
6.2 The reflectivity curves for 1000 nm thin samples, prepared with different partial oxygen pressure. 47
6.3 The change of reflectivity curves with annealing for samples prepared with low (top panel) and high (bottom panel) partial oxygen pressure. 48
6.4 The reflectivity curves for samples prepared with low (top left panel as prepared, top right panel annealed), medium (middle left panel as prepared) and high partial oxygen pressure (bottom panels). Blue curve is the measured data, red curve is the fit. 49

7.1 Fit of the diffraction pattern for 2000 nm thin film, as prepared (top and the inset detail) and after annealing at 800 °C (bottom). The incidence angle was 0.5 degrees. 53
7.2 The diffraction pattern for as-prepared 100 nm (top) and 220 nm thin film (bottom). The incidence angle was 0.5 degrees. In both films broad rutile peaks are dominating, for 220 nm an indication of narrower anatase peaks can be noticed. 54
7.3 The diffraction pattern for as-prepared 515 nm (top), 935 nm (middle) and 2000 nm thin film (bottom). The incidence angle was 1.5 degrees. In all the anatase peaks are dominating, in case of 2000 nm there nearly no indication of rutile. 55
7.4 Evolution of phase composition of thin film (220 nm) with annealing (top panel). While the as prepared sample is a mixture of rutile and anatase, at highest annealing temperatures the sample almost entirely transforms to rutile. In the bottom panel analogous dependence is displayed for thick (2000 nm) sample, where anatase phase transforms to rutile at higher annealing temperatures. 56
7.5 Dependence of crystallite size D (left) and microstrain e (right) on annealing temperature; for anatase – 2000 nm thick film (◆), 935 nm (○), 220 nm (×) and rutile 220 nm (▲). 57
7.6 Depth profile of the sample 935 nm on silicon substrate. The first peak belongs to anatase (101) reflection, the second one is rutile (110). 58
7.7 The reflectivity curves and their fits for all measured titanium dioxide thin films. Blue curve represents the measured data and red curve is the fit. 59
7.8 Dependence of spacing d on $\sin^2\psi$ for reflection 200 of 2000 nm sample on glass. 61
7.9 Dependence of $\frac{d_{hkl}-d_0}{d_0}$ on $\sin^2\psi$ for different reflections of two samples. 61
7.10 Measured and simulated pole figures of (101) and (202) diffractions for the 200 nm film 62
7.11 Water contact angle measurement of 2000 nm, 515 nm and 220 nm thin film (from top to bottom). 63

8.1 MRI diffractometer with high temperature chamber. 66
8.2 XRD line profiles of 101 anatase peak for film with thickness 800 nm (top) and 180 nm (bottom) for different temperatures. 68

8.3 Integrated intensities of anatase diffraction peak 101 normalized to the value reached after crystallization are displayed in dependence on annealing time for films with several different thickness. The experimental data were fitted by Avrami equations. 70
8.4 Dependence of the integrated intensities of anatase diffraction peak 101 normalized to the value reached after crystallization on annealing time for the thinnest film (48 nm). The symbols represent experimental values, the line is fitted Avrami equation. 71
8.5 Full set of dependences of the integrated intensities of anatase diffraction peak 101 calculated from the fitted Avrami equations on the annealing time. Solid lines and dashed line (short lines, for 630 nm) correspond to the films annealed at 180 °C, dashed lines correspond to the films anealed at 220 °C. 72
8.6 Dependence of crystallization onset t_0 (●) and exponent of the Avrami equation n (■) on the film thickness. Filled symbols correspond to the film annealed at 180 °C and open symbols to the films annealed at 220 °C. 72
8.7 Measured integral breadth of 101 anatase peak (in reciprocal space units, 1/d) vs. annealing time for different film thicknesses. The level of instrumental broadening in the parallel beam geometry was at about 0.0027 10^{-10} m. 73
8.8 The reflectivity curves (blue) with corresponding fits (red) for the samples with thickness 300 nm (top) and 130 nm (bottom), annealed at 200 °C. 75
8.9 Dependence of the surface roughness on the film thickness. . . 76
8.10 Changes of lattice spacing d of anatase lattice plane (101) with annealing time in dependence on film thickness. Annealing temperatures were 180 °C for films with thickness 800, 600, 440, and 180 nm and 225 °C for 130 and 48 nm. 77
8.11 Dependence of tensile stress determined by the $sin^2\psi$ method on the film thickness. 78
8.12 Two diffraction profiles (diffracted intensity vs. 2 theta), 105 and 211, are shown for different diffracting plane inclinations ψ with respect to the film surface ($\psi = 0°$ – thick line, $\psi = 40°$ – crosses, $\psi = 56°$ – dots, and $\psi = 65°$ – thin dashed line). Relative peak shifts for $\psi = 65°$ were $-0.116°$ and $-0.071°$ for 105 and 211 reflections, respectively. 79

8.13 Top left panel: strain measured on the (200) plane for thin TiO_2 films with different thicknesses. Top right: strain measured for the 440 nm TiO_2 film on different lattice planes. Bottom left: strain anisotropy, K_{hkl}, ratio of d_{hkl} vs. $\sin^2\psi$ slope to the d_{hkl} vs. $\sin^2\psi$ intercept plotted for different lattice planes and the films with different thicknesses. Bottom right: the slopes K_{hkl} for 440 nm sample and different *hkl* reflections vs. projection of the [*hkl*] diffraction vector direction onto the reciprocal space [001] direction. 80
8.14 Slopes K_{hkl} for 440 nm sample and various *hkl* reflections (top). Dependence of the XRD residual stress on the film thickness (bottom). Values obtained from direct XRD stress measurements (×) are compared with values obtained from the whole pattern fitting (●). 82
8.15 Ratios of integrated intensities of diffraction peaks 101 and 004 vs. annealing time. The annealing temperatures were 180 °C for the films with thickness 800, 600, 440, 180, 100 nm and 225 °C for films 130 and 48 nm. 84
8.16 Relation between the determined tensile stress and crystallization onset. 85

9.1 Scheme of double hollow plasma jet sputtering 87
9.2 Dependences of normalized intensities of three reflections for two films with different thickness as indicated in graphs. . . . 89
9.3 Change of the ratio of intensities I_{101}/I_{004} with annealing time for magnetron-sputtered films (set A) and for plasma jet sputtered films (set B). The results for films of different thickness as indicated in the figure are shown. 90
9.4 Change of interplanar spacings with annealing time for the 210 nm thick film and two diffraction maxima: 101 and 200. . 90
9.5 Tensile residual stress in dependence on film thickness by both $\sin^2\psi$ method and total pattern fitting as indicated in the plot. 91
9.6 Evolution of diffraction anatase peak 101 with time (in hours) at 390 ° for sol-gel films. 92
9.7 Evolution of diffraction anatase peak 101 with temperature during isochronal annealing (100 °/h) for sol-gel film. The peak on the right corresponds to rutile. 92
9.8 Dependence of the mean crystallite size (left axis) on the annealing time (change of temperatures indicated). 93

List of Tables

2.1 Spacegroups and lattice parameters of anatase, rutile and brookite. Data taken from Ref. [4, 5, 6]. 6

3.1 Constants in the modified Williamson-Hall plot. 25

7.1 The values of the electron density and roughness evaluated from fitting of X-ray reflectivity. The displayed uncertainties are rough estimates based on the final populations. 58

8.1 The values of the density, film thickness (only for the thinnest films) and roughness evaluated from fitting. The displayed uncertainties are rough estimates based on the final populations. 74

8.2 Evaluated XRD residual stresses. T is the film thickness, σ is the residual stress, w is the weight of the Voigt model, and a and c are the lattice parameters. 83

List of Abbreviations

C	Cauchy
C2	quadratic Cauchy
CVD	chemical vapour decomposition
DM	dual magnetron
FT	Fourier transform
FWHM	full width at half maximum
G	Gauss
HT	high-temperature
ICCD	The International Centre for Diffraction Data
JMAK	Johnson-Mehl-Avrami-Kolmogorov
NIST	National Institute of Standards
ODF	orientation distribution function
PDF	powder diffraction file
UV	ultra-violet
XRD	X-ray diffraction
XRR	X-ray reflectivity